2-9(mix)

NTS-88.25

NASA CR-121009

EVALUATION OF CIRCUMFERENTIAL AIRFLOW UNIFORMITY ENTERING COMBUSTORS FROM COMPRESSORS

VOLUME I - DISCUSSION OF DATA AND RESULTS

November 1972

by J. H. Shadowen and W. J. Egan, Jr.

PRATT & WHITNEY AIRCRAFT
FLORIDA RESEARCH AND DEVELOPMENT CENTER

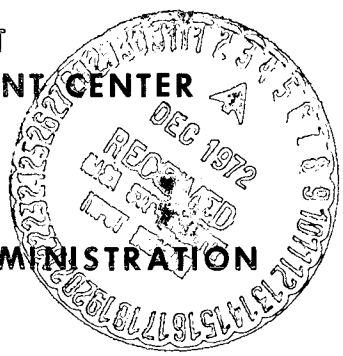

Prepared For

NATIONAL AERONAUTICS AND SPACE ADMINISTRATION

NASA Lewis Research Center
Contract NAS3-15693

31

1. Report No.	2. Government Accession No.	3. Recipient's Catalog No.
NASA CR-121009		

4. Title and Subtitle	5. Report Date
EVALUATION OF CIRCUMFERENTIAL AIRFLOW UNIFORMITY ENTERING COMBUSTORS FROM COMPRESSORS, VOLUME I - DISCUSSION OF DATA AND RESULTS	November 1972
	6. Performing Organization Code
7. Author(s)	8. Performing Organization Report No.
J. H. Shadowen and W. J. Egan, Jr.	PWA FR-5183
	10. Work Unit No.
9. Performing Organization Name and Address	11. Contract or Grant No.
Pratt & Whitney Aircraft Division of United Aircraft Corporation Florida Research and Development Center West Palm Beach, Florida 33402	NAS3-15693
	13. Type of Report and Period Covered
12. Sponsoring Agency Name and Address	Contractor Report
National Aeronautics and Space Administration Washington, D. C. 20546	14. Sponsoring Agency Code

15. Supplementary Notes

Project Manager, Everett E. Bailey, Fluid Systems Components Division, NASA Lewis Research Center, Cleveland, Ohio 44135

16. Abstract

A study of the compressor discharge airflow uniformity of two compressors from advanced engines, the J58 and F100/F401, was made. Compressor discharge pressures and temperatures at up to 33 circumferential rake locations allowed the airflow distribution to be ascertained and computer plotted. Several flight conditions and compressor variables, i.e., inlet distortion, modified seals, etc., were analyzed. An unexpectedly high nonuniform airflow was found for both compressors. Circumferential airflow deviation differences of up to 52% from maximum to minimum were found for the J58, and up to 40% for the F100/F401. The effects of aerodynamic and thermal distortion were found to be additive. The data were analyzed for influence of exit guide vane wakes and found free of any effect. Data system errors were small in relation to the measured pressure and temperature variations.

17. Key Words (Suggested by Author(s))		18. Distribution Statement
Compressor	Temperature Pattern	Unclassified - unlimited
Combustor	Pressure Pattern	
Diffuser		
Airflow Uniformity		
Airflow Deviation		

19. Security Classif. (of this report)	20. Security Classif. (of this page)	21. No. of Pages	22. Price*
Unclassified	Unclassified	122	$3.00

* For sale by the National Technical Information Service, Springfield, Virginia 22151

CONTENTS

ILLUSTRATIONS

ILLUSTRATIONS (Continued)

ILLUSTRATIONS (Continued)

ILLUSTRATIONS (Continued)

ILLUSTRATIONS (Continued)

TABLES

SUMMARY

A study of the airflow uniformity leaving compressors and entering combustors was made using compressors from two advanced engines, the J58 and the F100/F401. Compressor discharge total pressures, total temperatures, and static pressures were obtained from rig tests at up to 33 circumferential rake locations allowing the calculation of local airflow ratio and circumferential airflow deviation. The data analyzed encompassed test conditions of sea level takeoff, cruise, and combat, and compressor variables such as aerodynamic and thermal distortion, modified shrouds and seals, and indexed stators. The results are presented as computer-generated plots.

For all cases analyzed, the J58 compressor showed highly nonuniform airflow leaving the compressor. Local airflow values ranged from 52% above to 88% below average. In the circumferential direction airflow values ranged from 20% above to 32% below average. At least four areas of high airflow on the midspan are noticeable in each case. The data were analyzed for influence of exit guide vane (EGV) wakes and found free of any effect.

The F100/F401 high compressor showed more uniform airflow than did the J58 compressor but it still has local airflow values ranging from 35% above to 52% below average. In the circumferential direction, airflow values ranged from 20% above to 21% below average. The areas of high airflow are concentrated on the compressor hub. Again the data were analyzed for influence of exit guide vane (EGV) wakes and found free of any effect. The effects of aerodynamic and thermal distortion were found to be additive.

The information presented shows that an unexpected compressor discharge airflow nonuniformity problem exists in state-of-the-art compressors. Methods of distributing the airflow more evenly both in the compressor and in the diffuser-combustor system should be investigated.

INTRODUCTION

One of the significant problems in the development of turbojet combustion systems has been that of obtaining the uniform turbine inlet temperature patterns necessary for long turbine life. During engine development programs it has often been observed that large-scale circumferential turbine inlet temperature variations are insensitive to changes in combustor geometry, giving rise to the theory that these circumferential temperature nonuniformities are caused by compressor discharge airflow nonuniformities. Compressor discharge instrumentation for past engine development programs, as contrasted with research requirements, has been inadequate to prove or disprove the presence of nonuniform airflow. Airflow has therefore usually been assumed to be uniform because of the apparent mechanical uniformity of the compressor.

The objective of this program was to determine if, and to what extent, airflow nonuniformities are present in the discharge of advanced turbine engine compressors. For this purpose, compressors from two engines were chosen for investigation: the J58 and the F100/F401. The J58 is a high-altitude supersonic cruise, turbojet engine, whereas the F100/F401 is an advanced turbofan engine for the F-15/F-14B air superiority fighter aircraft.

Data from several J58 compressor rig tests with extensive instrumentation were available. For the F100/F401 high compressor, the necessary compressor discharge instrumentation was designed and fabricated under this program, and data were gathered during the normal course of compressor rig testing. Data from both compressors were analyzed under this program and the results are presented herein. Test variables included sea level takeoff (SLTO), cruise and combat operating conditions, indexing of stators, modifications to seals and shrouds, and inlet total pressure and temperature distortion. The inlet total pressure and temperature distortions will hereafter be termed aerodynamic and thermal distortion, respectively.

The data were obtained from up to 33 total pressure rakes and up to 12 total temperature rakes installed in the compressor discharge. Each rake had five or seven heads spaced across the annulus. Static pressures in the same plane at up to ten locations on each wall were also obtained.

This report discusses the acquisition, analysis technique, and results of the data obtained from the J58 compressor rig and the F100/F401 high compressor rig. It presents the results in nondimensionalized plot form for ease of comparison between test conditions and variables.

A companion report, NASA CR-121010 "Evaluation of Circumferential Airflow Uniformity Entering Combustors From Compressors, Volume II - Data Supplement" (Reference 1), contains the input data for each test case in both tabulated and computer-plotted form. It is designed for the use of those desirous of implementing the results of this report, or in further exploration of the subject of compressor discharge uniformity.

SCOPE OF INVESTIGATION

To investigate the possibility of nonuniform airflow leaving the compressor and entering the diffuser-combustor system of advanced turbine engines, two compressors were chosen for evaluation. The J58 turbojet is a large, supersonic cruise engine. The compressor has nine stages, a compressor pressure ratio of 8.75:1, and is shown schematically in figure 1. The other compressor chosen was the F100/F401 high compressor. This engine is an advanced turbofan and is currently in the development stage. It will power the F-15/F-14B air superiority fighter series. The high compressor of this engine has ten stages, a compressor pressure ratio of 8:1, and is shown schematically in figure 2.

These compressors were analyzed for several variables at sea level takeoff (SLTO), cruise, and combat conditions. The variables included aerodynamic and/or thermal distortion, indexing of stators, and modified seals and shrouds. Not all conditions and variables were studied for both compressors, however. The data were obtained from seven builds of two J58 compressor rigs and two builds of an F100/F401 high compressor rig. Run conditions for each compressor are given in table I, which shows the wide variation for the 31 test points considered in this study.

The data obtained for these test points included total pressures and temperatures and static pressures at the compressor discharge plane. These data allowed the radial and circumferential total pressure and temperature and the

circumferential static pressure distributions to be obtained. From these profiles, the average circumferential airflow deviation and the local airflow deviation were found for each test point. Inlet distortion patterns were obtained from total pressure and total temperature rakes installed in the compressor inlet.

DESCRIPTION OF RIGS AND INSTRUMENTATION

J58 Compressor Rig and Instrumentation

The J58 compressor is used in a high altitude, high flight Mach number engine that is considered state-of-the-art in turbojet engines. This compressor is a single-spool, variable inlet guide vane, fixed stator design with an interstage bleed and has a design pressure ratio of 8.75:1. The compressor is shown schematically in figure 1 along with a table describing each stage.

The data used in this program to determine the J58 compressor discharge airflow uniformity were all generated in the course of the engine development program and were made available to this program. During compressor development, two compressor rigs were instrumented at the compressor discharge plane with up to 33 seven-point radial total pressure rakes, up to 8 static pressure taps on the diffuser annulus outer wall, and up to 11 total temperature probes with one or two half-shielded temperature elements. Typical instrumentation is shown in figure 3. A schematic view of the circumferential locations of the instrumentation is shown in figure 4, while the axial location is shown in figure 1. For one build, 206, the one- and two-point total temperature elements were replaced with five-point radial temperature rakes and eight additional static pressures were installed on the diffuser annulus ID. This configuration is shown schematically in figure 5. The different builds used various combinations of static pressures, total pressures, and total temperatures. Table II describes the various combinations of instrumentation used.

The compressor rig was tested in the Florida Research and Development Center C-3 altitude test facility. This facility has an atmospheric intake upstream of a flow-controlling butterfly valve. The air is fed to a cylindrical plenum approximately 6.096 m (20 ft) dia x 6.096 m (20 ft) long. Flow straightening in the plenum entrance is accomplished by a means of baffles and flow straightening screens. A standard bellmouth inlet is installed in the plenum just forward of the compressor rig with enough room for inlet distortion screens between the compressor and the bellmouth, if necessary. Interstage compressor bleed is extracted between the fourth and fifth stages through an annular duct around the compressor approximately 61 cm (24 in.) long, which feeds six collector manifolds. These six manifolds each feed 12.7 cm (5 in.) diameter pipes, which are located at 60 deg, 90 deg, 120 deg, 240 deg, 270 deg, and 300 deg from TDC, respectively. The compressor rig is tested at a reduced inlet pressure but at proper corrected flow and rotor speed. Since the bleeds are usually subatmospheric, they are ducted back to the stand inlet flow duct between the controlling orifice and the plenum, upstream of the flow straightening baffles. The interstage bleed flows were run per normal operating schedule except for one test, during which the bleeds were not opened. Provisions for customer bleed are located on the inner combustor case downstream of the diffuser struts and diffuser dump section (figure 1). However, the customer bleed was not considered to have any significance in this program because of its distance from the compressor discharge instrumentation plane. The airflow undergoes diffusion and a sudden expansion between the compressor discharge and

customer bleed ports. The exhaust from the rig is collected in a manifold and dumped to atmosphere, or put through an exhauster. The compressor is coupled to a steam turbine that drives the compressor clockwise, looking upstream.

All pressures were recorded using a scanivalve and pressure transducer system. The scanivalves were connected to ΔP transducers with a range of 10.34 N/cm^2 (15 psid). All transducers were referenced to the same pressure, which was accurately determined. An error analysis on the C-3 stand pressures indicated a measurement uncertainty within ±0.0758 N/cm^2 (0.11 psi). Temperature data were taken using half-shielded chromel/alumel (C/A) thermocouples, except in Build 206, which used 5-point C/A thermocouple rakes with Kiel-type heads. Both measured the temperature with an uncertainty less than ±1.111°K (2°R). The output of the transducers and thermocouples was fed into an automatic data recording system, which supplied reduced data in engineering units.

Several variables were studied in the J58 compressor rig at two important conditions: SLTO and cruise. Among those variables were aerodynamic inlet distortion, indexing of stators, modified shrouds, and modified seals. Table I shows the comparisons to be presented in this study by run number. The inlet distortion was produced by an inlet screen (figure 6), which was used at the cruise condition to simulate inlet total pressure distortion seen at that flight condition. The distortion typically generated by the screen is shown in figure 7 as an inlet pressure distribution map. The indexing of stators consisted of rotating the first four stages 36 deg counterclockwise (ccw), looking upstream. The modification of interstage seals consisted of replacing, depending on the build, the sheet metal or honeycomb seals with Feltmetal or filled honeycomb, abradable-type seals and reducing the seal clearances. The modification to the shrouds consisted of replacing the sheet metal with Feltmetal in stages 5 through 9.

F100/F401 High Compressor Rig and Instrumentation

The F100/F401 high compressor is used in the advanced state-of-the-art turbofan engine that will power the F-15/F-14B air superiority fighter aircraft. The high compressor is a single-spool, variable stator design with a nominal pressure ratio of 8:1. The compressor is shown schematically in figure 2 along with a table describing each stage.

To analyze the compressor discharge airflow of the F100/F401, it was first necessary to obtain data with a sufficient number of total pressure and total temperature probes at the compressor discharge plane. As the F100/F401 is in the development phase, a high compressor rig was being tested while this program was being worked on. Through cooperation of the Air Force and Navy, permission was obtained to install the necessary instrumentation and gather data on a noninterference basis. The instrumentation was designed and fabricated under this program and consisted of total pressure rakes with five Kiel-type heads located on centers of equal area, total temperature rakes with five Kiel-type heads shielding chromel/alumel thermocouples, again on centers of equal area, and finally, static pressure taps for the annulus inner and outer walls. Typical probes are shown in figure 8. Twenty-two total pressure rakes (four of which were regular rig instrumentation), ten total temperature rakes (again four of which were regular rig instrumentation), ten OD static pressure taps, and ten ID static pressure taps were used as shown in figure 9 to obtain the

circumferential and radial pressure and temperature profiles necessary to calculate airflow deviation.

The compressor tested during this program is the version used in development flight engines and is typical of the production engine high compressor. The compressor rig was tested at a reduced pressure, but at proper corrected flow and rotor speed. The compressor rotates clockwise, looking upstream. The stators are variable in stages 4 through 6, and are adjustable in the remaining stages. The variable stators were operated per normal schedule with the adjustable stators in an optimized configuration for the rig build. The rig was tested in the East Hartford test stand X-27. This facility is essentially the same type of stand as that used to test the J58 compressor rig. The facility has an atmospheric inlet upstream of a flow-controlling butterfly valve. The air is fed to a cylindrical plenum, which is approximately 2.134 m (7 ft) dia x 3.048 m (10 ft) long. Although this plenum is considerably smaller than the FRDC C-3 stand plenum, the ratio of rig inlet flowpath diameter to plenum diameter for each rig is similar. Flow straightening is accomplished by baffles and screens in the forward section of the plenum. A standard bellmouth inlet is installed in the plenum just forward of the compressor rig with space for inlet distortion screens downstream of the bellmouth. Provisions for extracting customer bleed through the trailing edge of the blunt-ended diffuser struts are included in the rig. However, the customer bleed was not considered significant because of its distant location from the compressor discharge instrumentation plane. The trailing edge of the diffuser struts, where the bleed ports are located is in the plane of the diffuser dump section so the airflow is diffused and subjected to a sudden expansion between the compressor discharge and the customer bleed location. The exhaust from the rig is collected in a doughnut shaped manifold downstream of the diffuser case and exhausted to ambient or through an exhauster. The compressor is coupled to a turboshaft engine through a gearbox which rotates the rig clockwise looking upstream.

All pressures were recorded using a scanivalve and pressure transducer system. The pressures were read as absolute values and every other port was referenced to vacuum. The vacuum readings were checked to ensure agreement between transducers. The uncertainty is less than ± 0.069 N/cm^2 (0.1 psi) on absolute pressures. The total temperatures were taken by five-point temperature rakes with chromel/alumel thermocouples with an uncertainty of less than ± 1.111°K (2°F). The output of the transducers and thermocouples was fed into an automatic data recording system, which supplied reduced data in engineering units.

During all high compressor rig tests, a total pressure distortion screen was present over the outer 30% of the inlet annulus. Distortion generated by this screen simulated the fan pressure profile entering the high compressor. The screen mesh used was 3 x 3 x 0.0248 cm (0.063 in.). An additional total pressure distortion screen, 4 x 4 x 0.0248 cm (0.063 in.) mesh, was located over the compressor inlet from 165 deg to 345 deg clockwise, looking upstream, when desired, to provide circumferential aerodynamic distortion. Thermal distortion is accomplished by splitting the inlet duct in half and heating half the air by means of a heater burner system. The same 180 deg sector covered by screens for aerodynamic distortion was heated for thermal distortion. The heater burner system allowed for ΔT's of 22°K (40°F) and 55°K (100°F) by blending of ambient air downstream of the heater burners to reach the desired ΔT.

DATA ANALYSIS

To analyze the information obtained at the compressor discharge plane of both the J58 and F100/F401 compressor rigs, a data reduction program was formulated that allowed for computer-generated plots of the input total temperature and pressure profiles as well as the local and circumferential airflow deviation for each test case. The latter sets of computer plots show conclusively the areas of high and low airflow at the compressor discharge that are being fed into the diffuser-combustor system. These plots allow for comparisons between variables in different builds to indicate their effect on airflow deviation.

The input necessary for this program consists of total pressure profiles, $P_{t_{i,j}}$, total temperature profiles or points, $T_{t_{i,j}}$, and static pressures, $P_{s_{i,k}}$, at various circumferential locations. The profile descriptions can have up to seven values per circumferential location. The diffuser annulus radii to the inner and outer walls are required at the plane of the static pressures and the plane of the total pressures. The average static pressure at the plane of the total pressures is found by adjusting the static pressure for the area change to the plane of the total pressure if the static is not in the exact plane of the total pressure. The span location, i.e., probe head location between inner and outer walls of the annulus, is also necessary for the total pressures and temperatures. From these input items the data reduction program can calculate and generate plots at the compressor discharge of average circumferential airflow deviation, average square root of dynamic pressure ratio, and local airflow deviation, usually referred to as the local airflow map.

The engineering formulation of the data reduction program is presented below. All symbols not defined in the text are in the list of symbols. Several integers and subscripts are used in this formulation and are defined here for clarity:

- i is circumferential location
- j is radial location or associated with a radial location
- k is indicator for ID or OD
- L is indicator, = 1 for J58, = 2 for F100/F401
- m is number of total pressure rakes
- m1 is number of total temperature rakes
- n is number of static pressure circumferential positions.

The compressor discharge area at the plane of the total pressure rakes is:

$$A_t = \pi (R_{OD_{t,L}}^2 - R_{ID_{t,L}}^2)$$

and the area at the plane of the static pressures is:

$$A_s = \pi (R_{OD_{s,L}}^2 - R_{ID_{s,L}}^2).$$

The average static pressure at an input circumferential location is:

$$P'_{s_{i,avg}} = \frac{1}{2} \sum_{k=1}^{2} P_{s_{i,k}}$$

while the average total temperature at an input circumferential location is:

$$T_{t_{i,avg}} = \frac{1}{nn} \sum_{j=1}^{nn} T_{t_{i,j}} + 459.7$$

where when L = 1, nn can be = 1, 2, or 5
when L = 2, nn = 5.

Note that, if any values to be used in the summations are zero, they are eliminated from the average. These quantities are now used with an interpolation scheme so that appropriate values at the total pressure circumferential locations can be obtained.

The overall average total temperature and static pressure are calculated by:

$$T_{t_{avg,ov}} = \frac{1}{m1} \sum_{i=1}^{m1} T_{t_{i,avg}} \quad \text{and} \quad P_{s_{avg,ov}} = \frac{1}{n} \sum_{i=1}^{n} P'_{s_{i,avg}}$$

The input values of total pressure are scanned and any values below local average static pressure are discarded. The average total pressure for each rake is then computed as:

$$P_{t_{i,avg}} = \left(\sum_{j=1}^{nm} A_j P_{t_{i,j}} \right) / A_t$$

where

nm = 7 when L = 1

nm = 5 when L = 2.

The average static pressure at the plane and location of the total pressure rakes is found by interpolation at the appropriate circumferential location, and then adjusting that value for the area change to the plane of the total pressures to obtain:

$$P_{s_{i,avg}} = P_{t_{i,avg}} - \left(\frac{A_s}{A_t} \right)^2 \left[P_{t_{i,avg}} - P'_{s_{i,avg}} (\theta_i, P_{t_{i,avg}}) \right]$$

It is recognized that this expression is for incompressible flow but the Mach number is low and the area ratio is small so that the discrepancy is negligible.

To obtain the airflow parameters it is first necessary to evaluate the Mach number at each probe head and for each rake. This is done in an iteration loop

that initially guesses the static temperature to evaluate γ_i or $\gamma_{i,j}$ (Reference 2), then solves for

$$M_{i,j} = \left(\frac{2}{\gamma - 1} \left[(Pt_{i,j}/Ps_{i,avg})^{\frac{\gamma-1}{\gamma}} - 1 \right] \right)^{1/2}, \qquad \gamma = \gamma_{i,j}$$

$$M_i = \left(\frac{2}{\gamma - 1} \left[(Pt_{i,avg}/Ps_{i,avg})^{\frac{\gamma-1}{\gamma}} - 1 \right] \right)^{1/2}, \qquad \gamma = \gamma_i$$

The static temperature is then calculated from the isentropic relation

$$Ts_{i,j} = Tt_{i,avg} \Big/ \left(1 + \frac{\gamma-1}{2} M_{i,j}^2 \right), \qquad \gamma = \gamma_{i,j}$$

$$Ts_i = Tt_{i,avg} \Big/ \left(1 + \frac{\gamma-1}{2} M_i^2 \right), \qquad \gamma = \gamma_i$$

and used as the guess in the next iteration. This iteration loop is closed, and the correct values obtained, when the static temperature is within one degree of the guessed value. This is less than 0.2% in most cases.

The airflow parameters and final averages are obtained by:

Local airflow per unit area is:

$$(W/A)_{i,j} = \left(\frac{\gamma g}{\mathcal{R} Tt_{i,avg}} \right)^{1/2} \left(1 + \frac{\gamma-1}{2} M_{i,j}^2 \right)^{-\frac{\gamma+1}{2(\gamma-1)}} M_{i,j} \, Pt_{i,j}, \qquad \gamma = \gamma_{i,j}$$

Average airflow per unit area is:

$$(W/A)_i = \left(\frac{\gamma g}{\mathcal{R} Tt_{i,avg}} \right)^{1/2} \left(1 + \frac{\gamma-1}{2} M_i^2 \right)^{-\frac{\gamma+1}{2(\gamma-1)}} M_i \, Pt_{i,avg}, \qquad \gamma = \gamma_i$$

The uncertainties involved in the local airflow per unit area and the average airflow per unit area were calculated from the measurement inaccuracies of the pressures and temperatures. For the J58 compressor, the uncertainty in local airflow per unit area was 1.6% and the uncertainty in average airflow per unit area was 2.5%. For the F100/F401 compressor, these uncertainties were 1.6% and 1.4%, respectively.

Overall average airflow per unit area is:

$$(W/A)_{avg,ov} = \frac{1}{m} \sum_{i=1}^{m} (W/A)_i$$

Local airflow ratio is:

$$W_{i,j}/W_{avg,ov} = (W/A)_{i,j} \, A_j / (W/A)_{avg,ov} \, A_t$$

Percent airflow deviation is:

$$\text{Deviation} = [(W/A)_i/(W/A)_{avg,ov} - 1] \times 100$$

Average total pressure is:

$$P_{t_{avg,ov}} = \left[\sum_{i=1}^{m} P_{t_{i,avg}} (W/A)_i \right] \Big/ \sum_{i=1}^{m} (W/A)_i$$

Dynamic pressure at each rake is:

$$Q_{i,avg} = P_{t_{i,avg}} - P_{s_{i,avg}}$$

Average dynamic pressure is:

$$Q_{avg,ov} = \left[\sum_{i=1}^{m} \left[P_{t_{i,avg}} - P_{s_{i,avg}} \right] (W/A)_i \right] \Big/ \sum_{i=1}^{m} (W/A)_i$$

The output from the data reduction program consists of computer-generated plots of (1) radial total pressure and total temperature profiles; (2) circumferential total pressure, total temperature, and static pressure profiles; (3) circumferential airflow deviation profiles; (4) circumferential square root of dynamic pressure ratio variation; and (5) the local airflow deviation map. All of these plots will be discussed in detail.

RESULTS

J58 Compressor Rig

The data analyzed during this study were acquired from two J58 compressor rigs during seven builds. Twelve points were chosen at conditions of sea level takeoff (SLTO) and supersonic cruise with variables, including inlet aerodynamic distortion, modified seals, modified shrouds, and indexing of stators. Table I indicates the matrix of variables examined. Because of the large quantity of data generated at each test point, only the results are presented here. The input data for each case, along with the radial and circumferential computer-generated profile plots of the compressor discharge total pressures, temperatures, and static pressure are presented in Reference 1. Also given for each case in Reference 1 is a computer-generated plot of the average circumferential variation of the square root of dynamic pressure. It should be pointed out that the term IDENT, used in all figures, refers to the rig-build-run numbers and that θ/θ_{max}, used to indicate circumferential location, starts at top dead center and proceeds clockwise, looking upstream.

The compressor for the first build, rig 30204, build 10, was an engine Bill-of-Material (B/M) configuration. Three cases were analyzed: SLTO, and cruise with and without inlet aerodynamic distortion. The compressor discharge average circumferential airflow deviation for the SLTO condition is shown in figure 10. A four-lobe, nearly cyclic pattern of high and low flow areas is apparent, with peaks ranging from 20% above average to 33% below average, for a difference of 52%. This term, the difference between the highest and lowest values of circumferential airflow deviation, is a convenient indicator of overall airflow nonuniformity and is used throughout this report for comparing different variables and builds. The airflow map for this test is shown in figure 11. The

four areas of high and low airflow are again apparent, with the areas of high flow located near midspan of the compressor on horizontal and vertical centerlines. For this case the maximum local deviation is 52% above average whereas the minimum is 88% below average. The absolute values of the maximum and minimum local airflows are not considered to be particularly significant in themselves but do indicate the extremes of airflow variation when they lie in a large area of high or low airflow. Results associated with each test case are given in table III and provide the best method of comparing results of the different variables. The circumferential airflow deviations and local airflow ratios are presented, along with the average test conditions at the compressor discharge.

Results of the test at cruise conditions are shown in figures 12 and 13. The four-lobe pattern of high and low airflow is still present but the magnitude of flow variation is greatly reduced. The circumferential airflow difference is only 27% as compared to 52% at the SLTO condition. The airflow map shows the areas of high flow have moved towards the hub of the compressor and the flow pattern has shifted about 45 deg in angular location relative to the SLTO test (figure 11). Results of the test at cruise conditions with inlet aerodynamic distortion are shown in figures 14 and 15. The distortion imposed at the inlet was presented as a pressure distribution map in figure 7. The presence of inlet distortion produced little change in the circumferential airflow deviation, other than to increase the difference between highest and lowest deviations by 4% to 31%. The airflow maps with and without inlet distortion are nearly identical.

For the next two tests, the compressor was modified by installing reduced clearance, abradable type seals, in the first four stages to reduce interstage leakage. This configuration, Build 11, was tested at SLTO and cruise-distorted conditions. Results are shown in figures 16 through 19. The airflow uniformity is greatly improved, with the circumferential airflow deviation difference dropping to 19% at SLTO and 18% at cruise-distorted conditions. These values compare with 52% and 31%, respectively, for the compressor with B/M seals. Detailed comparison of the airflow maps for this compressor and the B/M compressor (figures 11 and 17 for SLTO and figures 13 and 19 for cruise-distorted) shows the reduced clearance interstage seals did, in fact, reduce interstage leakage because the airflow rate is increased at the hub of the compressor. The four-lobe cyclic airflow distribution observed with the B/M compressor is still clearly present at cruise-distorted conditions. Its presence at SLTO is questionable but the airflow map does show high flow areas at midspan on the horizontal and vertical centerlines, as were present in the B/M compressor.

The compressor was next modified by installing reduced clearance interstage seals throughout the compressor to further reduce interstage leakage (Build 12). These seals were constructed of Feltmetal rather than the abradable material used in the first four stages of the previous build. The compressor was tested at SLTO and cruise-distorted conditions. The results are shown in figures 20 through 23. The circumferential airflow deviation difference is 19 and 27% for SLTO and cruise-distorted conditions, respectively. This is much improved over the B/M compressor with values of 52 and 31%, but is inferior to the 19 and 18% obtained from the previous build with reduced clearance interstage seals in the first four stages. Detailed comparison of the airflow maps explains this discrepancy. The compressor with tight seals throughout actually

had more interstage leakage effects than the previous build with tight seals in only the first four stages. This is evidenced by the larger areas of low airflow rate at the hub of the compressor with tight seals throughout (compare figure 17 with 21 and figure 19 with 23) and indicates that the Feltmetal seals were less effective than the abradable seals. They were, however, more effective than the B/M seals during the SLTO test (compare figure 21 with 11) and hence produced more uniform airflow than the B/M configuration. When the airflow maps for tight interstage seals throughout and B/M configurations at cruise-distorted conditions are compared, it appears that the tight seal configuration has more interstage leakage than the B/M (compare figure 23 with 15). This can be explained in part by the fact that about 65 hours of testing occurred between the two data points on the tight seal compressor. Thus, the seals may have worn considerably by the time the cruise-distorted point was taken. In spite of the apparent relatively high seal leakage of the tight seal compressor at the cruise-distorted test condition, it provided more uniform airflow than the B/M configuration. The circumferential airflow deviation differences for the two are 27 and 31%. This deviation is explained by the fact that the tight seal compressor, even after wear had occurred, had more circumferentially uniform airflow on the hub than the B/M compressor (figures 23 and 15). The tight seal compressor had a line of average airflow of 70% around most of the hub circumference and an 80% line, which is continuous at a near-constant distance off the hub. This is in contrast to the B/M airflow map, figure 15, which shows airflow rates around the hub ranging from 70 to 110% of average. Apparently the leakage of the worn tight seals is more circumferentially uniform than the B/M seals and thus circumferential airflow distribution is more uniform. Examination of the tight seal compressor airflow maps also shows the same characteristic four-lobe pattern of high flow at midspan seen in previous builds.

A second J58 compressor rig, 30239, was used for the rest of the J58 compressor testing described in this report. This rig is similar to rig 30204, but it brought a different set of compressor hardware into the program. The first test with rig 30239, Build 202, was with a B/M compressor except that the B/M honeycomb tip shrouds had been replaced with Feltmetal tip shrouds in stages 5 through 9. This configuration was tested only at SLTO. Results are shown in figures 24 and 25. The circumferential airflow deviation difference is 29%. This value, compared to the 52% obtained with a B/M compressor in rig 30204, indicates a significant improvement in airflow uniformity attributable either to the Feltmetal tip shrouds or to unknown differences between the two compressors. This deviation difference is not as good, however, as the tight interstage seal compressor values of 19% obtained in the previous rig. The airflow map again shows four areas of high airflow at midspan on the vertical and horizontal centerlines.

For the next test, the Feltmetal tip shrouds were replaced with B/M honeycomb shrouds, and the stators in stages 1 through 4 were indexed 36 deg counterclockwise, looking upstream. The configuration (Build 203) was therefore B/M except for the indexing of the stators. This configuration was tested at SLTO giving the results shown in figures 26 and 27. The circumferential airflow deviation difference dropped to 19%, which is similar to that obtained from the other compressor when reduced clearance interstage seals were installed. The airflow map again displays four areas of high airflow at midspan on the vertical and horizontal centerlines.

The forward stators (stages 1-4) were indexed back to the B/M position in Build 204 and testing was again performed at SLTO conditions. This compressor was entirely B/M. The results are shown in figures 28 and 29 and are practically identical to the results of the previous test with the forward stators indexed. The circumferential airflow deviation difference for both compressors is similar, about 20%. Comparison of the airflow map of this compressor with that of the compressor with Feltmetal tip shrouds (figures 24 and 25) shows that the two machines have similar airflow patterns except on the tip in the area between 1 and 5 o'clock. This difference apparently produced the 10% higher circumferential airflow difference for the Feltmetal shrouded compressor. The localized low tip airflow of the Feltmetal shrouded compressor leads to the speculation that one of the shrouds was eccentric with large clearance in the area of low tip airflow. Comparison of results from this compressor with the other B/M compressor tested during the program reveals striking differences for supposedly identical compressors (compare figures 32 and 33 with 10 and 11). The airflow map for the first B/M compressor shows much larger areas of low airflow on both the hub and tip of the compressor than the second B/M compressor. The circumferential airflow deviations for the two compressors are 52 and 20%, respectively. As the two compressors are thought to be identical, the cause of this large difference cannot be isolated, other than to speculate that the second machine was "tighter" in hub and tip seal clearances than the first. The four-lobe pattern of high airflow at midspan is present in both compressors.

For the next Build, 206, the second B/M compressor was rebuilt with foreign object damaged rotor blades in stages 2 through 9. The machine was again B/M except for the damaged blading. Tests were conducted at both SLTO and cruise-distorted conditions with this compressor. Results are shown in figures 30 through 33. Circumferential airflow deviation differences for SLTO and cruise-distorted conditions are 19 and 23%, respectively. The four-lobe high airflow pattern is again clearly present in the cruise-distorted test but is indexed 45 deg from its usual oricntation half-way between horizontal and vertical centerlines. At SLTO, the airflow map is more indicative of an eight-lobe pattern. Except for the damaged blading used in this build, the results are directly comparable to the other two B/M builds. Overall airflow characteristics are similar to the second B/M compressor but quite different from the first B/M compressor. No specific cause for these variations can be offered. Airflow distribution is obviously sensitive to subtle build-to-build variations.

F100/F401 High Compressor Rig

The compressor tested during this program is the version of the F100/F401 high compressor used in development flight engines. The rig, 34017, underwent two builds during the program, with the detailed compressor discharge instrumentation shown in figure 9. During the first build, 204, the only variables available were the test conditions: SLTO, subsonic cruise, and combat. The second build, 205, was essentially the same compressor, but it was tested with inlet aerodynamic distortion and two levels of thermal distortion at the various test conditions. The combination of variables analyzed for these builds is shown in table I. As in the J58 compressor results, the compressor discharge total pressure, total temperature, and static pressure are given as computer-generated radial and circumferential plots and in tabular form in Reference 1. Also given in Reference 1 is a plot of average circumferential variation of the square root of the dynamic pressure for each case.

Results from tests of Build 204 are presented in figures 34 through 39, and in table IV. (Results for all F100/F401 tests are presented in this table.) Circumferential airflow deviation differences for the SLTO, subsonic cruise, and combat test conditions are 13, 11, and 16%, respectively. The airflow maps for the three tests are quite similar and show none of the cyclic circumferential airflow variation observed in the J58. A second difference relative to the J58 is the presence of high airflow on the compressor hub. The J58 compressor consistently delivered low airflow on the hub and nonuniformity appeared to be related to the radial depth of the low airflow. The F100/F401 compressor has its highest airflow near the hub and in this test series provided more uniform airflow than the J58 compressor.

One of the purposes of Build 205 was to permit study of distortion effects on compressor performance. Several sets of data were obtained with and without aerodynamic distortion and different amounts of thermal distortion. The first set of tests generated nondistorted inlet data for comparison with Build 204 and subsequent tests with inlet distortion. The inlet pressure and temperature maps are given in figures 40 and 41 at the SLTO condition. They were obtained with eight equally spaced five-point total pressure rakes and an equal number of total temperature rakes at the locations shown. Maps for the cruise and combat points were very similar and are not shown. Results of the baseline case are presented in figures 42 through 47. During the taking of data for these cases, a scanivalve switch was not activated. Thus, no pressures were recorded over the segment 83.5 deg to 150 deg. For the SLTO test case, the average circumferential airflow deviation (figure 42) ranges from 8% above to 11% below average. The local airflow deviation map (figure 43) still has the areas of high airflow on the hub. Both the cruise and combat conditions show similar characteristics with about 15% in circumferential airflow deviation difference and high airflow areas located on the hub.

Aerodynamic distortion was generated by a screen installed at the compressor inlet from 165 deg to 345 deg clockwise, looking upstream. The pressure map obtained at the inlet is presented in figure 48; one side is mostly below average, the other above. The temperature map is similar to figure 41. Results of tests at all flight conditions are presented in figures 49 through 54. The SLTO condition results (figures 49 and 50) indicate an increase from 19 to 23% in airflow deviation due to the screen. The airflow map is similar to the baseline (figure 43). As in the baseline case, cruise and combat conditions give similar airflow deviations (figures 51 and 53) and flow maps (figures 52 and 54).

Combined aerodynamic and thermal inlet distortion was tested in the next series. The thermal distortion was imposed by heating the inlet airflow over the same 180-deg sector on which screens were installed for aerodynamic distortion. Two thermal distortions were tested, $\Delta T = 22\,^{\circ}K$ (40 °F) and 55 °K (100 °F), over the range of test conditions. For $\Delta T = 22\,^{\circ}K$ (40 °F), the compressor inlet total pressure and temperature maps are given in figures 55 and 56. Results with a thermal distortion of $\Delta T = 22\,^{\circ}K$ (40 °F) are presented in figures 57 through 62. The SLTO case shows another increase in average circumferential airflow deviation to 27% (figure 57). The local airflow map (figure 58) indicates an area of high airflow from approximately 30 deg to 230 deg and low airflow over the remainder. This indicates a rotation or swirl of the distortion of about 45 deg through the compressor. The cruise and combat test data show the same results (figures 59 to 62). An increase in thermal

distortion to $\Delta T = 55°K$ (100°F) drastically increased the average circumferential airflow deviation difference to 34% for SLTO and higher for the other test conditions. The inlet pressure and temperature maps for the SLTO condition are given in figures 63 and 64. The results of all three test conditions (figures 65 through 70) show the increase in airflow deviation and the rotation of the distortion by about 45 deg. The areas of high airflow are still on the hub but seem to have expanded.

When the aerodynamic distortion is removed and the thermal distortion set to $\Delta T = 22°K$ (40°F), the compressor inlet characteristics, given as total pressure and temperature maps, are shown in figures 71 and 72. Results from these test conditions are given in figures 73 through 78. The average circumferential airflow deviation is about 22% for all cases. At SLTO the local airflow map shows high airflow areas in four locations off the hub. The cruise and combat points do not show the same characteristic, however. When the thermal distortion was increased to $\Delta T = 55°K$ (100°F), the inlet total pressure map (figure 79) remained the same but the inlet total temperature variations (figure 80) were exaggerated. The SLTO compressor discharge characteristics are similar to those found previously with combined aerodynamic distortion and $\Delta T = 55°K$ (100°F). The average circumferential airflow deviation (figure 81) is 17% from average. The distortion remains rotated about 45 deg clockwise looking upstream. The areas of high airflow as shown on the flow map (figure 82) are mainly on the hub.

DISCUSSION OF RESULTS

The J58 and F100/F401 compressors show a degree of compressor discharge airflow nonuniformity not previously documented. As these two compressors encompass state-of-the-art compressor design, it is highly probable that comparable airflow nonuniformity exists in other compressors. This nonuniformity had not been previously observed because normal compressor development instrumentation does not provide discharge measurements at a large number of circumferential locations, and the variations that are observed are usually dismissed as instrumentation errors or exit guide vane (EGV) wake effects. In this program, however, the compressors were instrumented at many circumferential locations, care was taken to ensure accuracy of the measurements, and exit guide vane wake effects can be judged insignificant by inspection of the data.

Rigs were instrumented with five- or seven-point total pressure rakes at a minimum of twenty circumferential locations, single or five-point total temperature rakes at a minimum of ten circumferential locations, and wall static pressure taps were spaced around the annulus on the outer and inner diameters at up to ten locations. Typical instrumentation locations were shown in figures 4, 5 and 9. The measurement uncertainties were within $\pm 0.0758\ N/cm^2$ (0.11 psi) on pressures and $\pm 1.11°K$ (2°R) on temperatures. The difference between average total and static pressures on all tests was $1.38\ N/cm^2$ (2 psi) or greater and the variation within total pressures on each test was $2.76\ N/cm^2$ (4 psi) or greater. Thus the $\pm 0.0758\ N/cm^2$ (0.11 psi) instrumentation uncertainty is small relative to the pressure variations encountered. Temperature variations were on the order of 11.1°K (20°R) or higher, so the temperature uncertainties are a small effect, particularly since the absolute temperatures were about 555.6°K (1000°R). Thus, a 1.11°K (2°R) error is only 0.2% error in absolute temperature.

The criticism that compressor discharge airflow nonuniformity data are unreliable because the exit guide vanes influence only some of the total pressure rakes and not others, is refuted by a study of a specific case for each compressor. For the J58 compressor rig, the data from the cruise-distorted test in rig 30204, Build 10 were used. The circumferential position of each rake was determined relative to its nearest stator trailing edge and the local total pressure ratio plotted (figure 83). No pattern of EGV wake influence is discernable, although enough data points were taken to give adequate definition to any trends. Since there are twice as many 9th-stage stator vanes as EGV's this plot also indicates no pattern of 9th-stage stator vane influence. For the F100/F401 high compressor, the subsonic cruise condition with aerodynamic and thermal distortion was analyzed in a manner similar to the J58 case mentioned previously. Again, although sufficient data were available (figure 84), no pattern of EGV wake effects could be found. Stator vanes and EGV's are known to produce local wakes but the instrumentation planes in both rigs are far enough downstream that the local wakes have dissipated.

Results of this study have been presented in two forms: computer-generated plots (figures 10 through 82) and tables (tables III and IV). Because of the many test conditions and combinations examined while reducing the data from the J58 and F100/F401 compressor rigs, tables I, III, and IV are the easiest to use. Table I presents the matrix of variables and test conditions analyzed. Table III gives the reduced data for the J58 compressor, whereas table IV has the F100/F401 high compressor reduced data. Several parameters are presented for comparison in tables III and IV. Among these are the circumferential airflow maximum deviation, minimum deviation, and difference; the local airflow ratio maximum and minimum; the number of high and low deviation areas; and the number or location of the locally high airflow areas. Also presented are the overall averages of the compressor discharge variables.

The parameter that displays the nonuniformity of the compressor discharge airflow most dramatically for each case is the circumferential airflow deviation difference. For the J58 compressor, this parameter ranges from 18 to 52%. The greater the deviation difference, the greater the nonuniformity of flow leaving the compressor. All the J58 compressor tests investigated show relatively high nonuniformity of compressor discharge airflow. The worst case investigated was the SLTO test condition of rig 30204, Build 10, which had a circumferential airflow deviation of +20% to -33% and a maximum local airflow ratio of 52%. Four areas of locally high airflow were distributed about 90 deg apart starting at TDC. The other two test conditions for this build were slightly better, with a low of 27% circumferential airflow deviation difference but the same local characteristics.

In Builds 11 and 12 of the same rig, modifications to the interstage seals brought the circumferential airflow deviation differences down below 20%, but the maximum local airflow ratios remained high, 33 to 39%. The reduced clearance interstage seals in stages 1 through 4 of Build 11 reduced the interstage leakage as evidenced by the increase in airflow rate at the compressor hub. A further modification to the interstage seals in Build 12 extended the tightened seals through stage 9 and made use of Feltmetal to replace the abradable-type seal. This change, however, showed no improvement over Build 11. In fact the cruise-distorted test point was more nonuniform than the same case in Build 11, probably due to seal wear since about 65 hours of testing occurred between the two test points of Build 12. During both builds the four-lobe pattern remained in evidence, although somewhat hidden in the SLTO case of Build 12.

Rig 30239, Build 202, was a B/M configuration with modified tip shrouds. This build was tested at SLTO only and showed a circumferential airflow deviation difference of 29%, as compared to the 19% deviation obtained in the previous rig with tight interstage seals. The differences, however, can not be attributed strictly to the shrouds, but could be caused by unknown differences in the two compressor rigs. The next build, 203, returned to the B/M honeycomb shrouds but indexed the first four stator stages 36 deg clockwise, looking upstream. This configuration was also tested at SLTO only and resulted in a circumferential airflow deviation difference of 19%, which is the same as the SLTO cases of the previous rig with tight interstage seals. The stators were returned to B/M position for Build 204, giving a complete B/M configuration. The SLTO tests showed essentially no difference between Builds 203 and 204. Indexing of stators, therefore, does not seem to have an effect on discharge airflow uniformity. Comparison of the SLTO points from Builds 11 and 12 of rig 30204 and Builds 203 and 204 of rig 30239 shows about the same uniformity for all builds; this indicates that the second rig, 30239, probably had tighter B/M seals to start with. The final build, 206, was a B/M compressor with foreign-object-damaged blades. The circumferential airflow deviation difference for the two conditions analyzed, SLTO and cruise-distorted, was similar to those of the previous builds and no conclusion about foreign-object-damaged blading can be drawn. The four-lobe pattern of airflow ratio and deviation is still evident in all cases.

For the F100/F401 high compressor, an average circumferential airflow deviation difference for the baseline case is about 13% for Build 204 and 15% for Build 205 of rig 34017. The high and low deviations (table IV) are somewhat different for each build. When aerodynamic distortion is imposed, the average circumferential airflow deviation difference increases to about 19%. For aerodynamic and thermal distortion, the difference becomes 26% for $\Delta T = 22\,^{\circ}K$ ($40\,^{\circ}F$) and 37% for $\Delta T = 55\,^{\circ}K$ ($100\,^{\circ}F$). When only thermal distortion is imposed, the average circumferential airflow deviation difference is 22% for the low ΔT and 35% for the high. These comparisons show that for the levels of distortion tested the thermal distortion increases nonuniformity more than does aerodynamic distortion by a substantial amount. Typically, aerodynamic distortion increased the circumferential airflow deviation difference about 3-4%, thermal distortion of $22\,^{\circ}K$ ($40\,^{\circ}F$) increased the difference by 6-7%, and thermal distortion of $55\,^{\circ}K$ ($100\,^{\circ}F$) increased the difference by 18-19%. Effects of the aerodynamic and thermal distortion seem to be additive in that the increases in average circumferential airflow deviation difference attributable to the aerodynamic or thermal distortions separately may be numerically added to the baseline to obtain the same deviation difference resulting from testing with combined distortions. In most cases the local high flow is concentrated on the compressor hub. The maximum local airflow ratio for all cases was 40% above average. In general, the F100/F401 high compressor airflow is more uniform than that of the J58 compressor but it is still relatively nonuniform.

Possible causes of compressor airflow nonuniformity are many, and while isolation of specific causes and effects is generally beyond the scope of this program, a discussion of some of the more obvious possible causes and pertinent results follows.

Stator Orientation - Because the performance of a stator passage is affected by upstream flow properties, a repeating pattern of varying stator wake alignment around the compressor could produce a repeating pattern of varying airflow rate around the compressor. The number of times the pattern repeats around the circumference should be equal to the highest common integral factor of the number of vanes per stage. In the case of the J58 the highest common factor for all stages is two, but no two-cycle pattern was observed. The first four rows of stator vanes were indexed to break up the pattern and no change in the outlet flow field was noted. However, the last five stages, which were not indexed, have a common factor of four and a four-cycle pattern of high and low airflow around the circumference was observed. This suggests that the four-cycle pattern was a result of the orientation of the stator vanes in the last five stages of the J58 compressor. This cannot be construed as positive proof of the source of the four-cycle pattern as it was not possible to index the individual stages and change the orientation of the stator vanes. In the F100/F401 compressor, the largest common factor for all stages is two, and the last three stages have a common factor of six, but no cyclic pattern corresponding to these values was observed. Thus, the data available on this subject are inconclusive but do lend some support to the theory of stator vane orientation being a source for generating circumferential variations in compressor discharge airflow.

Bleed Ports and Bleed Extraction - The presence of bleed ports or local extraction of airflow could locally alter the compressor aerodynamics and produce nonuniform airflow at the compressor discharge. Both the J58 and F100/F401 compressor rigs had provision for customer bleed. The J58 compressor rig also had provision for interstage bleed. Customer bleed was not considered in this program because its location was far removed from the compressor discharge instrumentation plane. In the J58, the customer bleed ports were located downstream of the diffuser, on the inner burner case wall. Thus, the airflow underwent diffusion and a sudden expansion between the compressor discharge and the location of the customer bleed ports. In the F100/F401 compressor, the customer bleed ports were located in the blunt trailing edge of the diffuser struts. The diffuser struts ended at the diffuser dump section, so again the airflow encounters diffusion and sudden expansion between the compressor discharge and customer bleed port locations.

The J58 interstage bleed was operated per normal schedule for all but one test, but no data were generated with varied bleed flow at the same condition with the same compressor. Thus, no conclusions can be drawn concerning bleed effects.

Circumferentially Nonuniform Tip and Seal Clearances - Any circumferentially nonuniform feature of the compressor, such as nonuniform tip or seal clearances, is likely to cause nonuniform airflow due to circumferentially varying leakage and performance levels. No known hardware circumferential nonuniformities were tested during this program, so no conclusive data are available on this subject.

Seal Leakage - Throughout this program, airflow nonuniformity appeared to be strongly related to interstage seal leakage. Seal leakage could not be correlated with known variations in seal clearances but whenever seal leakage was small, as evidenced by the presence of high airflow near the compressor hub, the compressor discharge airflow was relatively uniform. Increased seal leakage increased airflow nonuniformity. This trend persisted throughout both the J58 and F100/F401 compressor testing.

Exit Guide Vanes or Last Stage Stators - A circumferentially nonuniform airflow pattern is likely to exist immediately downstream of EGV's or stator vanes because of wake effects and the velocity profiles generated by turning in the vanes. These effects are localized due to the close spacing and thinness of the vanes and may be expected to dissipate a short distance downstream of the vanes. In this program, the compressor discharge total pressure probes were randomly spaced relative to the stator vanes or EGV's, so that the probes might be influenced randomly by the local airflow profiles coming off the stator vanes or EGV's. The data from both compressors studied in this program were sorted out in terms of probe orientation relative to the stator vanes and EGV's and analyzed for local effects but none could be found. The local stator vane and EGV effects appear to have fully dissipated at the instrumentation planes so the measured nonuniformities are truly present.

Downstream Struts - The diffuser case struts located downstream of the compressor could conceivably cause circumferential airflow variation by blockage effects. The rigs used in this program were all built with engine-type diffuser cases with actual-size struts. The number of struts in all the rigs was eight but no eight-cycle airflow variations were consistently observed. Only one test of the J58 compressor displayed an eight-cycle pattern, so downstream strut effects are not considered significant in the compressors studied in this program.

Inlet Distortion - Inlet total pressure distortion of the degree imposed in the J58 compressor testing was found to have little effect on discharge airflow nonuniformity. The total pressure distortion imposed simulated that distortion encountered in actual flight operation. In the F100/F401 compressor testing, classical 180-deg patterns of both total pressure and temperature distortions were imposed. This distortion carried through the compressor, producing a pattern of 180-deg nonuniformity with one high and one low airflow area at the compressor discharge. The basic airflow nonuniformity pattern generated by the compressor without inlet distortion was still present with the distortion; the 180-deg pattern was simply imposed over it. The effects of inlet distortion appear related to the compressor design and to the type of distortion imposed.

Build-to-Build Variations in Hardware - Unknown build-to-build variations in compressors built to the same design produced large variations in discharge airflow nonuniformity; these variations were as large as the changes produced by the modifications tested during the program. This phenomenon is mentioned to point out the subtleness of the causes of compressor discharge airflow nonuniformity.

Data Accuracy - Very accurate measurement systems are required in the study of compressor discharge airflow distribution because small variations in total or static pressure represent large variations in airflow. Most compressors operate with a discharge Mach number of about 0.30. The velocity head at this Mach number is 6% of total pressure; therefore, a 1% low reading from a total pressure probe would indicate an area about 9% low in airflow (assuming a uniform static pressure). A 1% high reading from a total pressure probe indicates an area about 7% high in airflow. Variations of ±1% in pressure readings from compressors are usually regarded as negligible, but they represent significant variations in local airflow if the data system is accurate. In this

program, pressure measurement uncertainties were within ±0.2%. Error analysis predicts an uncertainty of ±2.9% on local airflow and ±2.5% on average airflow at each rake location. These errors are small compared to the magnitude of airflow nonuniformity encountered.

SUMMARY OF RESULTS

Both the J58 compressor and the F100/F401 high compressor show compressor discharge airflow nonuniformities not previously realized. The J58 compressor shows the greatest airflow deviation in terms of average circumferential deviation and local airflow ratio. The F100/F401 high compressor is considerably better. However, it is more nonuniform than desirable from the standpoint of providing uniform turbine inlet temperature distribution.

The J58 compressor test cases indicated that no less than a ±10% average circumferential airflow deviation with a local airflow ratio 30% above average is typical of the nonuniformity to be expected from this compressor. The worst case showed that the circumferential airflow deviation was +20% to -33% at SLTO. Four distinct areas of high flow were found. Although several variables were examined, no significant improvements could be discerned. In fact, the build-to-build variations in the rig were larger than those produced by the variations in compressor geometry. Comparison of probe readings at various locations from the exit guide vane trailing edges showed no discernable pattern of EGV influence. These measurements are therefore believed to be unaffected by local stator or EGV airflow patterns.

The F100/F401 high compressor baseline test case is typically a ±7% average circumferential airflow deviation compressor. The local airflow ratio maximum is typically 20% above average. The high airflow regions are on the compressor discharge inner wall with only a few high spots as far away as the 50% span. The typical average circumferential airflow deviation difference for the baseline case is 16%. When aerodynamic distortion is added, this increases by 3-4%. When thermal distortion only is added, this increases by 6-7% for $\Delta T = 22°K$ (40°F) and 18-19% for $\Delta T = 55°K$ (100°F). The combined effect of aerodynamic and thermal distortion seems to be additive, so that the difference becomes 10% for $\Delta T = 22°K$ (40°F) and 22% for $\Delta T = 55°K$ (100°F) when both distortions are considered. Comparison of probe readings at various circumferential spacings from the EGV's reinforce the conclusion that the EGV's do not affect the compressor discharge airflow uniformity measurements as taken in this program.

The results of this program indicate that large airflow nonuniformities exist at the discharge of advanced turbine engine compressors. The only variable that could be defined during these tests as having a marked effect on airflow uniformity was interstage seal leakage. If not attenuated, these airflow nonuniformities could cause significant local increases in turbine inlet temperature. Any contribution to these locally high temperatures from combustor mixing inadequacies could be additive. Efforts should be initiated to improve flow uniformity in the compressor and to design diffuser-combustor systems that attenuate inlet airflow nonuniformity.

LIST OF SYMBOLS

A	Area	m^2, cm^2, (ft^2, $in.^2$)
B/M	Bill-of-Material	
cw	Clockwise	
ccw	Counterclockwise	
Deviation	Airflow deviation	%
g	Local gravitational acceleration, 9.807 m/sec^2 (32.174 ft/sec^2)	
ID	Inner Diameter	cm (in.)
IDENT	Rig-Build-Run number	
M	Mach number	
m	Number of total pressure rake locations	
m1	Number of total temperature rake locations	
n	Number of static pressure tap locations	
OD	Outer diameter	cm (in.)
P	Pressure	N/cm^2 (psia)
Q	Dynamic pressure	N/cm^2 (psia)
R	Radius	cm (in.)
$\mathcal{R}$	Gas constant for air, 0.287 J/mol °K (53.3 ft lb_f/lb_m °R)	
T	Temperature	°K (°R)
TDC	Top dead center	
W	Airflow	kg/s (lb_m/sec)
W/A	Airflow per unit area	g/s/cm^2 (lb_m/sec/in.^{2})
WA/WAA	Local airflow/overall average airflow	
γ	Specific heat ratio	
θ	Circumferential location	rad (deg)
π	3.1416	

Subscripts

avg or ave	Average
avg, ov	Overall average
ID	Inner diameter
i	Circumferential location
j	Radial location, or associated with a radial location
k	Inner or outer diameter location
L	Indicator, = 1 for J58, = 2 for F100/F401 case
Local	Value at probe head
max	Maximum value
OD	Outer diameter
S	Static
s	Static or plane of statics
T	Total
t	Total or plane of totals

Superscript

' (Prime)	Input static average

Table I. Test Conditions and Variables for Compressors Surveyed

Test Condition	Approximate Corrected Speed, %	Variable	Build-Test Number J58	Build-Test Number F100/F401	Distortion
SLTO	100	Baseline or Bill-of-Material	10-531		
			204-37		
			206-182		
	98			204-8031	
				205-4353	
				205-4233	A
				205-4453	A-T
				205-5313	A-T
				205-4653	T
				205-4753	T
	100	Modified Seals	11-185		
			12-114		
		Modified Shrouds Indexed Stators	202-8		
			203-14		
Cruise (Supersonic)	70	Baseline or Bill-of-Material	10-552		B
			10-569		A-B
			206-136		A-B
		Modified Seals	11-171		A-B
			12-453		A
Cruise (Subsonic)	95	Baseline or Bill-of-Material		204-8023	
				205-4363	
				205-4263	A
				205-4464	A-T
				205-4523	A-T
				205-6613	T
Combat	90	Baseline or Bill-of-Material		204-8014	
				205-4313	
				205-4213	A
				205-4414	A-T
				205-4513	A-T
				205-4614	T

Note: Numbers correspond to test point designations.

A - Aerodynamic Distortion
T - Thermal Distortion
B - Bleeds

Table II. J58 Compressor Rig Discharge Instrumentation Combinations

Rig	Build	Run	No. P_t	No. T_t	No. P_s (OD)	No. P_s (ID)
30204	10	531	26	11	8	0
30204	10	552	26	11	8	0
30204	10	569	26	11	8	0
30204	11	185	26	10	6	0
30204	11	171	26	10	6	0
30204	12	114	33	11	6	0
30204	12	453	33	11	6	0
30239	202	8	33	10	3	0
30239	203	14	32	10	3	0
30239	204	37	32	10	3	0
30239	206	136	27	12	8	8
30239	206	182	27	12	8	8

Table III. J58 Compressor Rig Data Comparison

Rig	30204							30239				
Build	10			11		12		202	203	204	206	
Run	531	552	569	185	171	114	453	8	14	37	136	182
Conditions:												
SLTO	X									X-e		X-f
Cruise		X										
Cruise-D			X								X-f	
SLTO, Mod. Seals				X-a		X-b		X-c				
Cruise-D, Mod. Seals					X-a		X-b					
SLTO, Indexed Stators									X-d			
Variables at Compressor Discharge:												
Overall Average:												
Total pressure, N/cm^2	26.22	26.17	25.61	24.26	25.72	26.0	22.43	25.62	25.79	26.11	26.39	24.27
(psi)	38.03	37.96	37.15	35.18	37.298	37.71	32.53	37.16	37.408	37.873	38.27	35.206
Total temperature, °K	638.83	456.21	452.61	628.81	453.90	628.56	609.66	624.77	625.63	614.24	458.45	620.68
(°R)	1149.89	821.17	814.69	1131.84	817.02	1131.32	1097.3	1124.5	1126.05	1105.54	825.2	1117.13
Static pressure, N/cm^2	24.88	24.01	23.53	22.73	22.24	24.06	20.74	24.15	23.99	24.34	24.26	22.73
(psi)	36.08	34.82	34.13	32.97	33.710	34.89	30.08	35.03	34.788	35.304	35.19	32.96
Dynamic pressure, N/cm^2	1.346	2.161	2.08	1.524	2.464	1.95	1.69	1.47	1.81	1.77	2.119	1.55
(psi)	1.952	3.134	3.016	2.211	3.574	2.832	2.45	2.129	2.62	2.57	3.073	2.247
Airflow/unit area, $kg/sec\ cm^2$	0.0472	0.0707	0.069	0.0497	0.0747	0.058	0.0507	0.050	0.055	0.056	0.0704	0.050
($lb_m/sec\ in^2$)	0.264	0.396	0.386	0.278	0.418	0.323	0.284	0.28	0.31	0.312	0.394	0.281
Mach number	0.278	0.354	0.351	0.309	0.384	0.339	0.339	0.294	0.327	0.321	0.349	0.311
Circumferential Airflow Deviation:												
Maximum, %	+19.55	+15.35	+17.45	+8.91	+10.51	+10.38	+11.70	+15.65	+8.6	+6.92	+13.72	+8.04
Minimum, %	-32.90	-11.28	-13.40	-10.47	-7.88	-8.87	-15.57	-13.30	-10.65	-12.80	-9.68	-11.16
Difference, %	52	27	31	19	18	19	27	29	19	20	23	19
No. of High Deviation Areas*	4	4	4	3	4	2	2	6	4	5	5	5
No. of Low Deviation Areas*	4	6	5	3	4	4	2	5	3	2	4	4
Local Airflow Ratio:												
Maximum	1.523	1.294	1.310	1.393	1.335	1.351	1.334	1.436	1.362	1.341	1.277	1.379
Minimum	0.116	0.351	0.138	0.244	0.447	0.295	0.306	0.223	0.268	0.114	0.355	0.047
No. of High Flow Areas	4	4	4	4	4	4	4	5	7	6	4	7

Notes: X - Bill-of-Material (B/M) Compressor Configuration
D - Simulated Engine Inlet Distortion
a - Tight Interstage Seals in Stages 1 through 4, Abradable-Type
b - Tight Interstage Seals Throughout, Felt Metal Type
c - Feltmetal Tip Shrouds Stages 5 through 9
d - First Four Stages Rotated Counterclockwise 36 deg Looking Upstream, Otherwise B/M
e - Same as d Except First Four Stages Returned to Normal Position, B/M
f - Foreign Object Damaged Blades in Stages 2 through 9, otherwise B/M
* - More Than 5% Variation From Average

-25-

Fold out

1

F.O.

2

Table IV. F100/F401 High Compressor Rig Data Comparison

Rig	34017			34017														
Build	204			205														
Run No.	80-3-1 (8031)	80-2-3 (8023)	80-1-4 (8014)	343-5-3 (4353)	343-6-3 (4363)	343-1-3 (4313)	342-3-3 (4233)	342-6-3 (4263)	342-1-3 (4213)	344-5-3 (4453)	344-6-4 (4464)	344-1-4 (4414)	345-3-13 (5313)	345-2-3 (4523)	345-1-3 (4513)	346-5-3 (4653)	346-6-13 (6613)	346-1-4 (4614)	347-5-3 (4753)
Conditions:																			
SLTO	X			X			X+a			X+b			X+c			X+d			X+e
Cruise, Subsonic		X			X			X+a			X+b			X+c			X+d		
Combat			X			X			X+a			X+b			X+c			X+d	
Variables at Compressor Discharge:																			
Overall Average:																			
Total Pressure, N/cm^2	62.47	57.13	49.33	62.01	56.73	50.64	61.77	55.5	49.23	60.98	54.86	48.66	60.81	54.53	49.07	62.59	58.68	50.36	63.87
(psi)	90.6	82.86	71.54	89.94	82.28	73.44	89.59	80.49	71.40	88.44	79.56	70.57	88.19	79.08	71.17	90.77	85.1	73.03	92.63
Total Temperature, °K	550.0	528.6	505.2	551.5	530.8	507.1	559.0	526.5	513.6	571.6	544.7	521.5	608.55	585.4	562.2	618.1	577.4	529.5	559.7
(°R)	990.0	951.4	909.2	992.7	955.3	912.7	1006.2	947.6	924.4	1028.9	980.4	938.9	1095.3	1053.6	1011.8	1112.5	1039.2	953.1	1007.4
Static Pressure, N/cm^2	59.43	54.03	46.61	59.05	53.92	47.93	59.01	52.64	46.56	58.04	52.04	45.97	57.69	51.64	46.58	59.70	55.75	47.58	60.88
(psi)	86.22	78.37	67.59	85.65	78.2	69.51	85.57	76.35	67.52	84.17	75.48	66.67	83.67	74.9	67.55	86.58	80.85	69.0	88.29
Dynamic Pressure, N/cm^2	3.03	3.1	2.72	2.97	2.81	2.71	2.78	2.85	2.67	2.96	2.82	2.69	3.14	2.89	2.51	2.89	2.93	2.78	3.00
(psi)	4.39	4.5	3.95	4.31	4.081	3.93	4.026	4.14	3.873	4.292	4.09	3.902	4.55	4.19	3.64	4.191	4.25	4.03	4.35
Airflow/Unit Area, $kg/sec\ cm^2$	0.121	0.119	0.106	0.119	0.113	0.107	0.114	0.113	0.104	0.115	0.109	0.103	0.114	0.106	0.0096	0.111	0.112	0.106	0.114
($lb_m/sec\ in^2$)	0.676	0.666	0.593	0.665	0.632	0.598	0.639	0.632	0.582	0.646	0.612	0.576	0.641	0.592	0.537	0.624	0.629	0.591	0.641
Mach Number	0.269	0.285	0.287	0.267	0.272	0.283	0.259	0.277	0.285	0.269	0.277	0.288	0.278	0.282	0.276	0.263	0.274	0.288	0.265
Circumferential Airflow Deviation:																			
Maximum, %	+4.76	+5.14	+10.23	+8.45	+5.38	+7.12	+12.1	+11.13	+8.68	+13.32	+13.24	+14.29	+16.42	+19.78	+20.38	+10.74	+9.13	+13.79	+17.35
Minimum, %	-8.5	-5.6	-6.02	-10.59	-8.44	-7.39	-10.74	-6.47	-6.97	-13.92	-10.92	-10.61	-17.46	-20.55	-16.72	-12.9	-8.83	-9.40	-17.41
Difference, %	13	11	16	19	14	15	23	18	16	27	24	25	34	40	37	24	18	23	35
No. of High Deviation Areas*	0	1	2	1	2	2	4	3	3	3	3	4	3	4	3	3	3	3	2
No. of Low Deviation Areas*	2	1	1	2	2	1	2	3	2	1	1	1	2	2	2	3	3	1	1
Local Airflow Ratio:																			
Maximum	1.13	1.15	1.22	1.163	1.147	1.176	1.176	1.198	1.225	1.216	1.249	1.277	1.259	1.326	1.347	1.165	1.156	1.263	1.229
Minimum	0.647	0.656	0.611	0.58	0.575	0.616	0.601	0.574	0.614	0.599	0.538	0.623	0.563	0.48	0.525	0.564	0.573	0.611	0.510
Area of High Flow or No. of Areas	Hub	Hub	Hub	Hub	Hub	Hub	Hub	Hub	Hub	Hub	Hub	Hub	Hub	Hub	Hub	4	Hub	Hub	Hub

Notes: X - Undistorted inlet contains OD screen that simulates the fan. This is present all the time.
a - Aerodynamic Distortion, 3.14 rad (180 deg) Screen
b - Aerodynamic Distortion, 3.14 rad (180 deg) Screen Plus Thermal Distortion $\Delta T = 22°K$ (40°F)
c - Aerodynamic Distortion, 3.14 rad (180 deg) Screen Plus Thermal Distortion $\Delta T = 55°K$ (100°F)
d - Thermal Distortion $\Delta T = 22°K$ (40°F)
e - Thermal Distortion $\Delta T = 55°K$ (100°F)
* - More Than 5% Deviation From Average

Fold out

1

F.O. 2

F.O. 3

Stage	Type	No.	No. 1 Vane Location Looking Upstream
IGV	Vanes	20	TDC Foil Rotation -11 deg to +23.17 deg
1st	Blades Vanes	34 78	0.383 deg CCW
2nd	Blades Vanes	52 82	1.083 deg CW
3rd	Blades Vanes	76 114	TDC
4th	Blades Vanes	72 120	TDC
5th	Blades Vanes	54 120	TDC
6th	Blades Vanes	60 104	TDC
7th	Blades Vanes	84 104	TDC
8th	Blades Vanes	90 136	TDC
9th	Blades Vanes	102 84	TDC
EGV	Vanes	168	0.825 deg CW
	Probes		Figure 4 or 5
	Struts	8	TDC

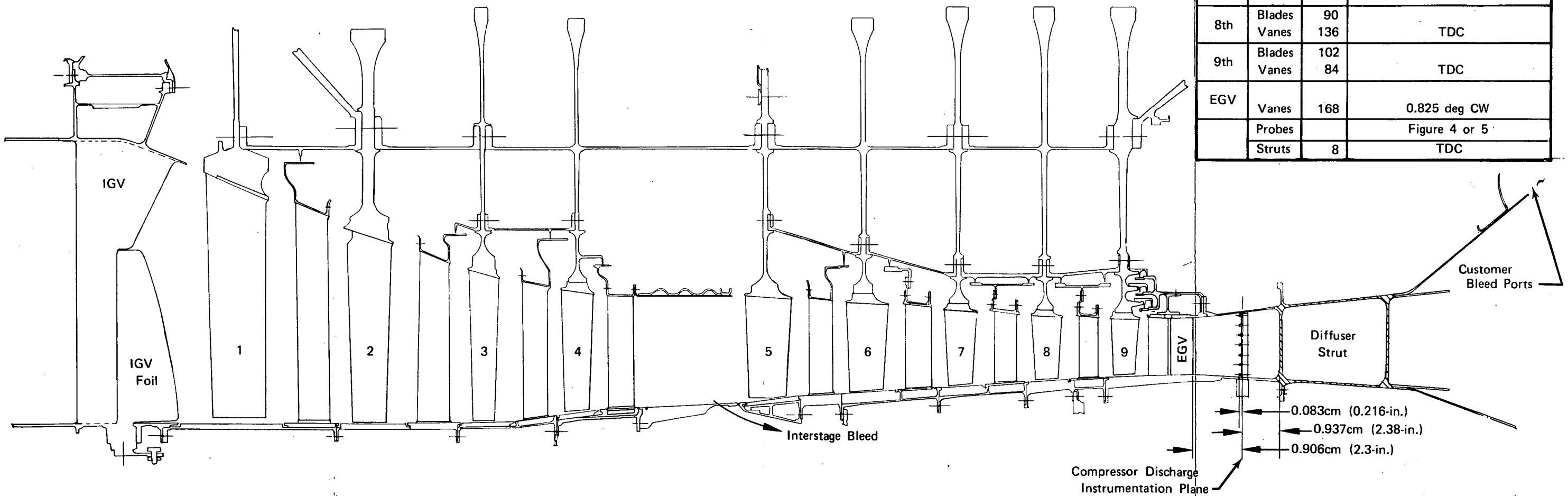

Figure 1. J58 Compressor Rig Schematic

FD 63336A

Stage	Type	No.	No. 1 Vane Location Looking Upstream
	Screen Mount Vanes	12	TDC
	Preswirl Vanes	40	TDC
	Cambered Struts	8	11 deg CCW
IGV	Vanes	90	TDC
4th	Blades Vanes	52 64	TDC
5th	Blades Vanes	70 62	TDC
6th	Blades Vanes	86 74	TDC
7th	Blades Vanes	88 82	TDC
8th	Blades Vanes	96 98	TDC
9th	Blades Vanes	94 106	TDC
10th	Blades Vanes	92 122	TDC
11th	Blades Vanes	82 132	TDC
12th	Blades Vanes	90 138	TDC
13th	Blades	94	
EGV	Vanes	96	TDC
	Comp Discharge Probes	32	Figure 9
	Diffuser Struts	8	TDC

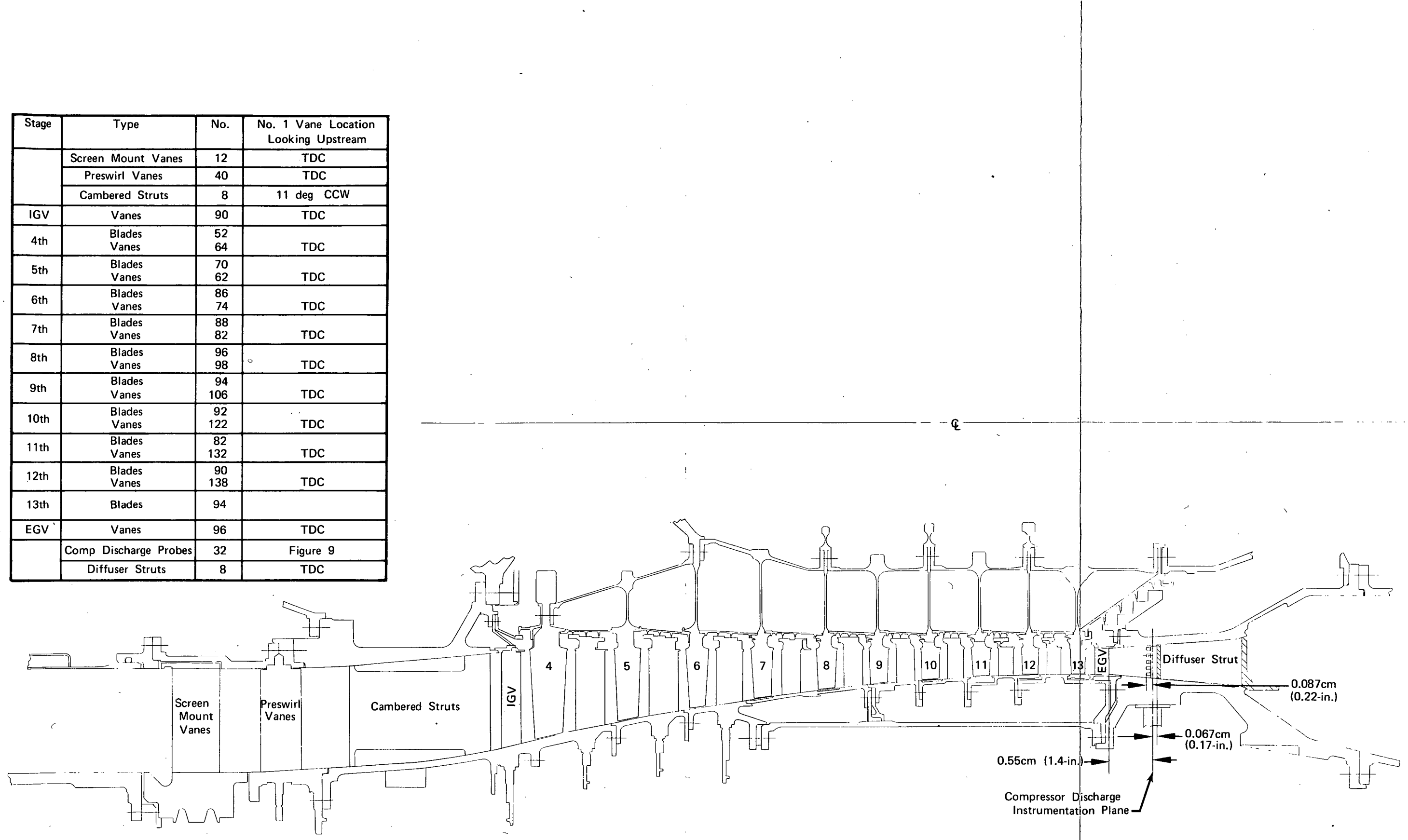

Figure 2. F100/F401 High Compressor Rig Schematic

FD 63337A

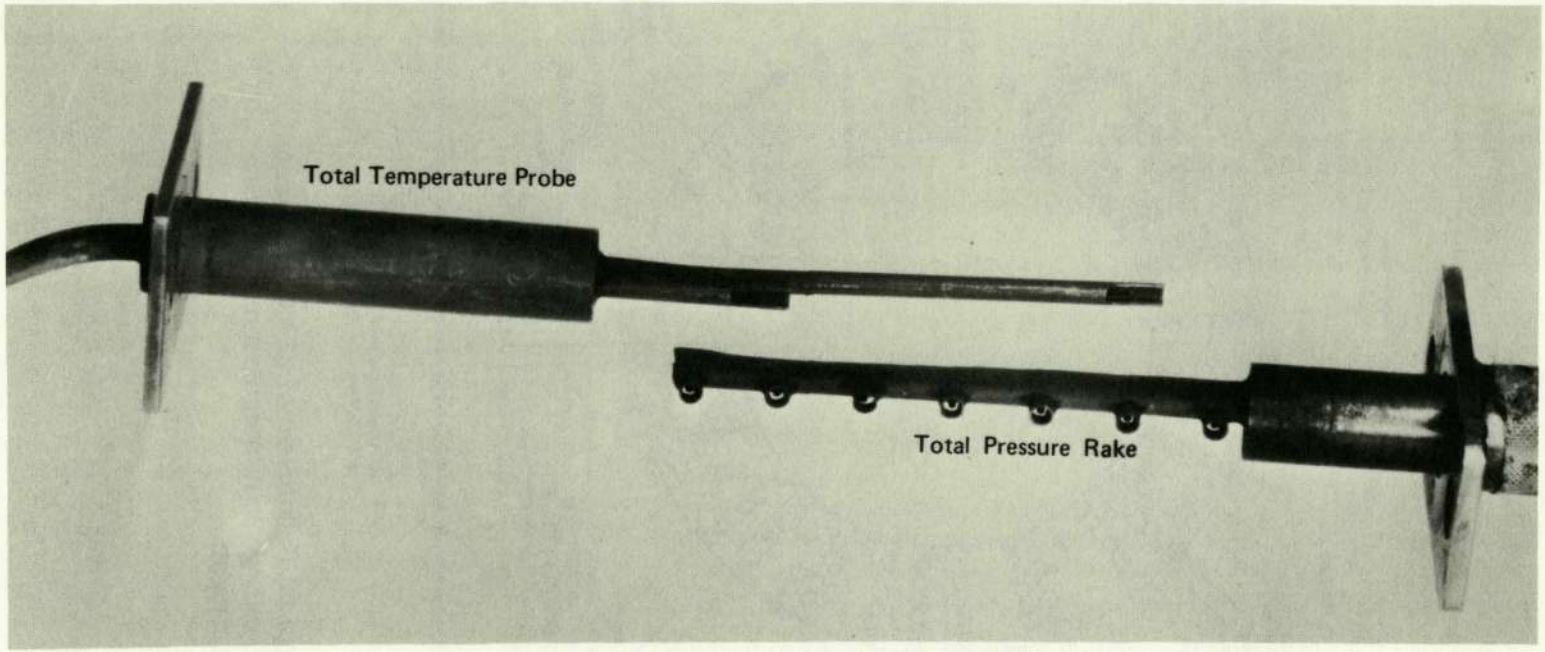

Figure 3. Typical J58 Compressor Discharge Instrumentation FE 120469 B

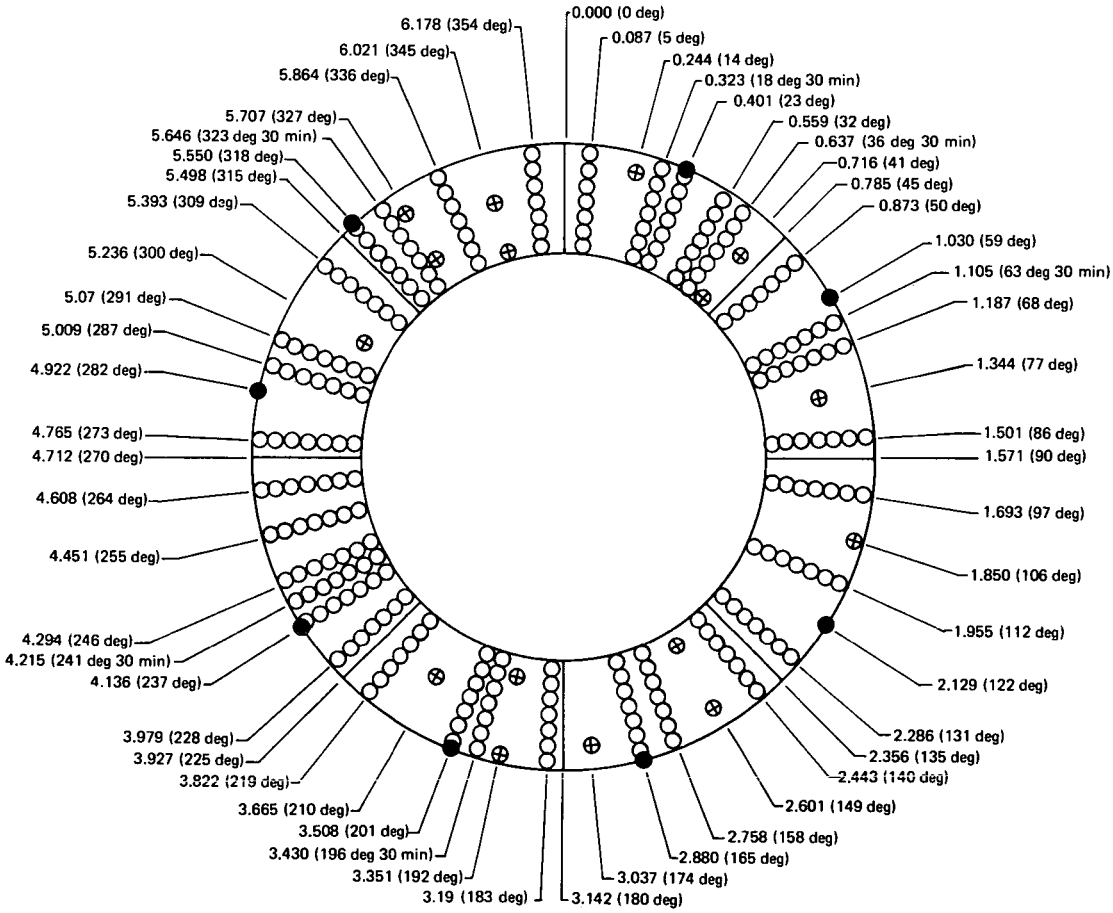

Note: All locations were not used for every build. Typical of all builds except 206. Angles are given in radians (degrees).

Key:

- ○ Total Pressure - Thirty-Three 7-Point Rakes
- ⊕ Total Temperature - Eleven Probes
- ● Static Pressure - Eight Wall Taps, OD

Figure 4. Typical Schematic of J58 Compressor Discharge Instrumentation, Looking Upstream

FD 63335

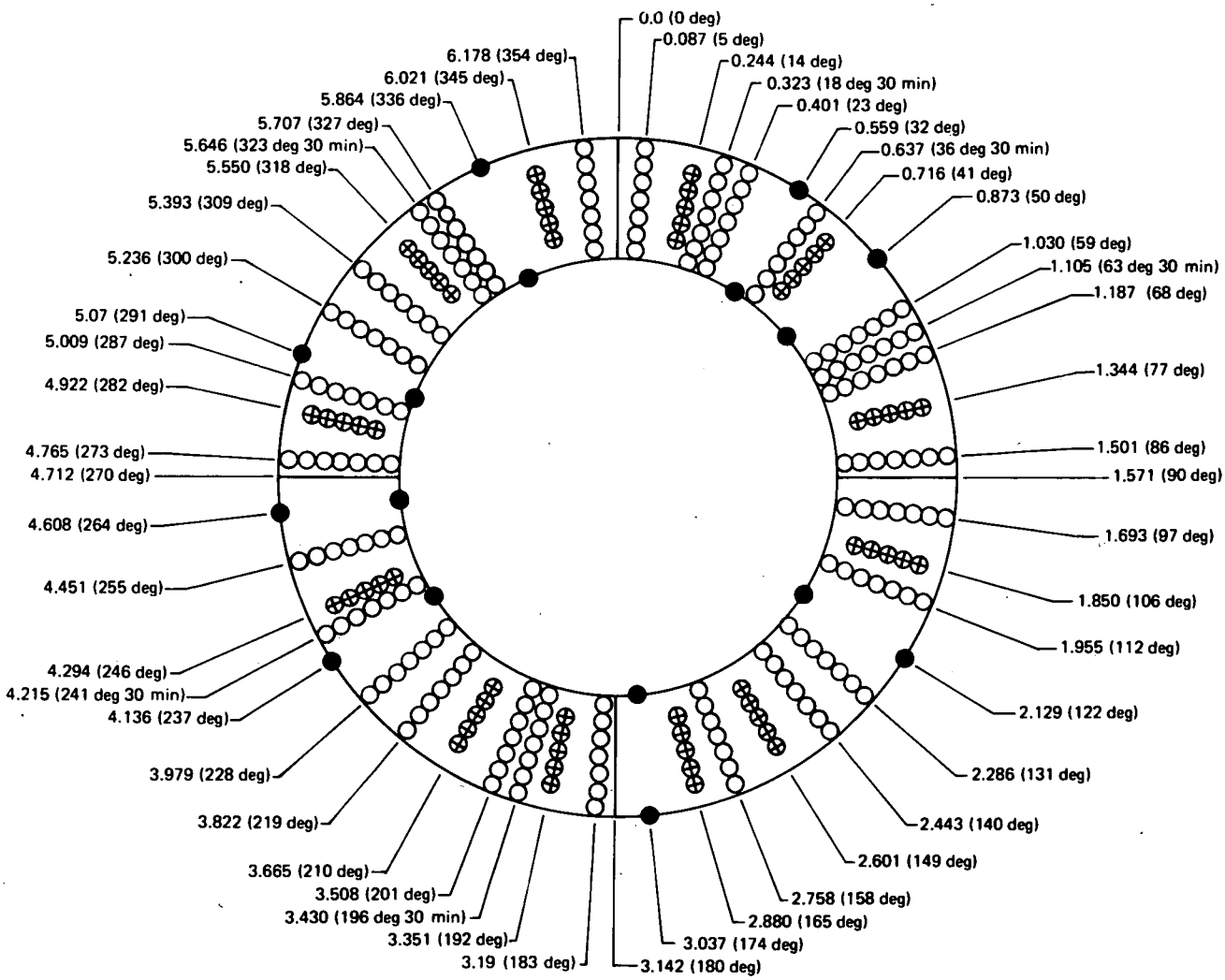

Note: Angles are given in radians (degrees).

Key:
- ○ Total Pressure - Twenty-Seven 7-Point Rakes
- ⊕ Total Temperature - Twelve 5-Point Rakes
- ● Static Pressure - Sixteen Wall Taps

Figure 5. Schematic of J58 Compressor Discharge Instrumentation, Looking Upstream; Rig 30239, Build 206, Runs 136 and 182 FD 63334

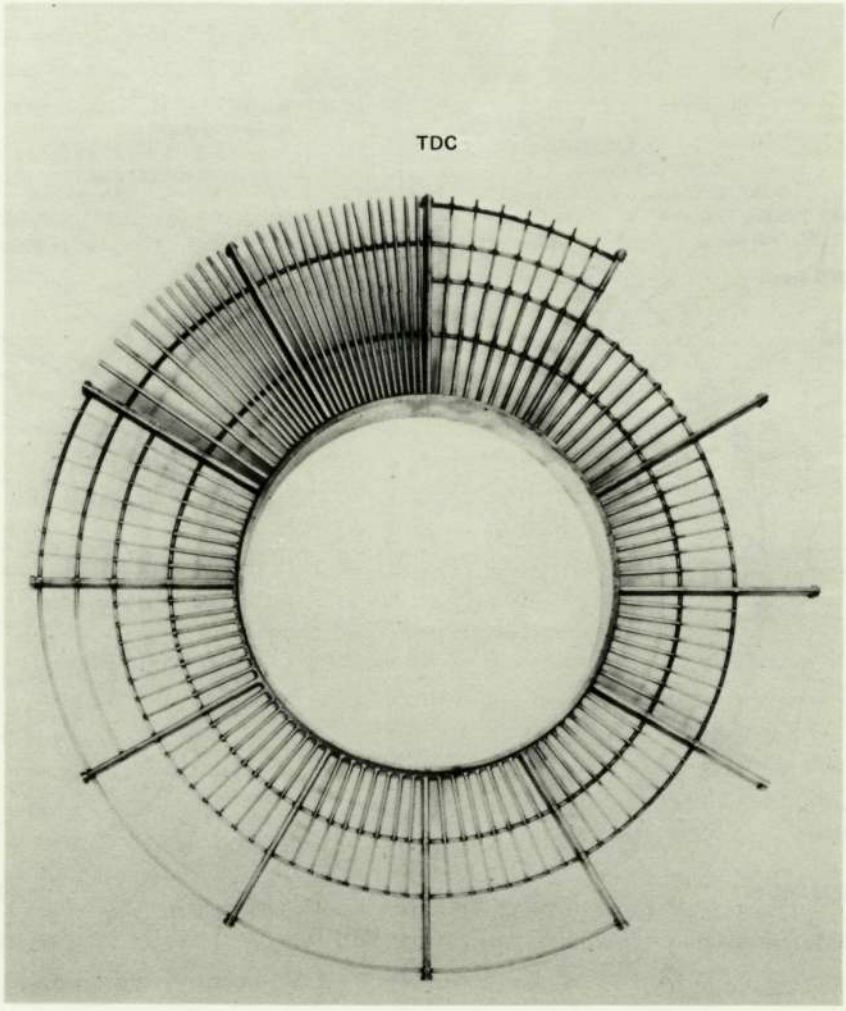

Figure 6. J58 Cruise Inlet Distortion Screen, Looking Upstream FE 104135B

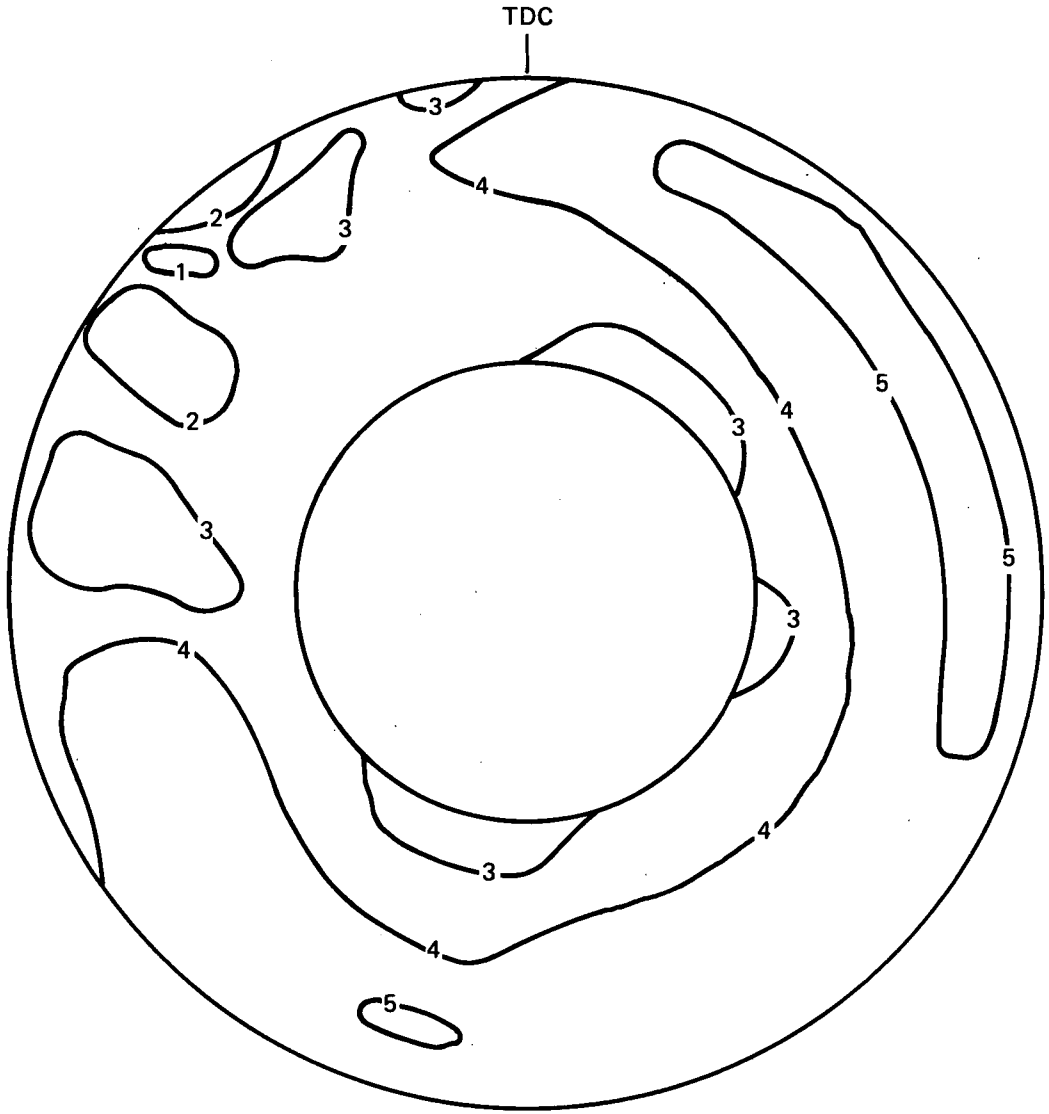

Symbol	$P_t/P_{t_{average}}$
1	0.94
2	0.96
3	0.98
4	1.00
5	1.02

Figure 7. J58 Compressor Rig Inlet Total Pressure Distribution, Looking Upstream; Cruise-Distorted Inlet, Rig 30204, Build 10, Run 569

FD 63352A

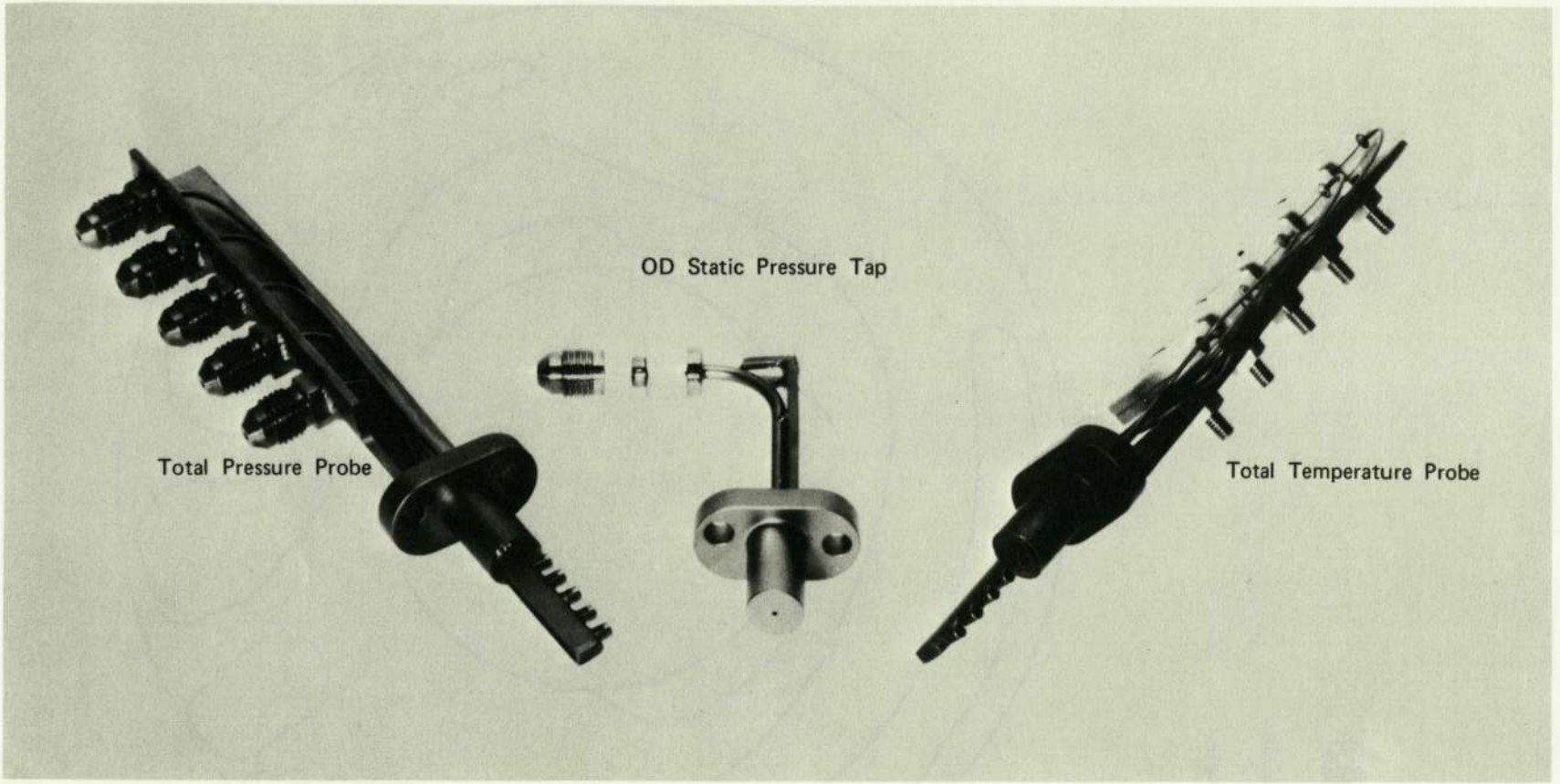

Figure 8. Typical F100/F401 High Compressor Discharge Instrumentation

FE 112884A

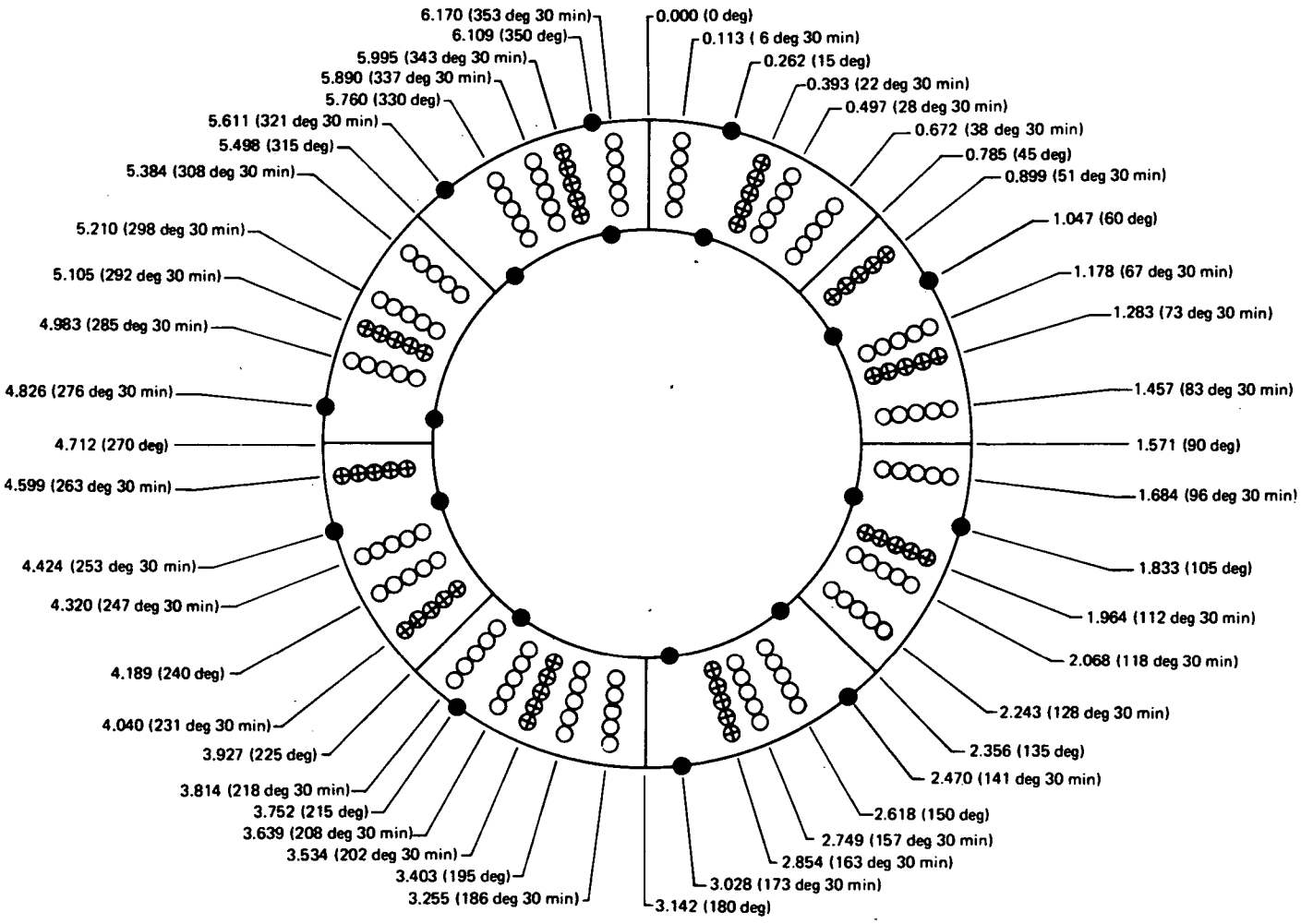

Figure 9. Schematic of F100/F401 Compressor Discharge Instrumentation, Looking Upstream

FD 63333

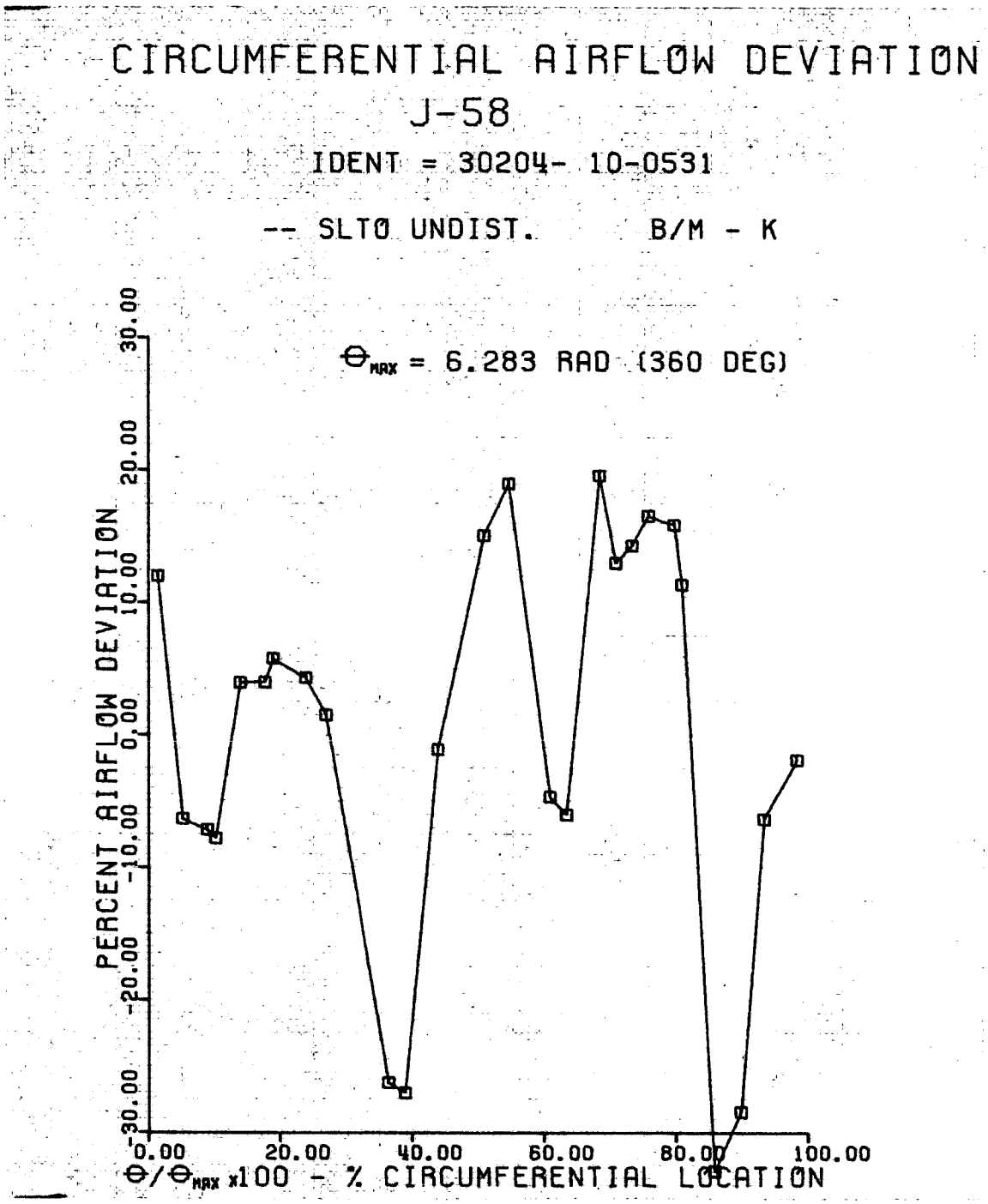

Figure 10.

DF 92056

COMPRESSOR DISCHARGE FLOW MAP

J-58 COMPRESSOR RIG - - $W_{LOCAL}/W_{AVE.\ OVERALL}$

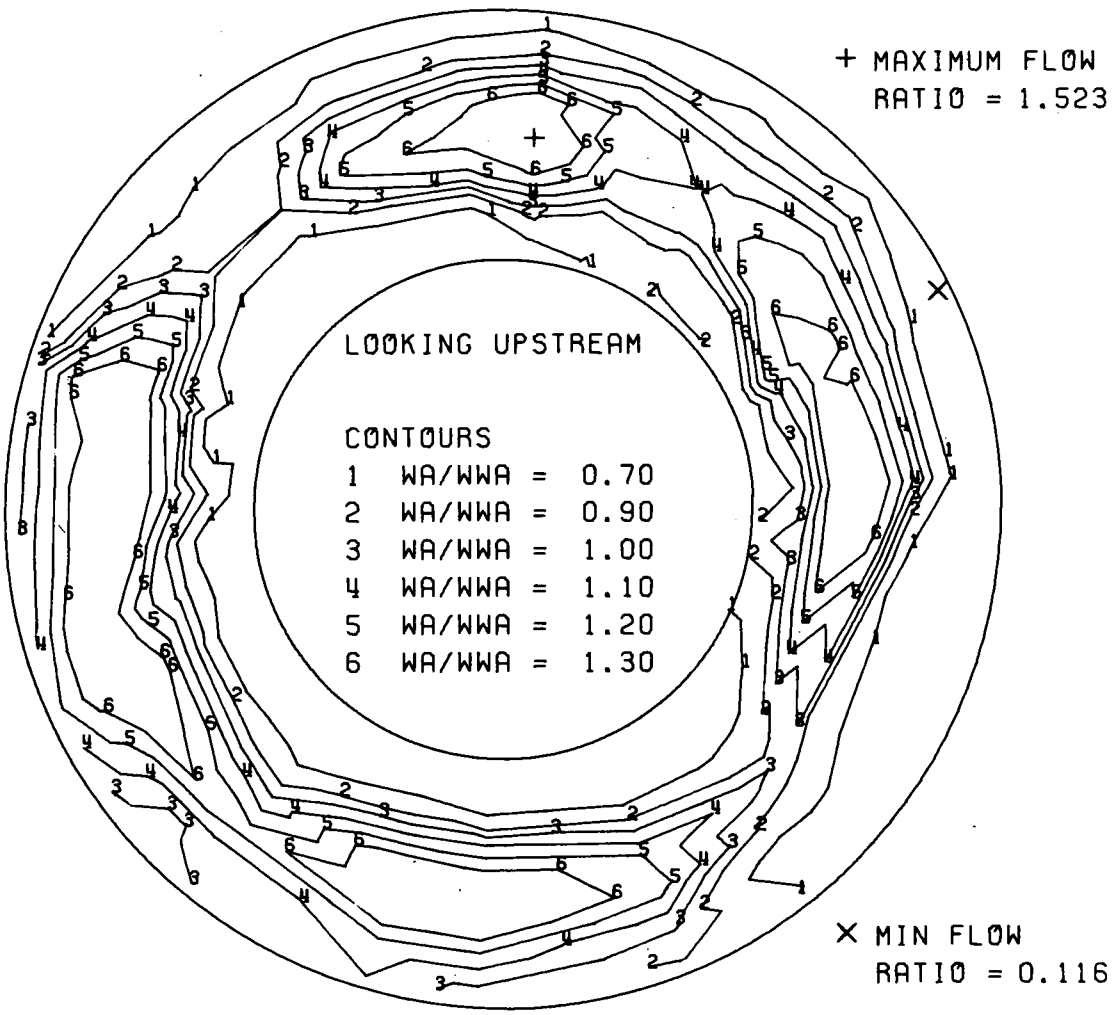

RIG NO.30204 BUILD NO.= 10 RUN NO.= 0531 CONDITION- -- SLTO UNDIST.

Figure 11.

DF 92063

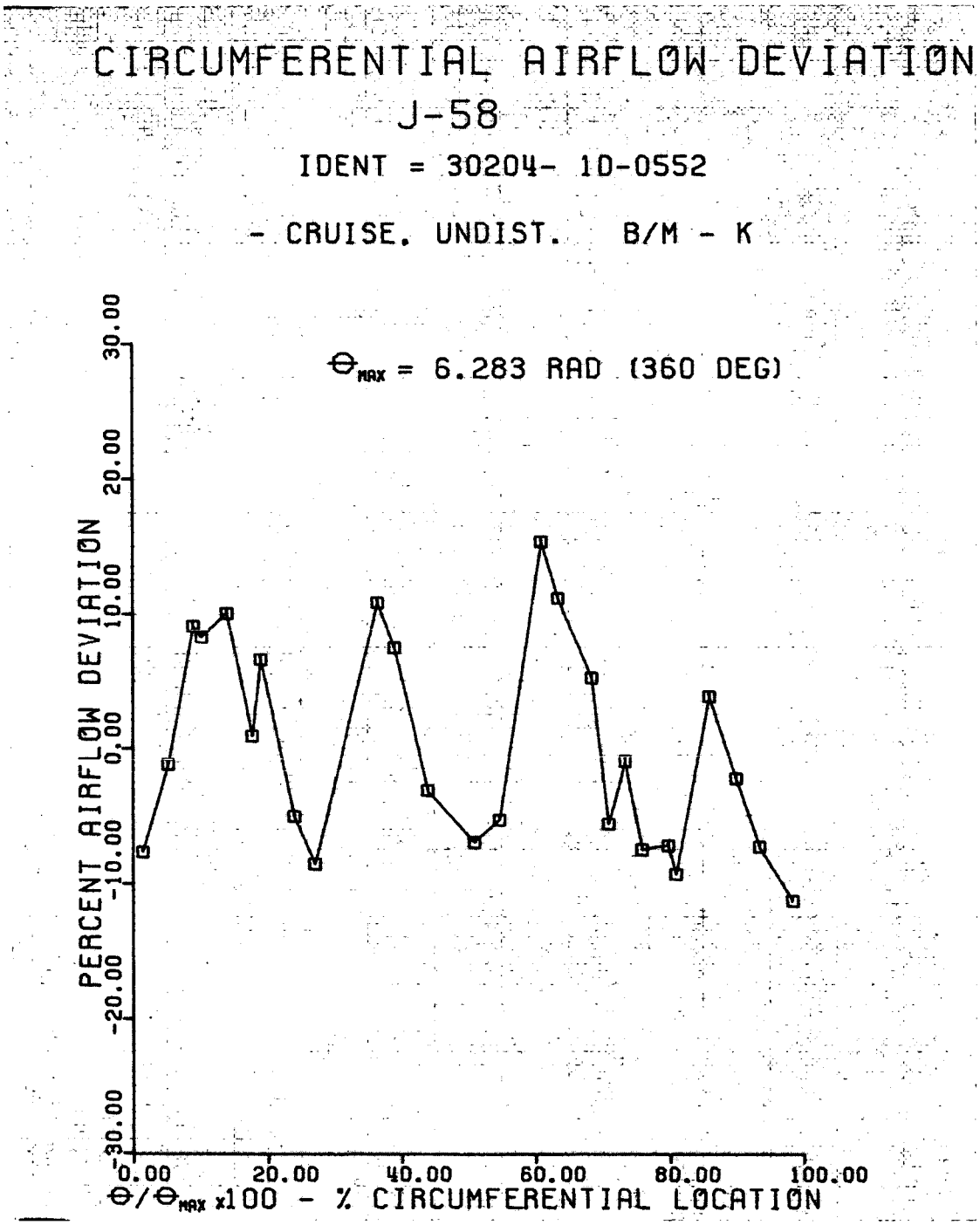

Figure 12.

DF 92057

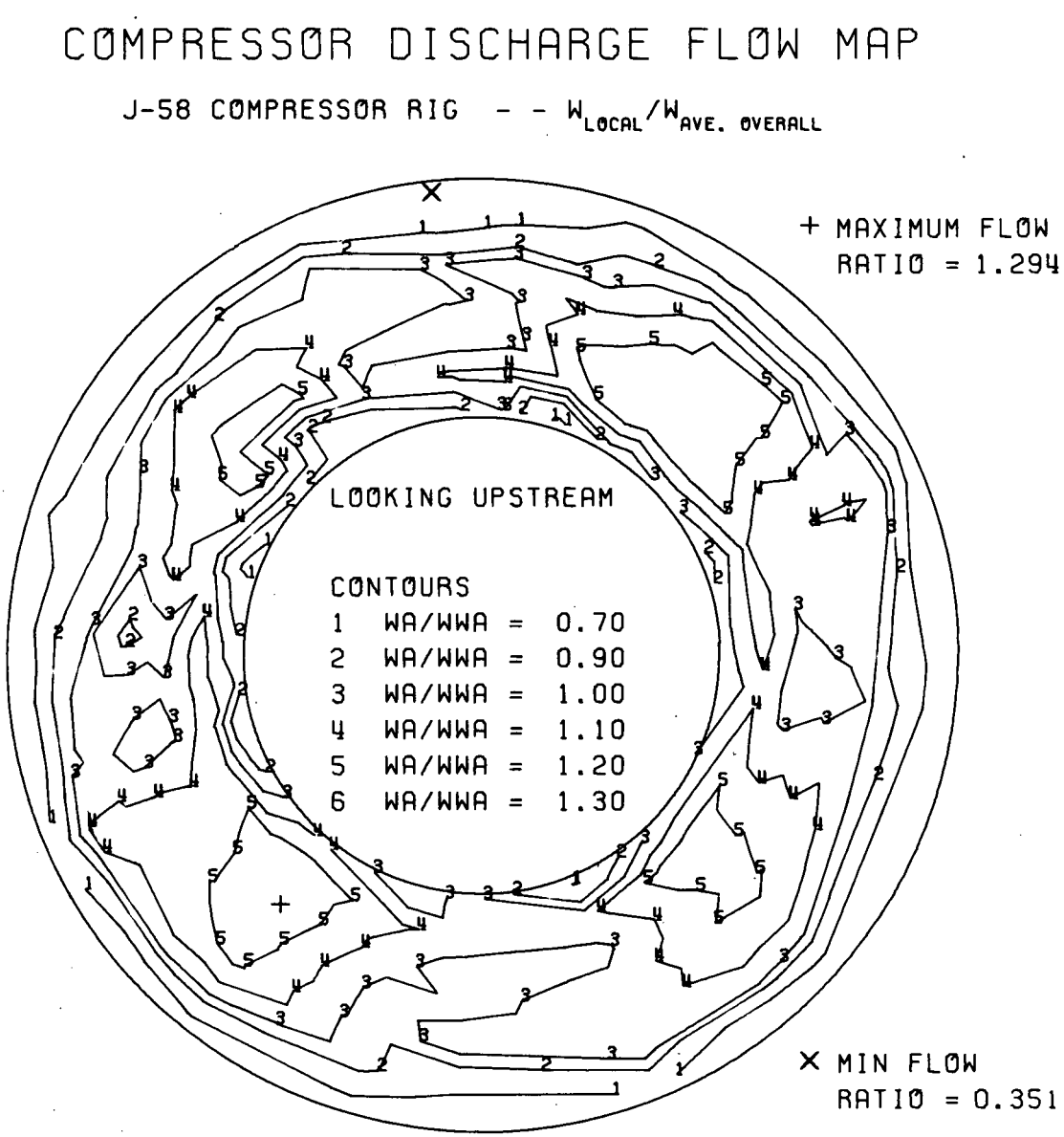

Figure 13.

DF 92070

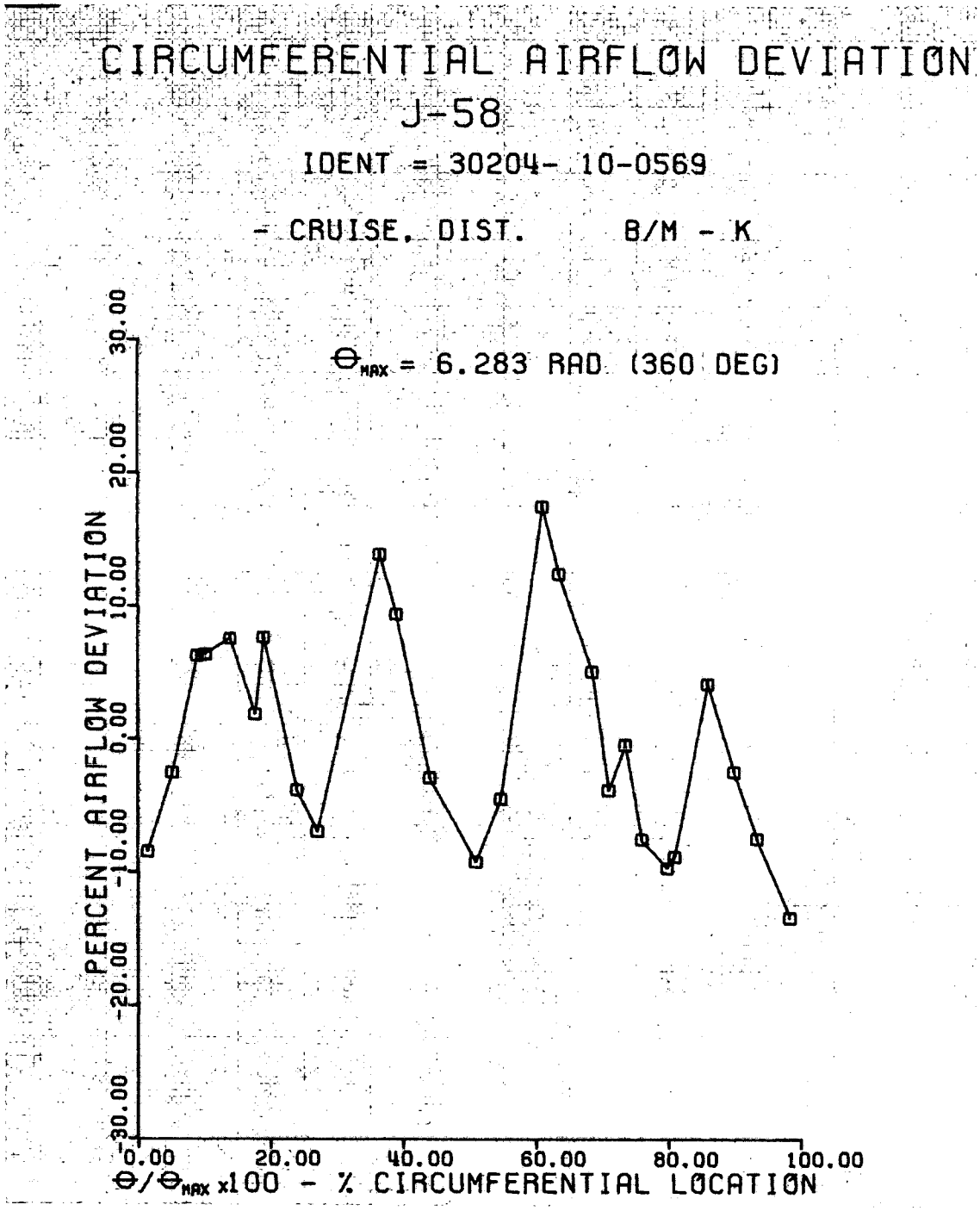

Figure 14.

DF 92058

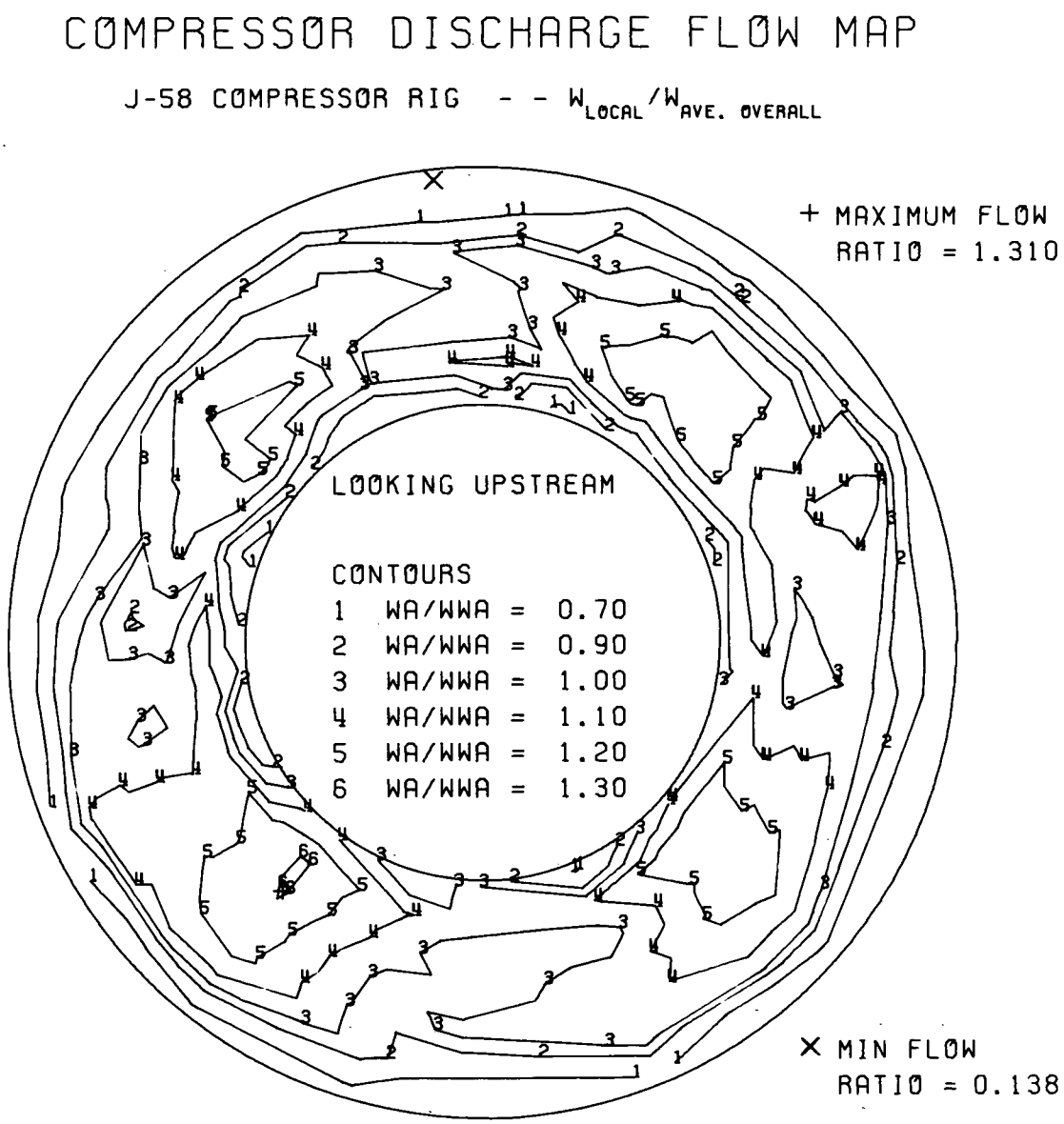

Figure 15. DF 92064

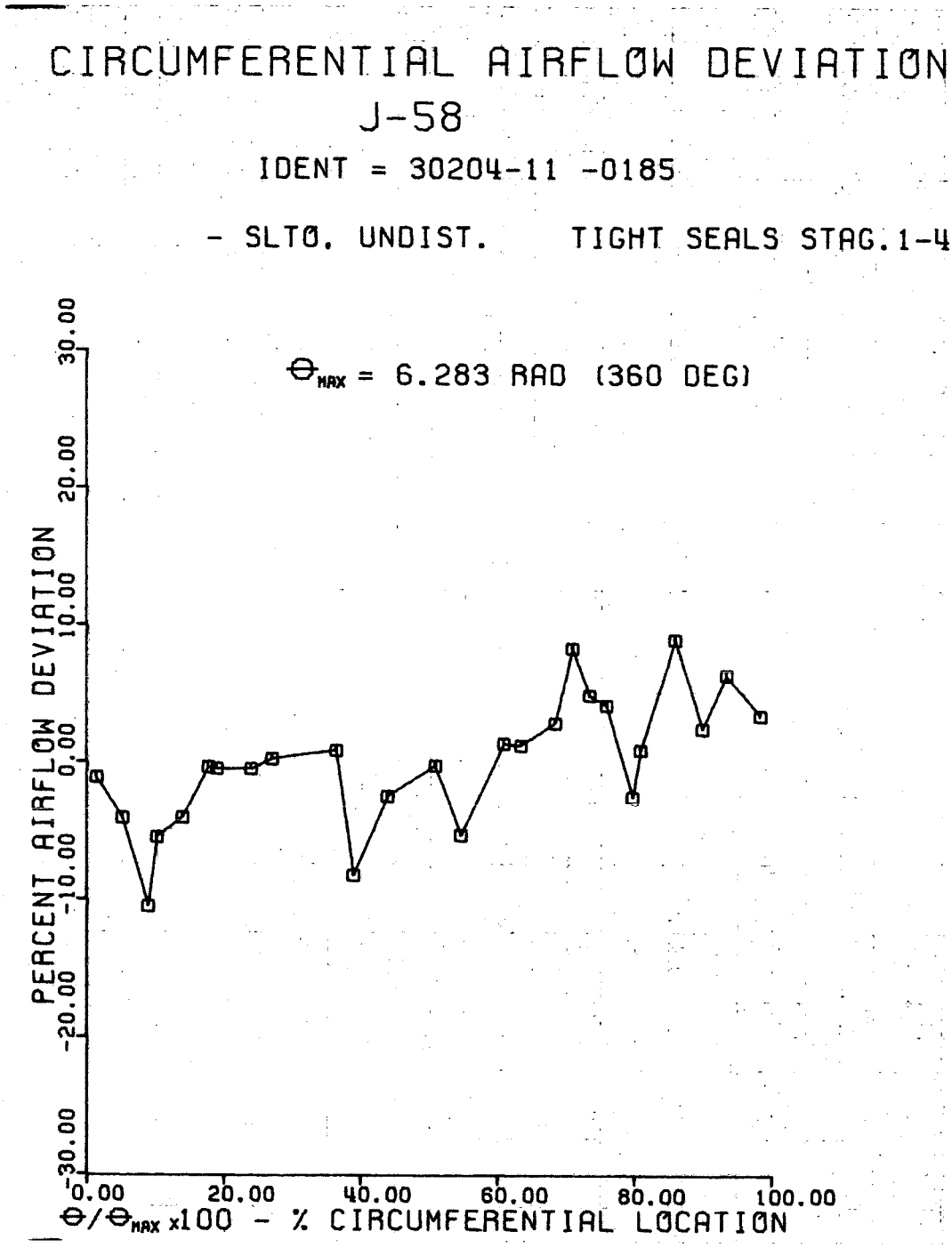

Figure 16.

DF 92055

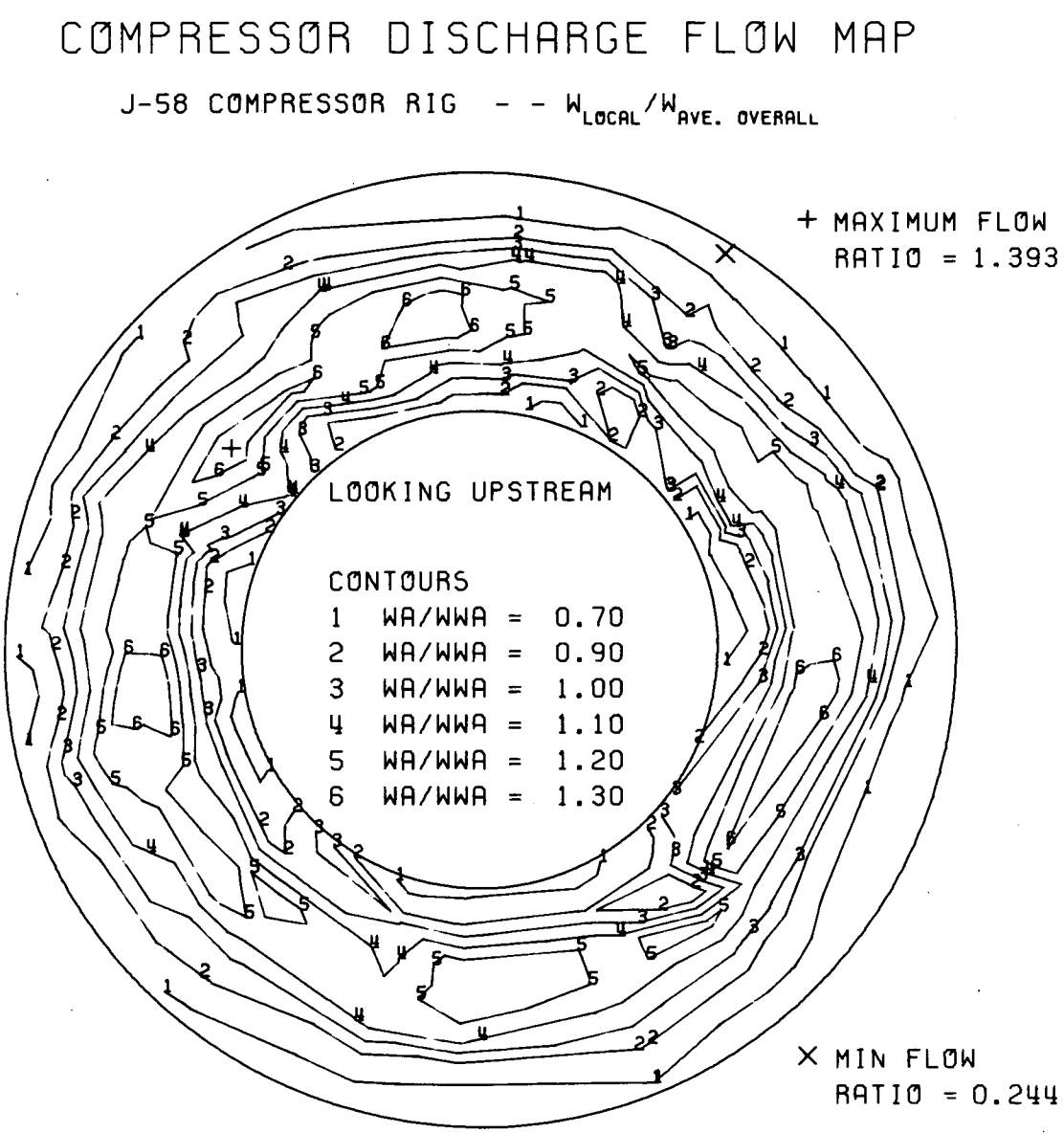

Figure 17.

DF 92062

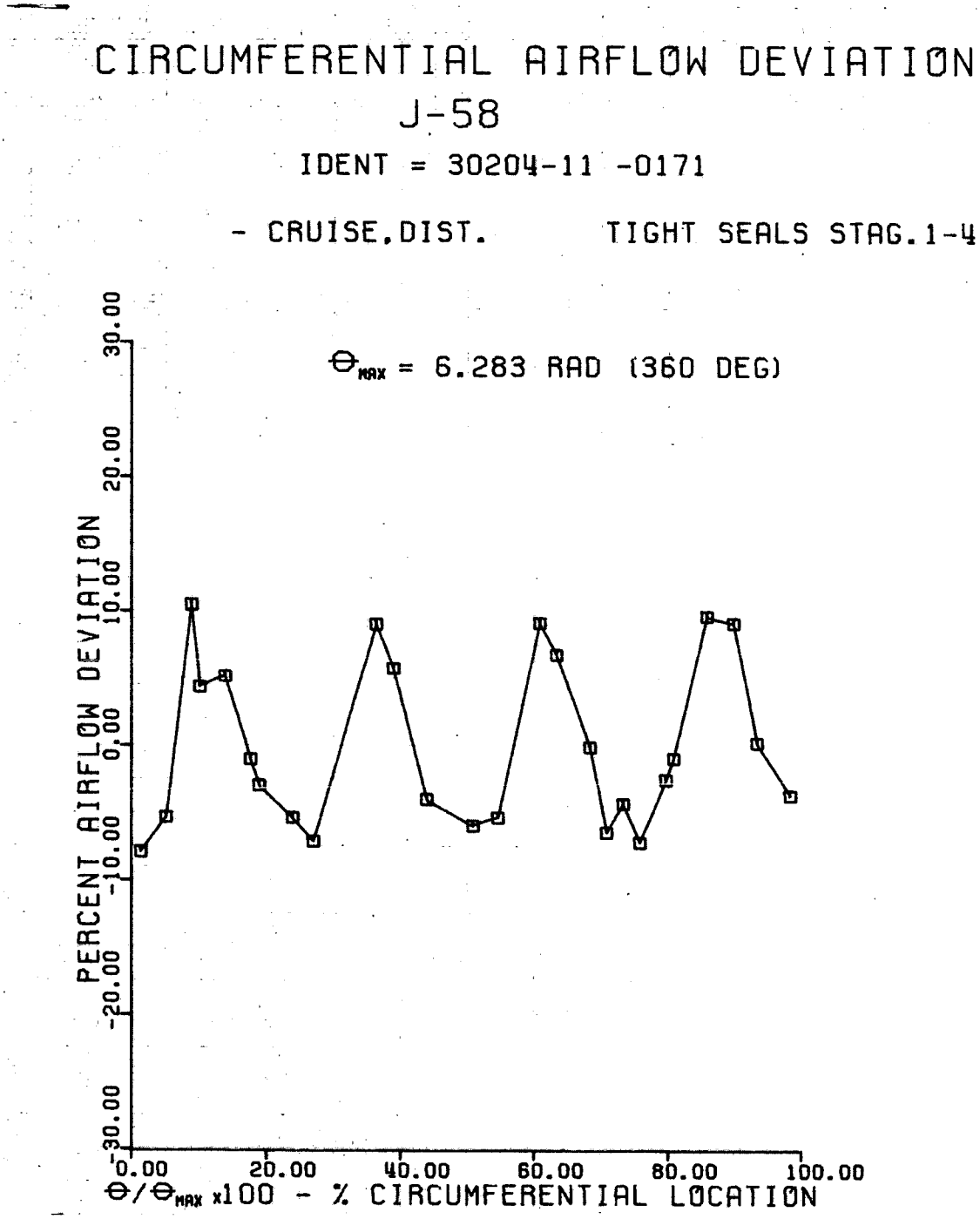

Figure 18.

DF 92054

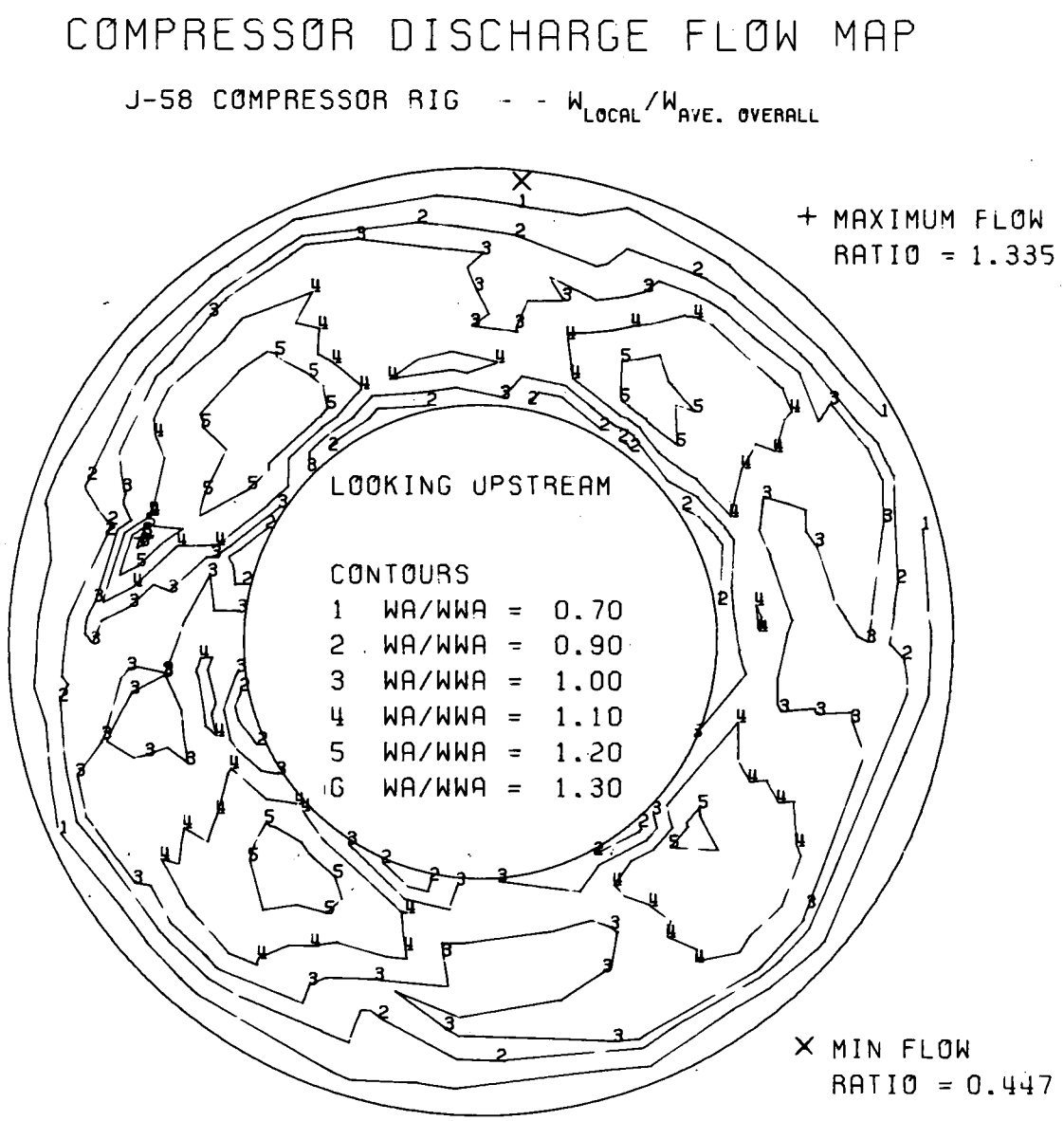

RIG NO.30204 BUILD NO.=11 RUN NO.=0171 CONDITION-- CRUISE,DIST.

Figure 19.

DF 92071

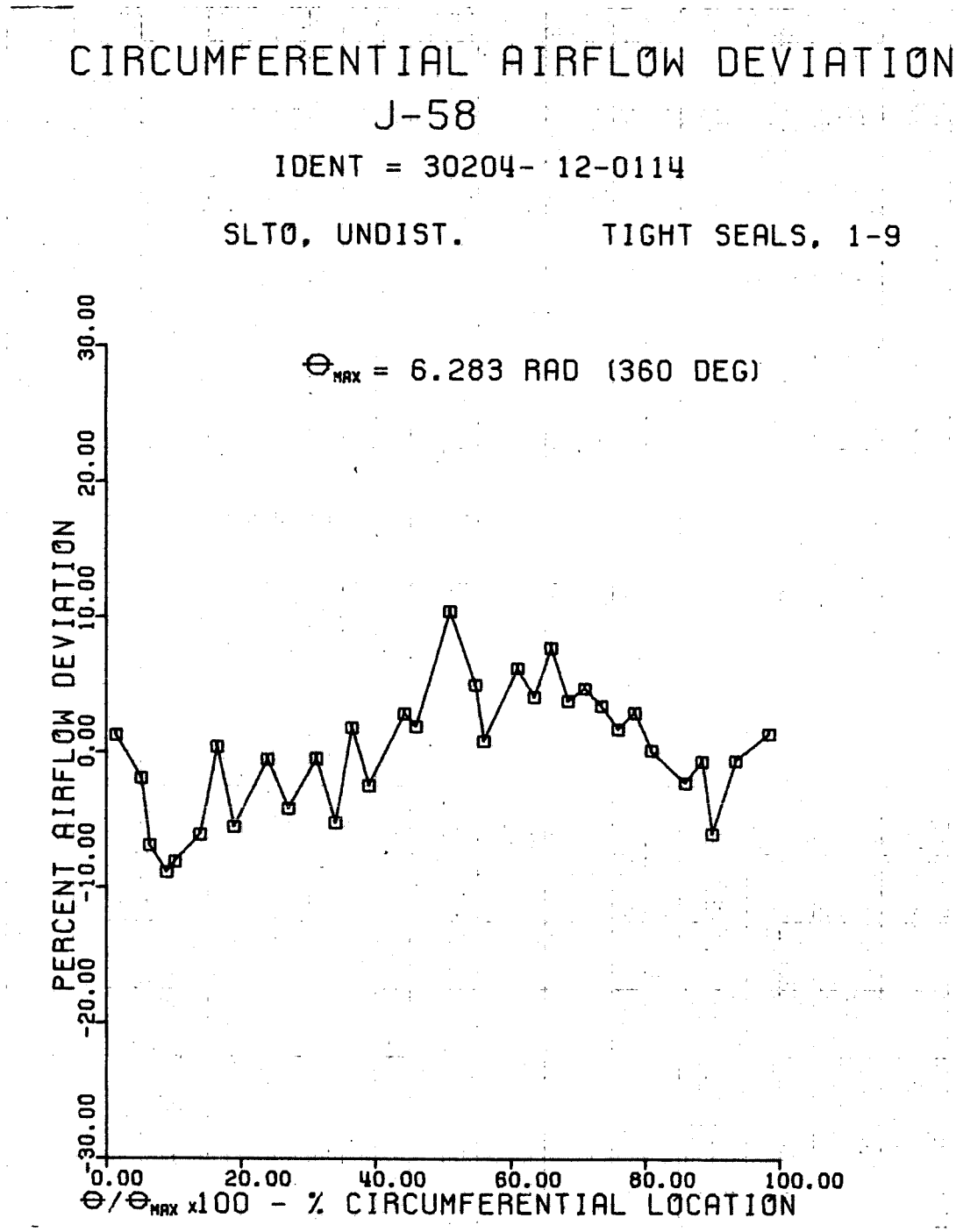

Figure 20.

DF 92053

COMPRESSOR DISCHARGE FLOW MAP

J-58 COMPRESSOR RIG - - $W_{LOCAL}/W_{AVE.\ OVERALL}$

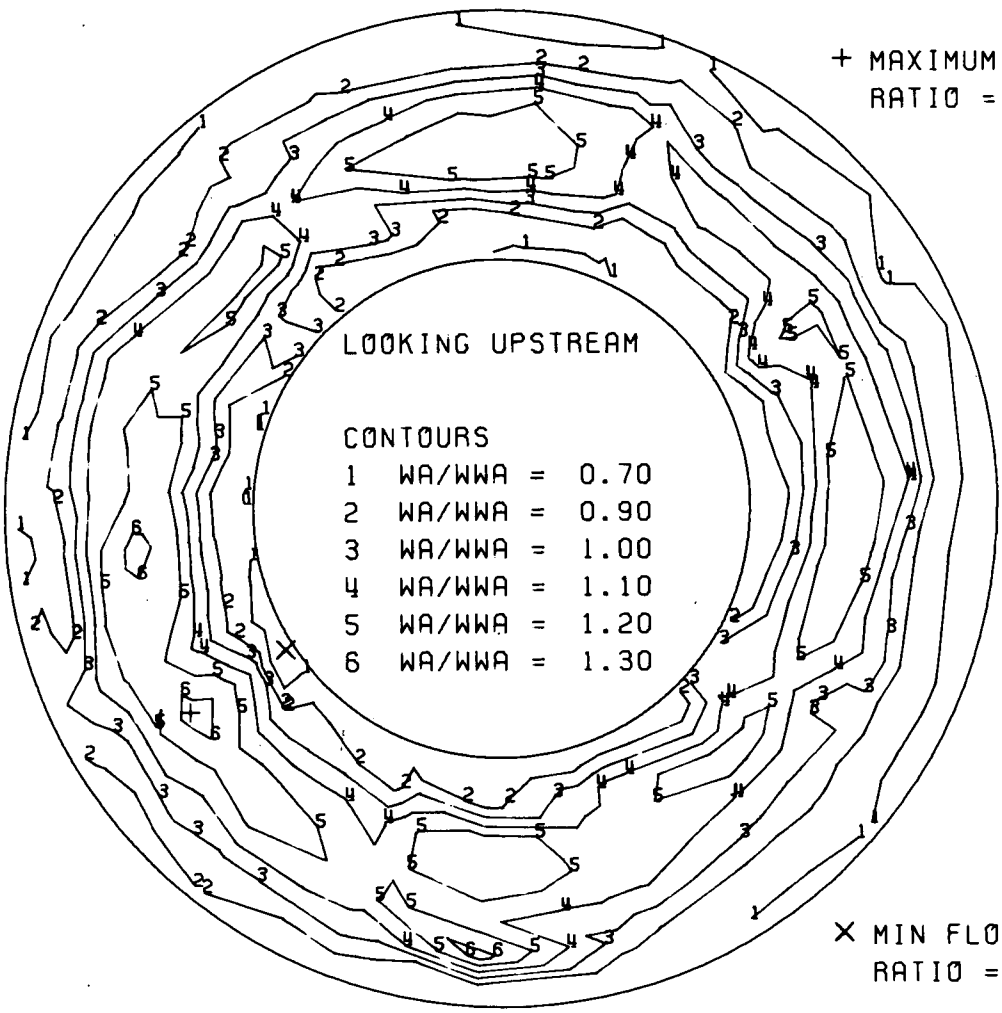

RIG NO.30204 BUILD NO.= 12 RUN NO.=0114 CONDITION- SLTO, UNDIST.

Figure 21. DF 92061

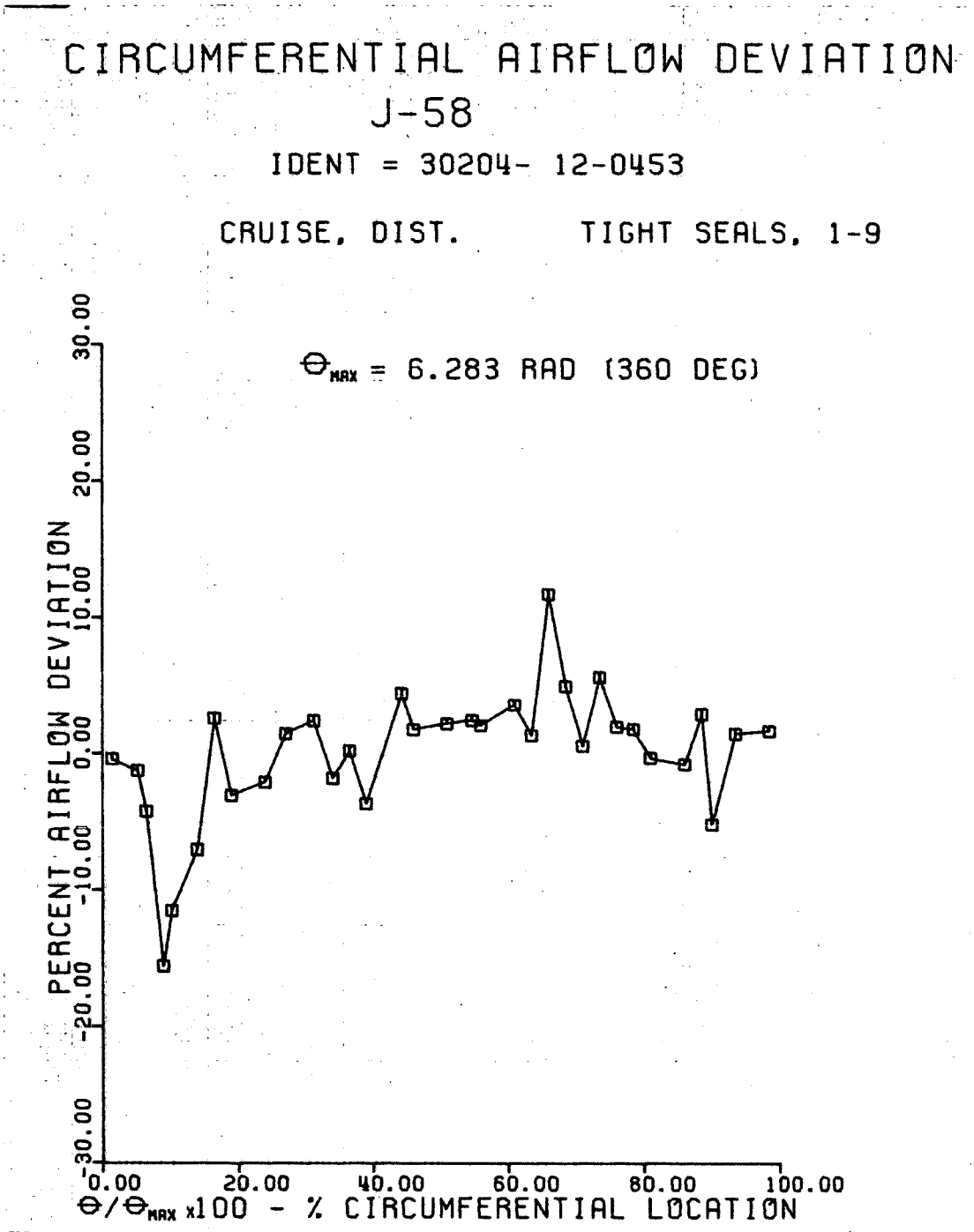

Figure 22.

DF 92050

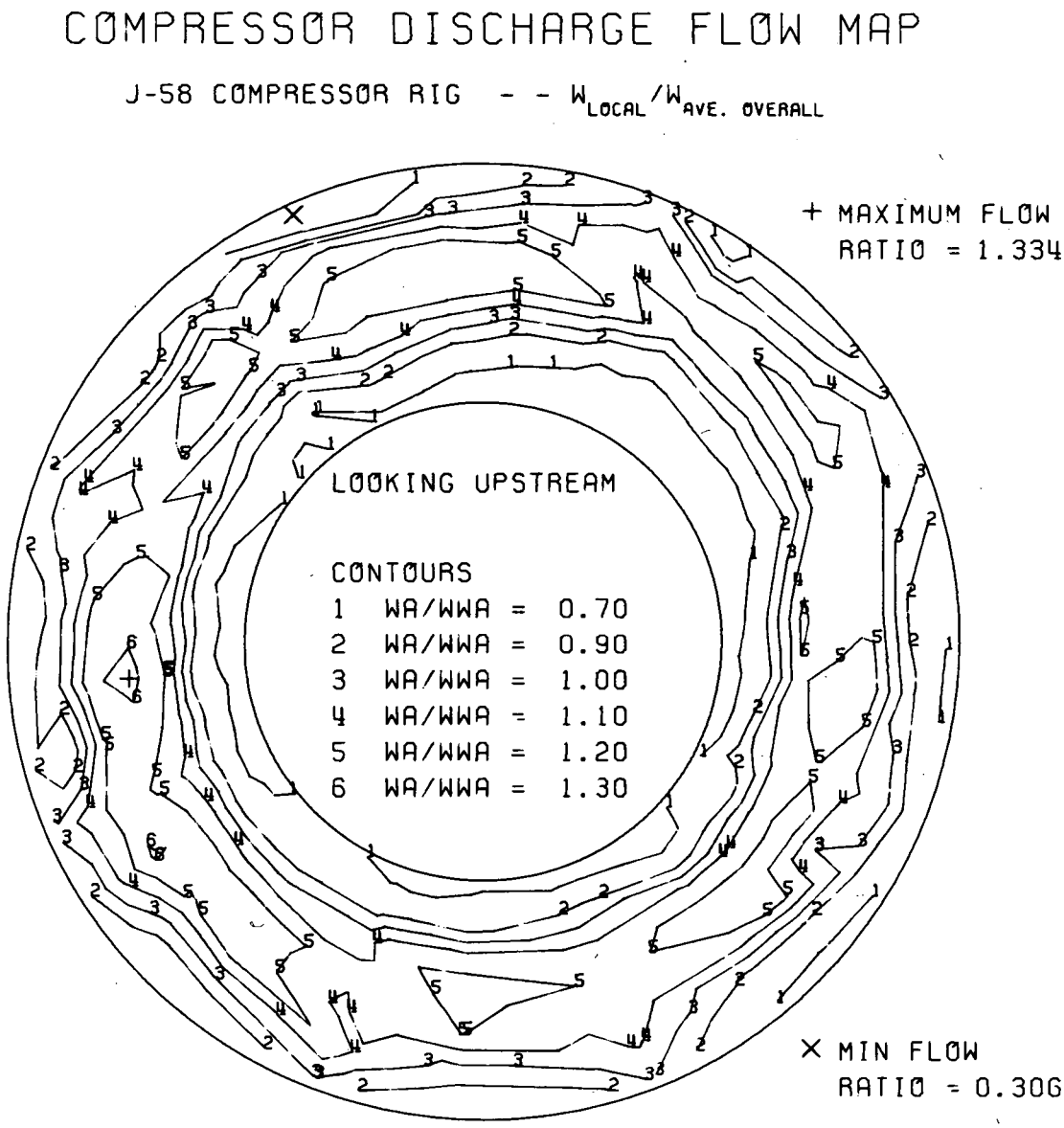

Figure 23.

DF 92069

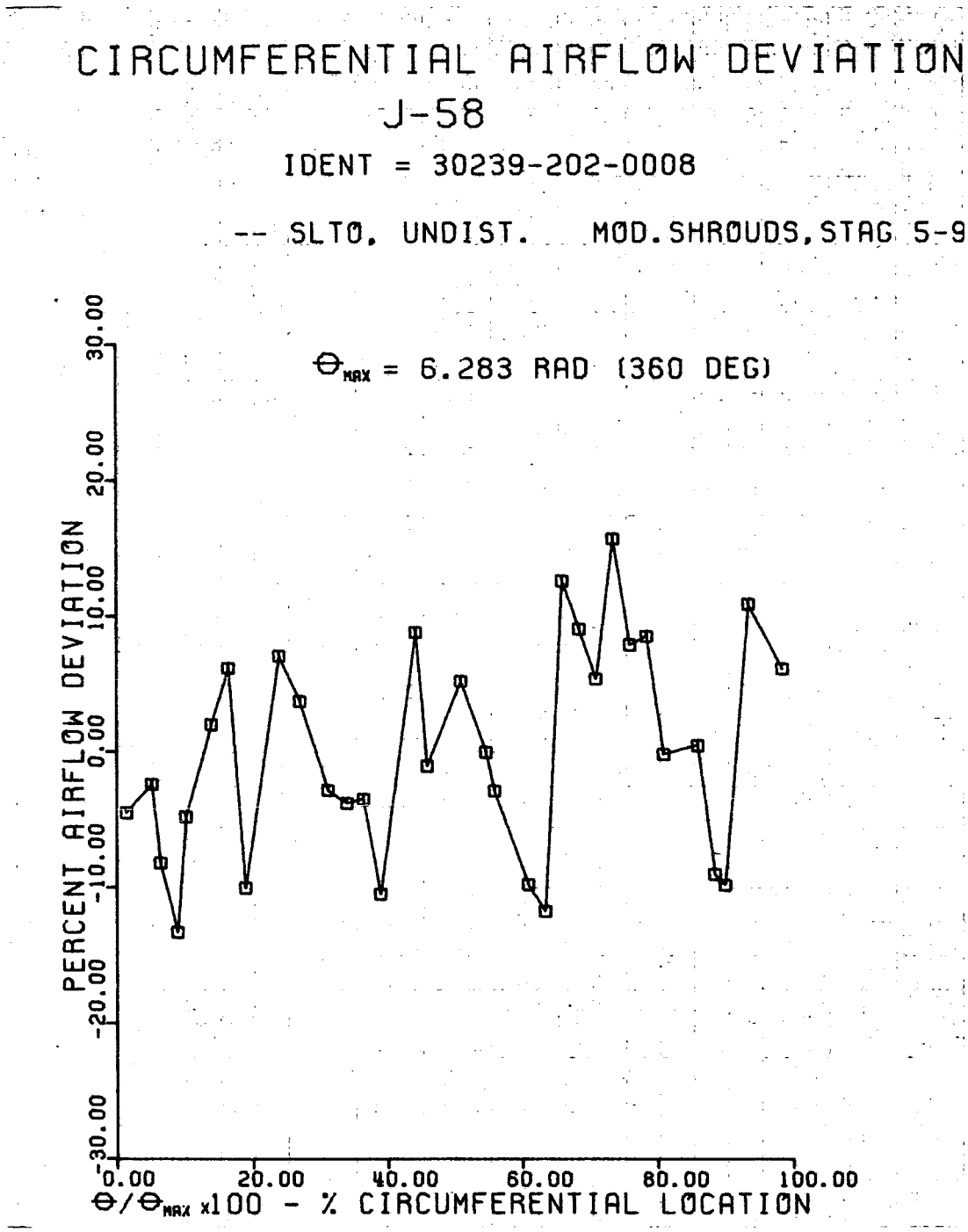

Figure 24.

DF 92052

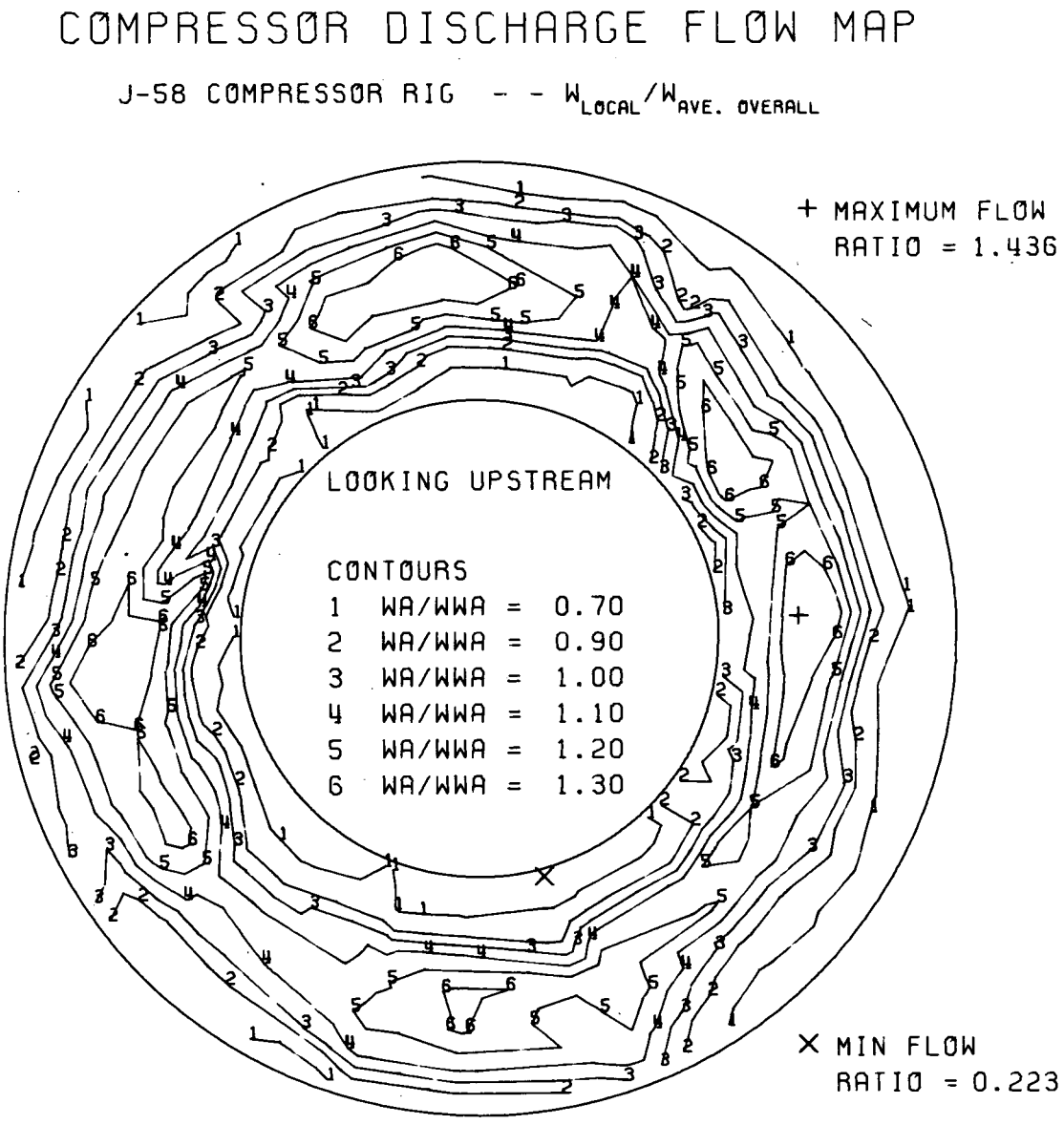

Figure 25.

DF 92065

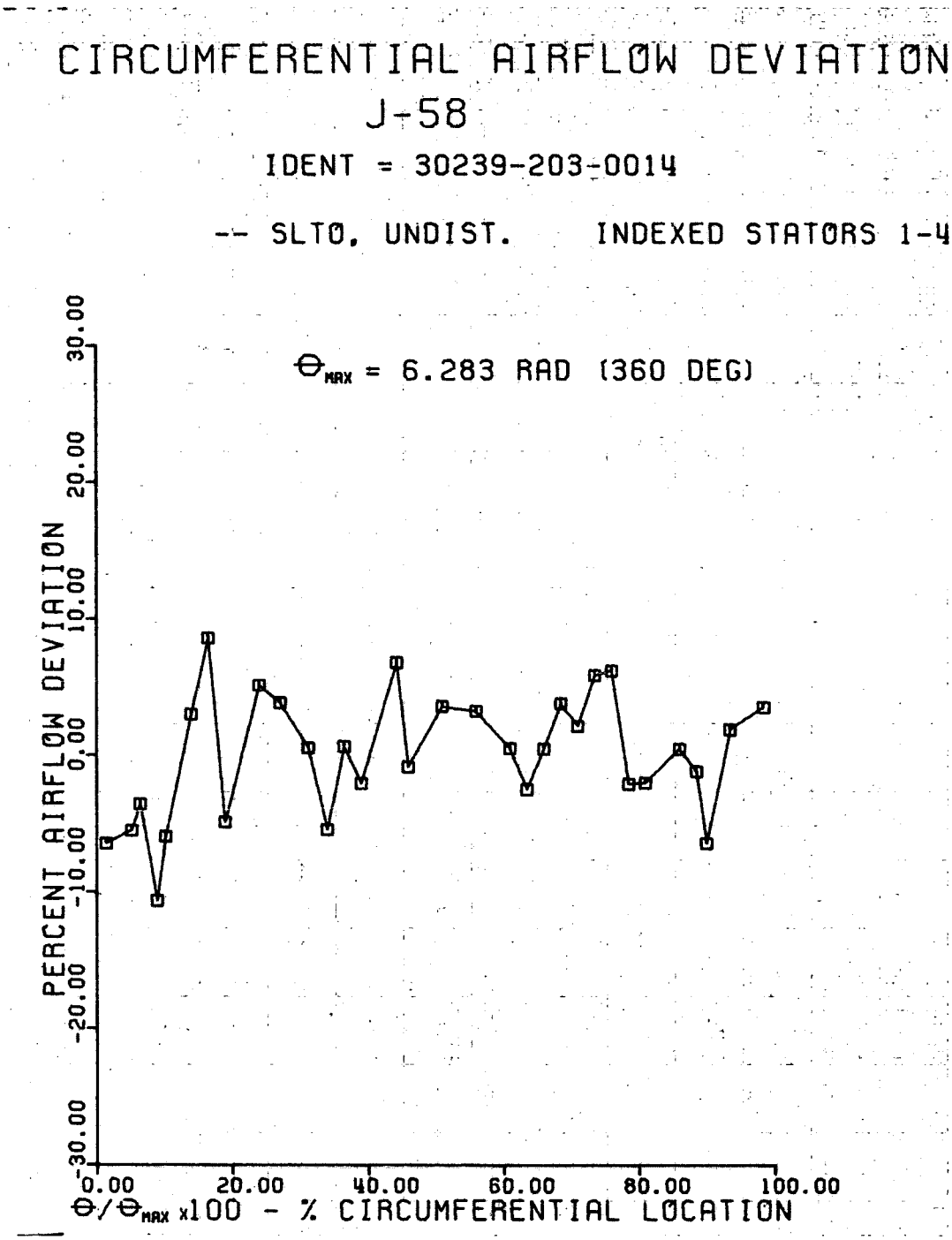

Figure 26.

DF 92051

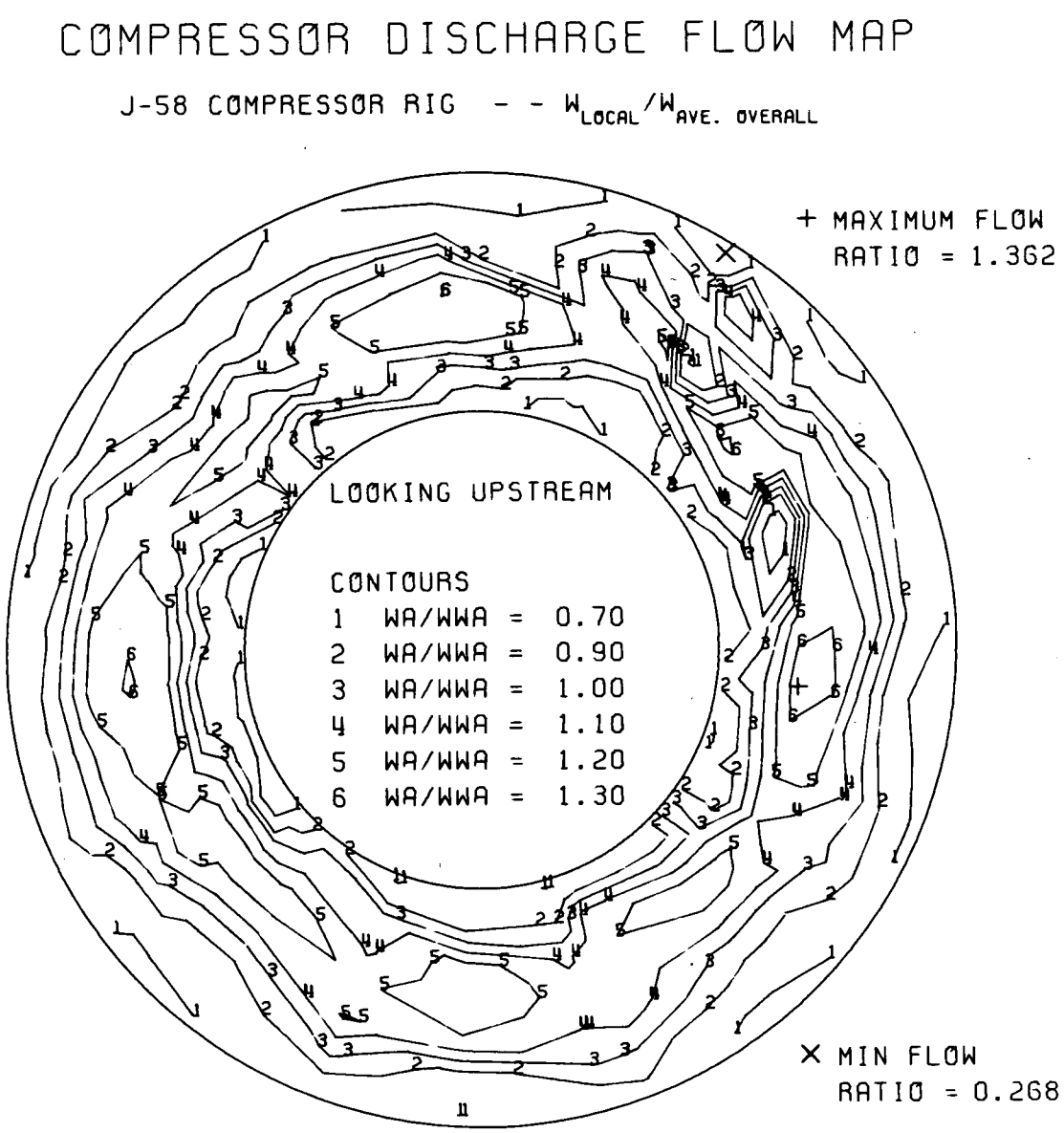

Figure 27.

DF 92068

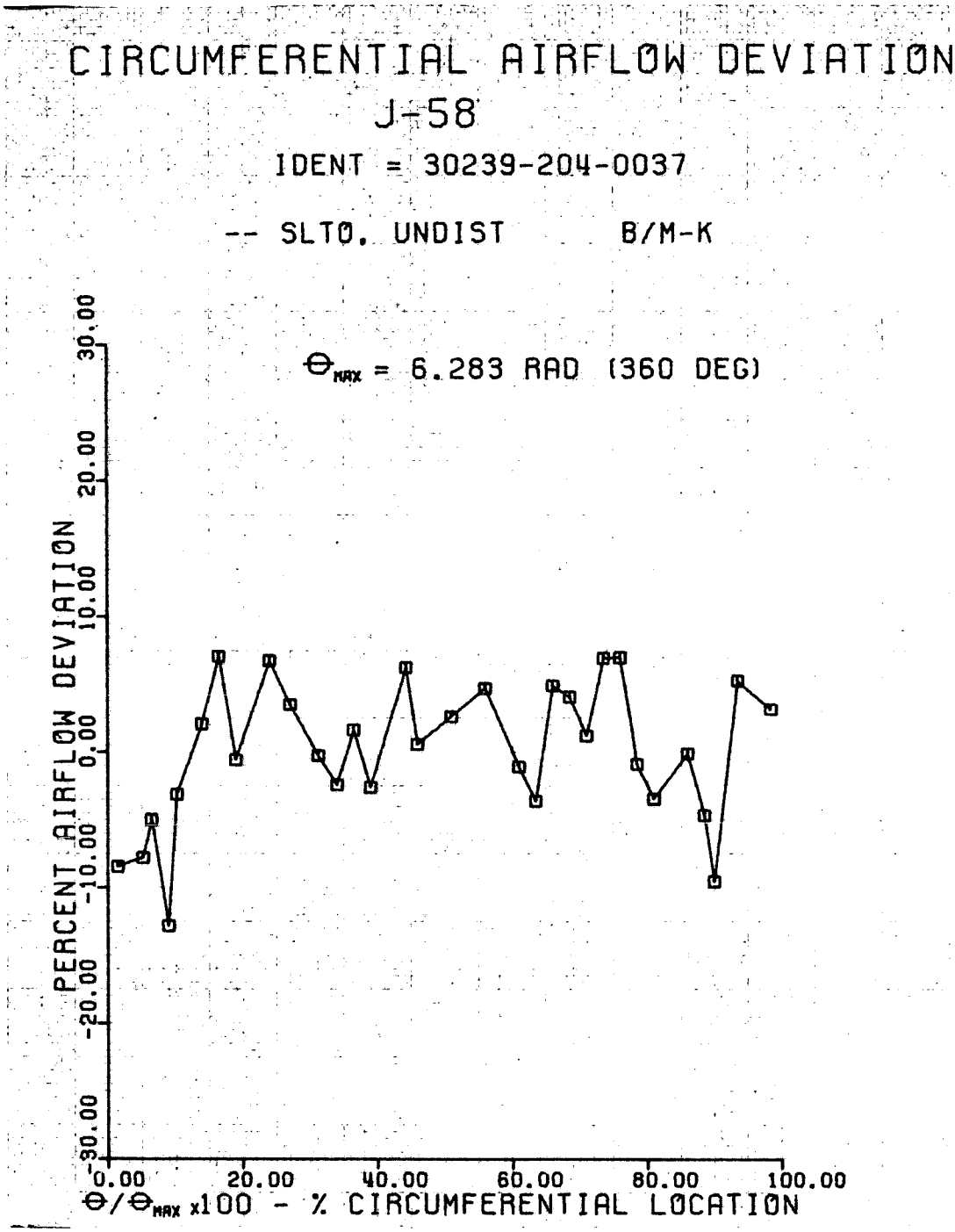

Figure 28. DF 92049

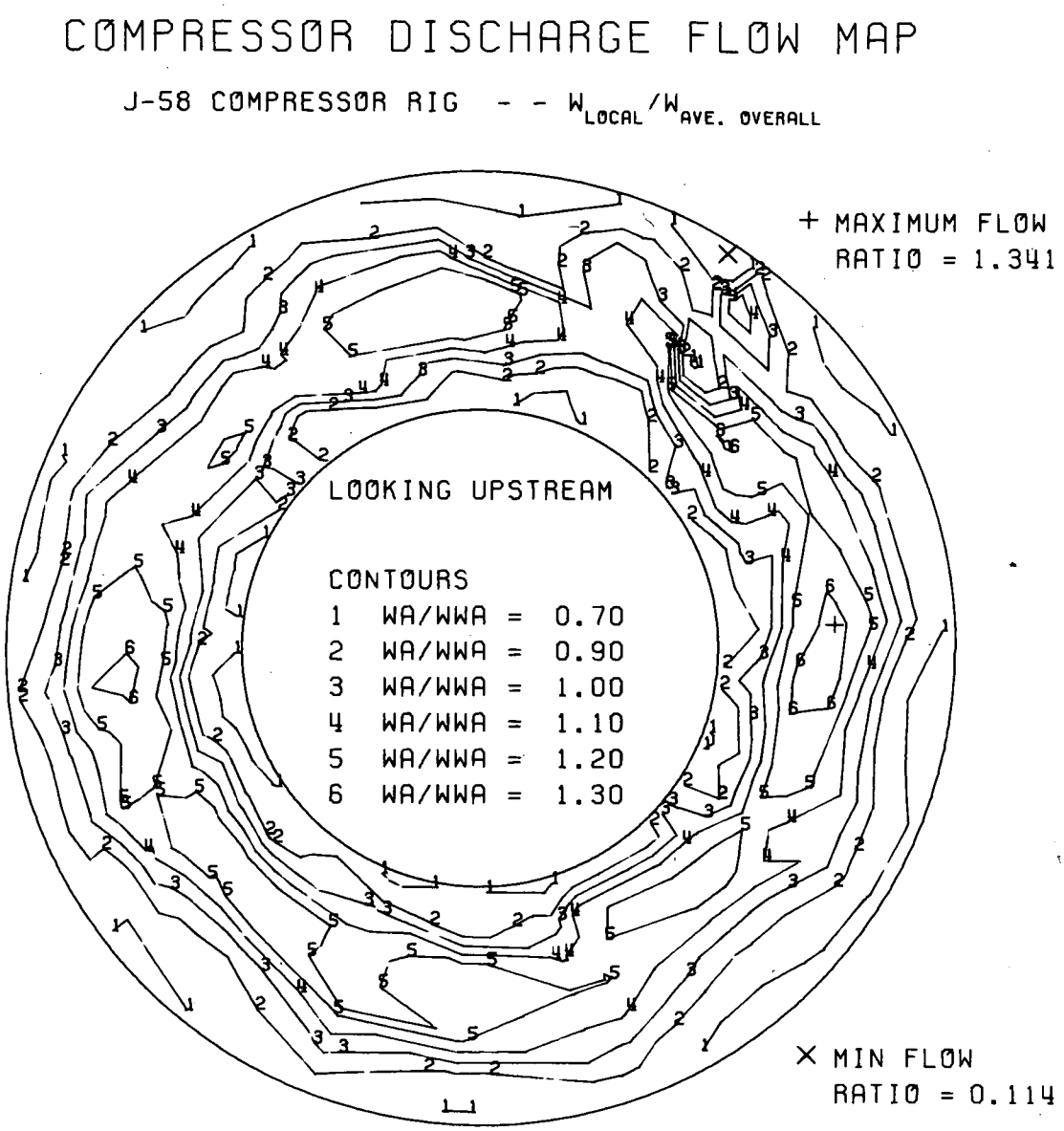

Figure 29.

DF 92067

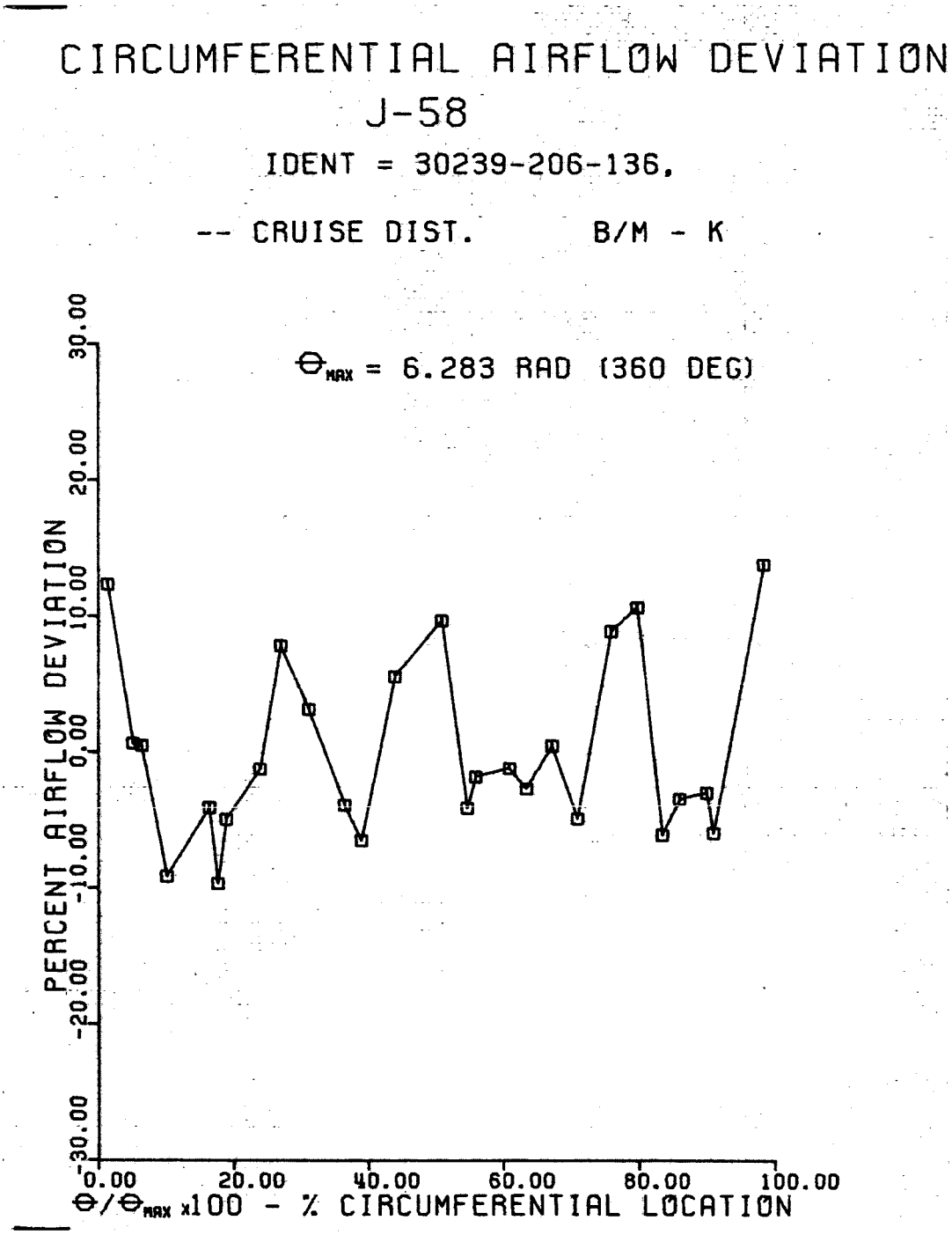

Figure 30.

DF 92048

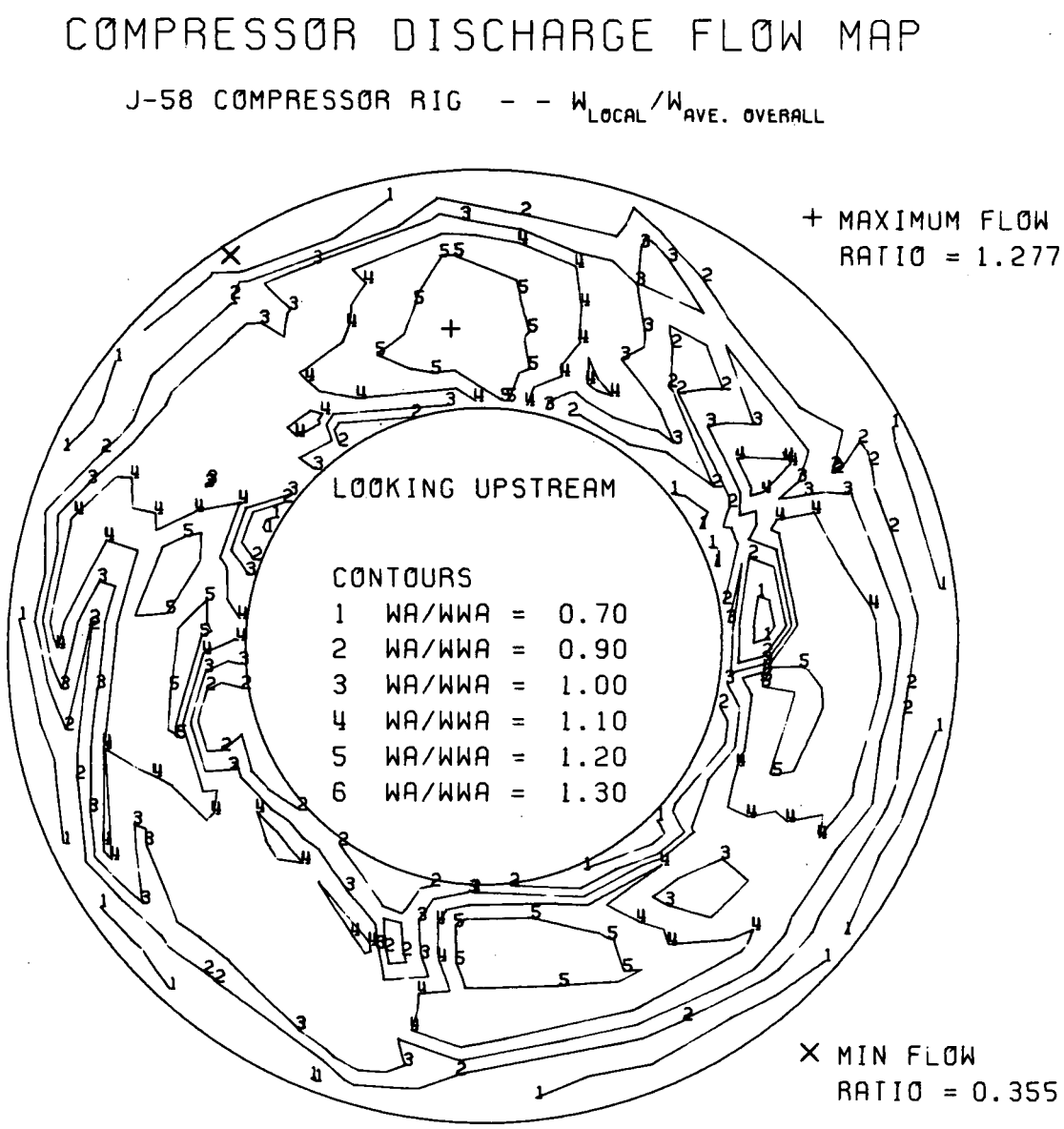

Figure 31.

DF 92066

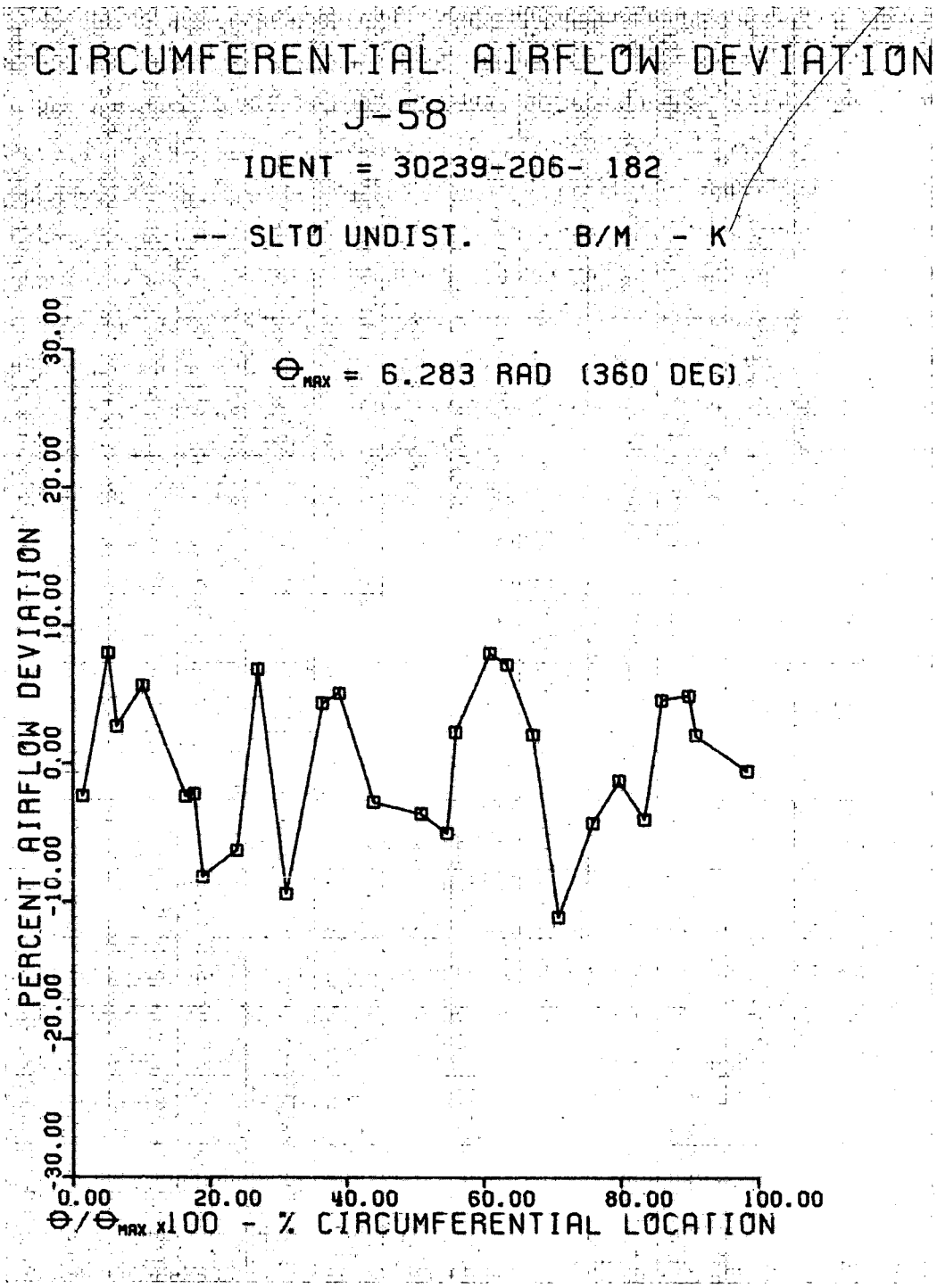

Figure 32.

DF 92059

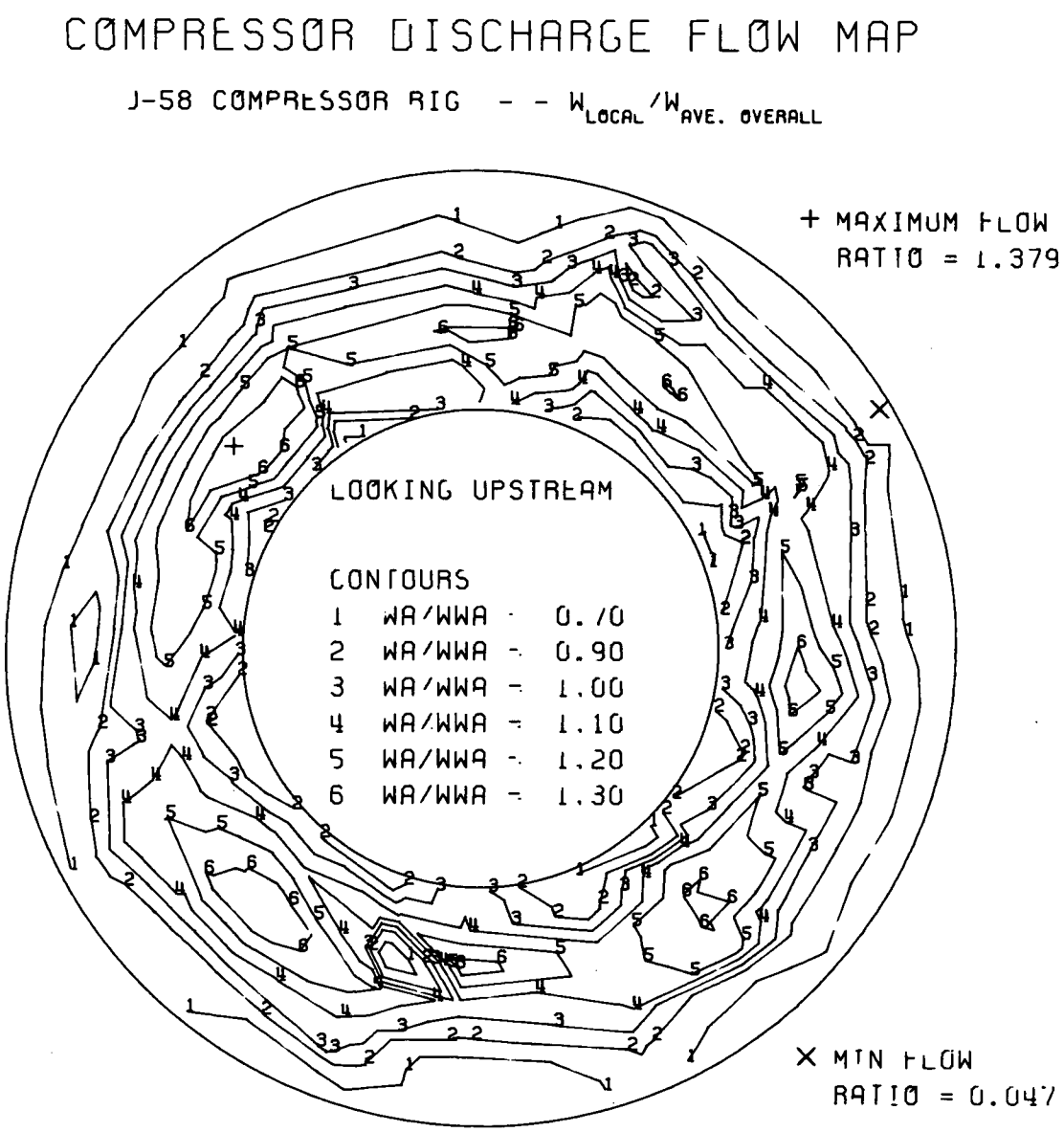

Figure 33.

DF 92060

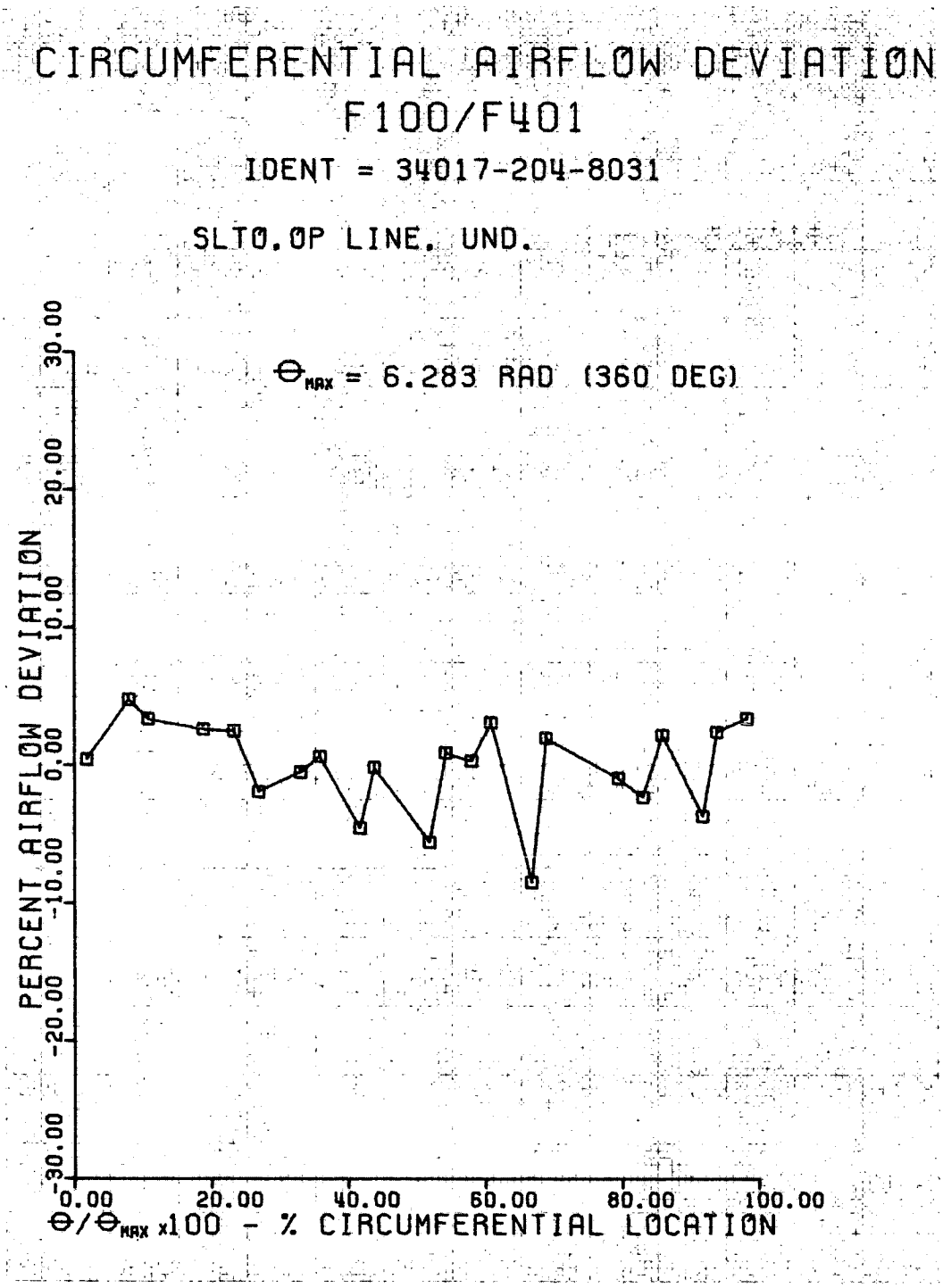

Figure 34.

DF 92091

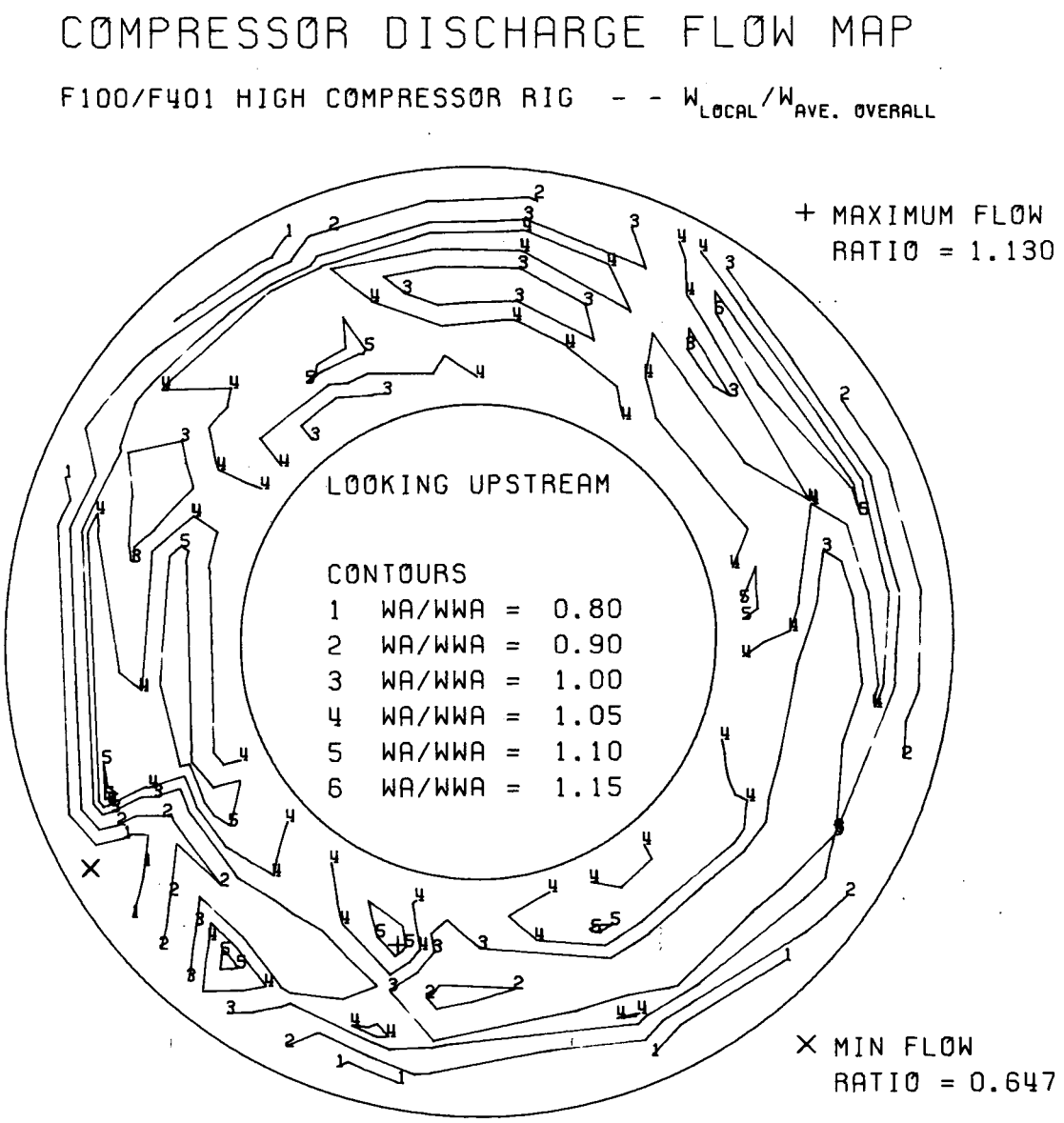

Figure 35.

DF 92072

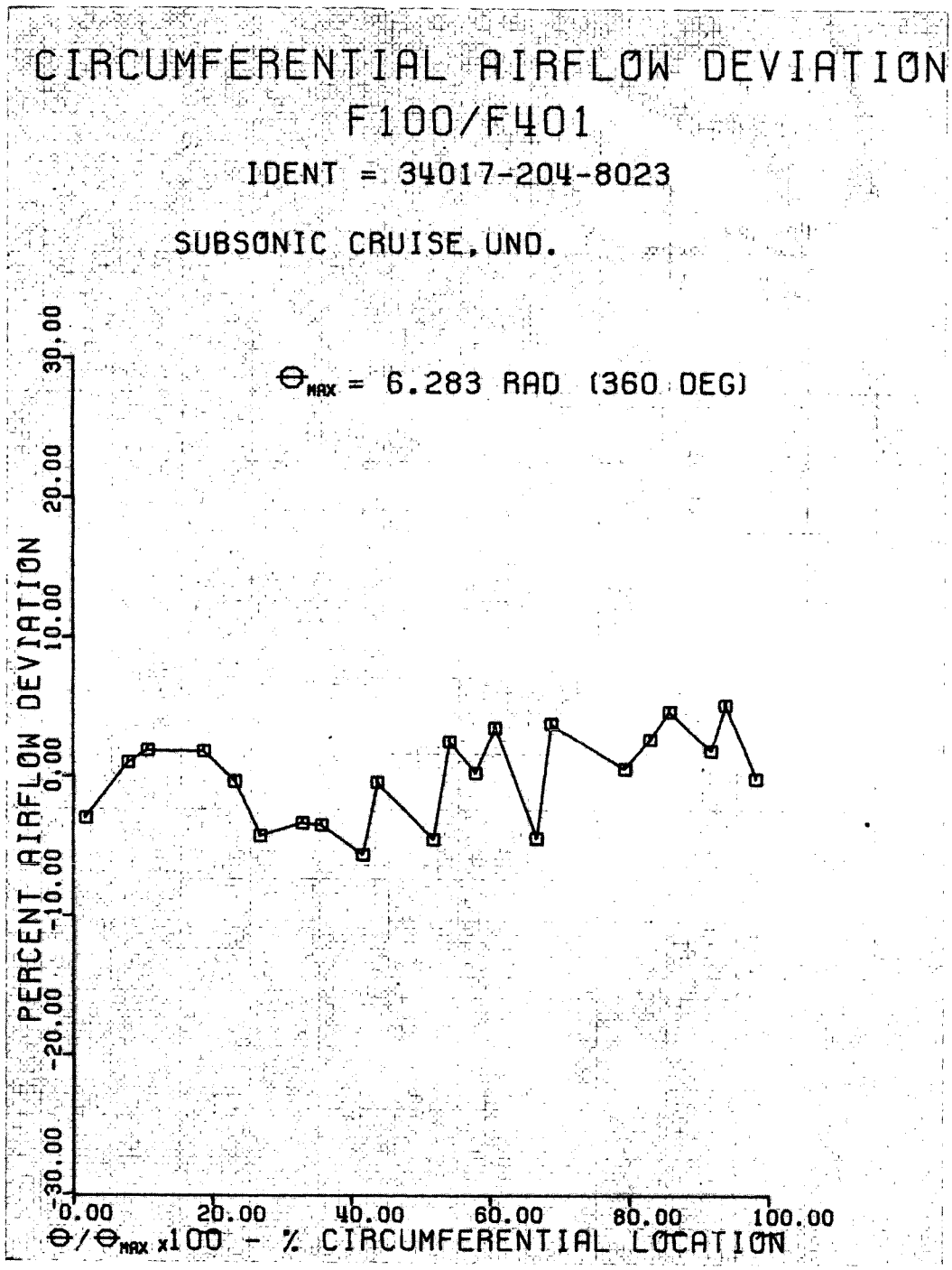

Figure 36.

DF 92092

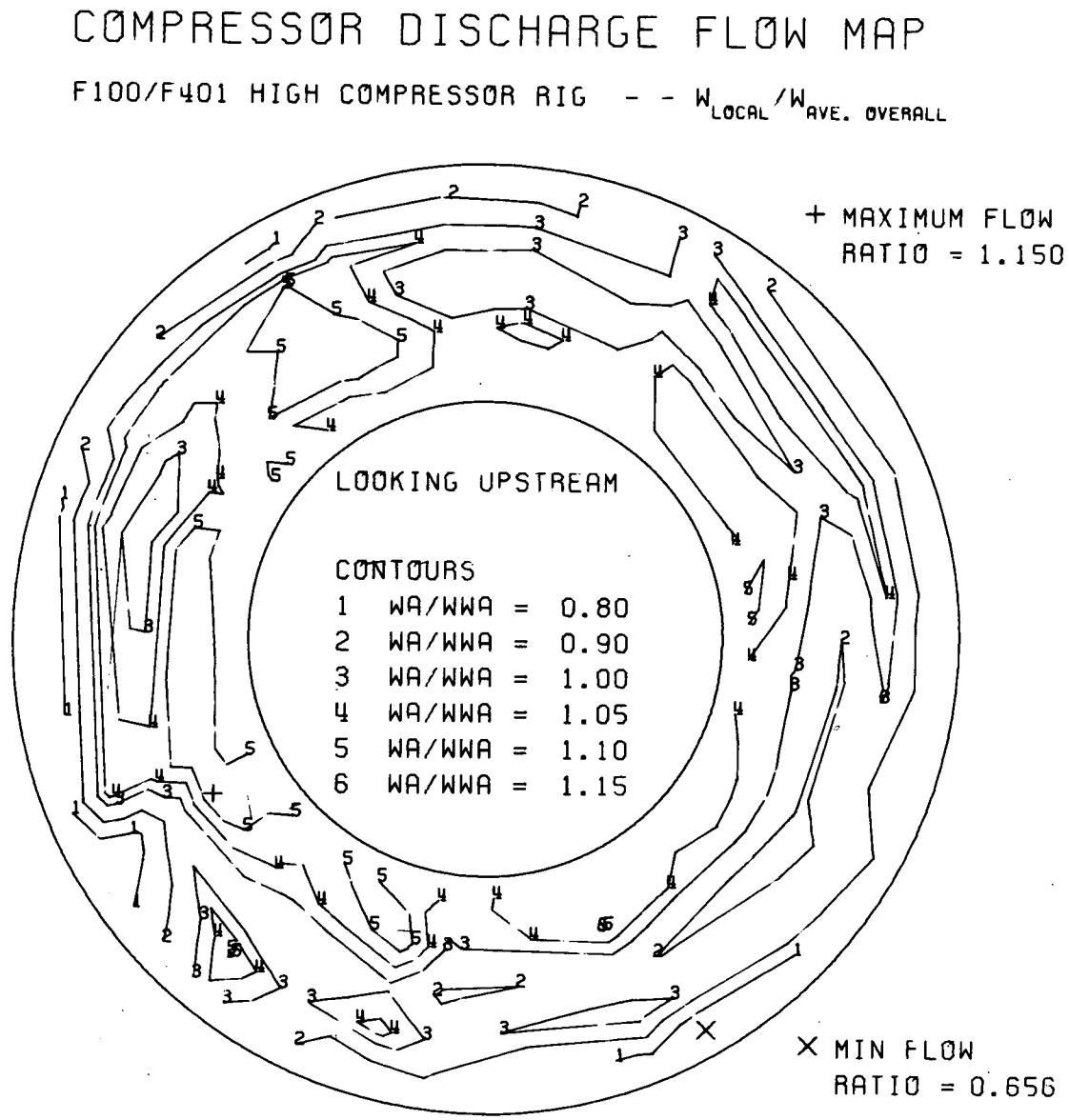

Figure 37.

DF 92073

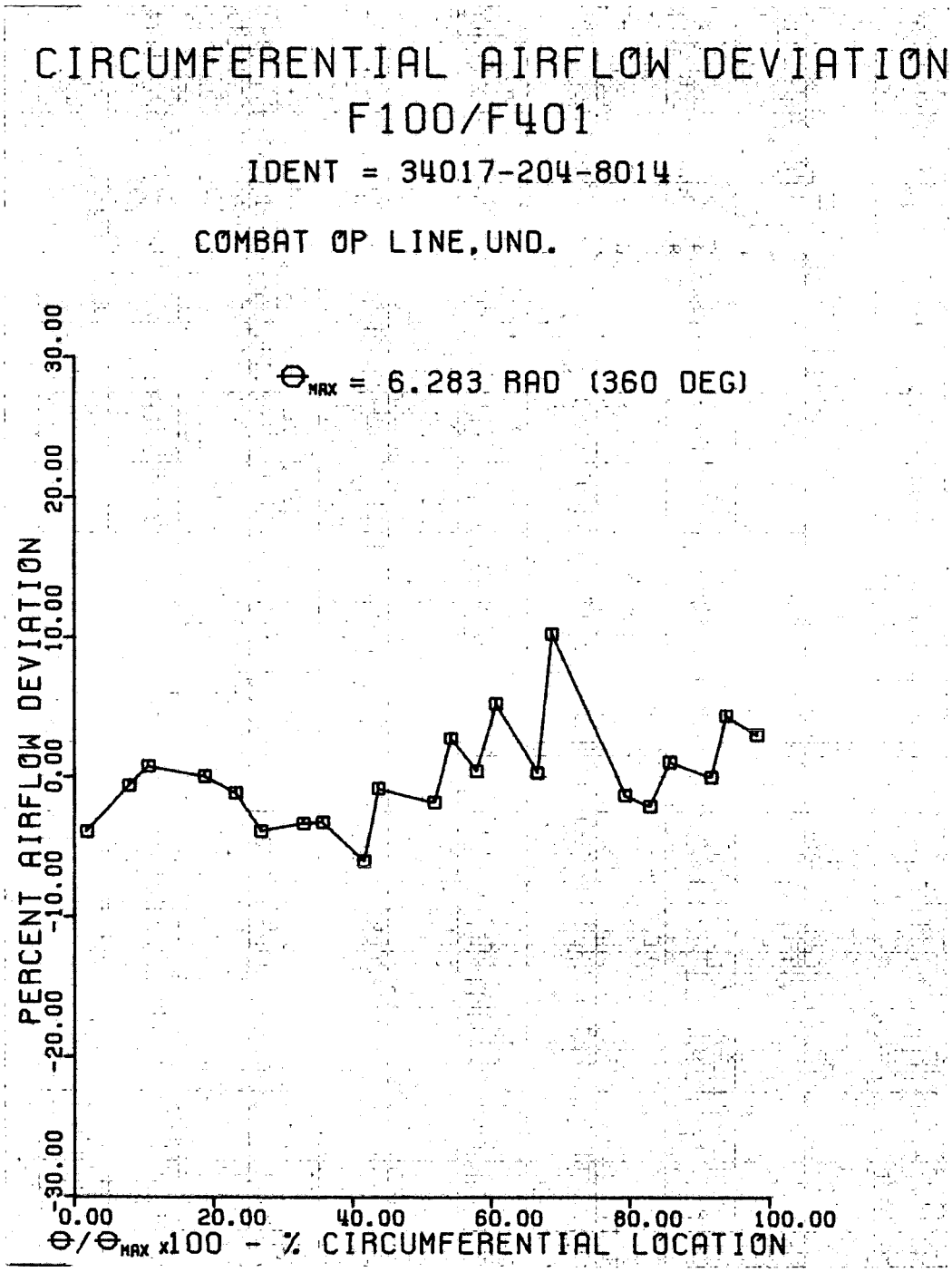

Figure 38.

DF 92093

COMPRESSOR DISCHARGE FLOW MAP

F100/F401 HIGH COMPRESSOR RIG - - $W_{LOCAL}/W_{AVE.\ OVERALL}$

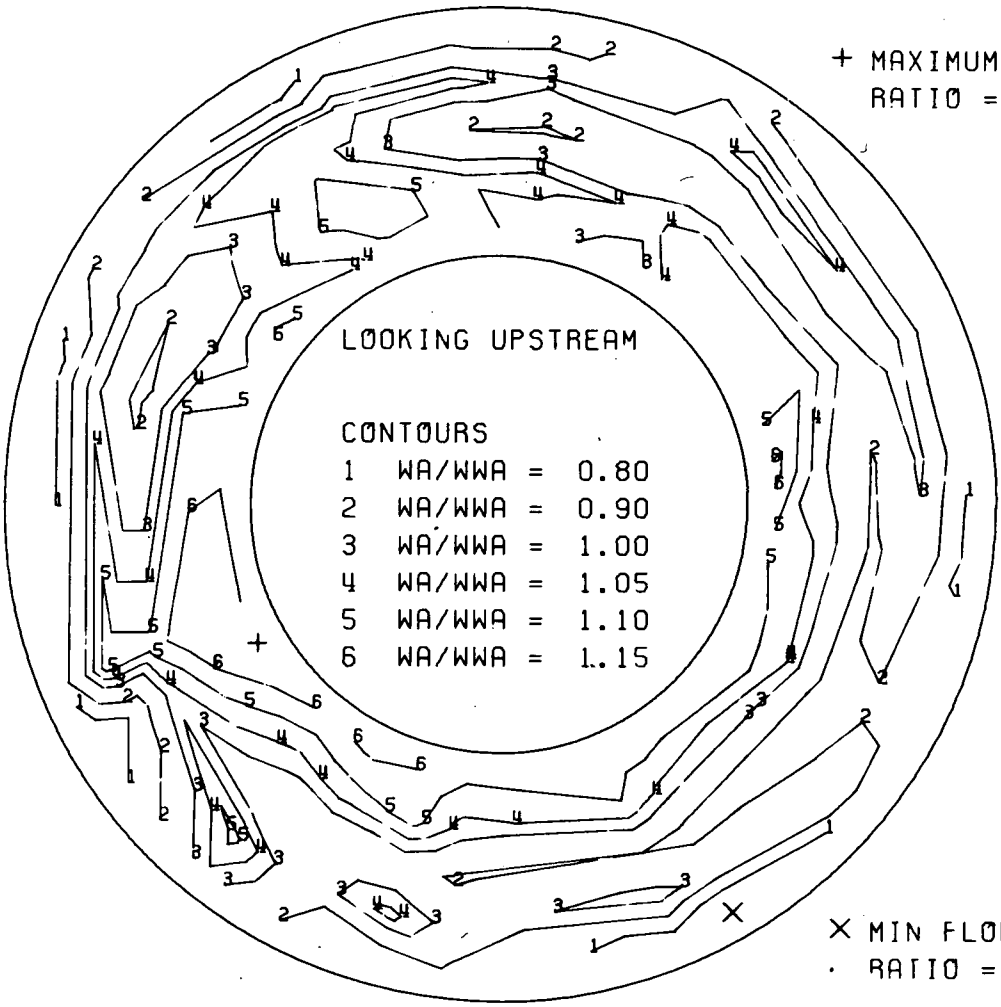

RIG NO.34017 BUILD NO.=204 RUN NO.=8014 CONDITION- COMBAT OP LINE,UND.

Figure 39.

DF 92074

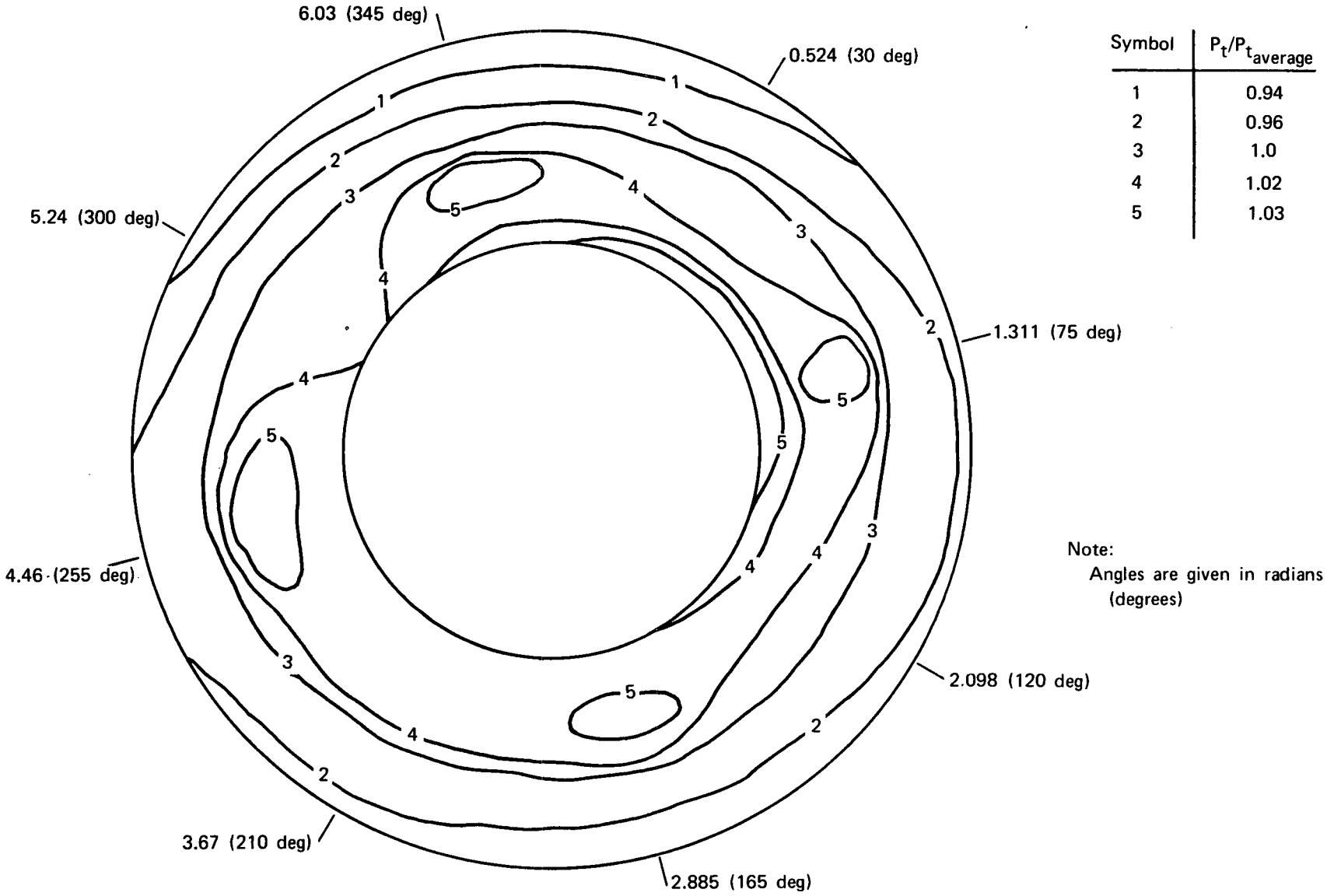

Figure 40. F100/F401 High Compressor Inlet Pressure Map, No Distortion; Build 205, Run 4313 FD 63398

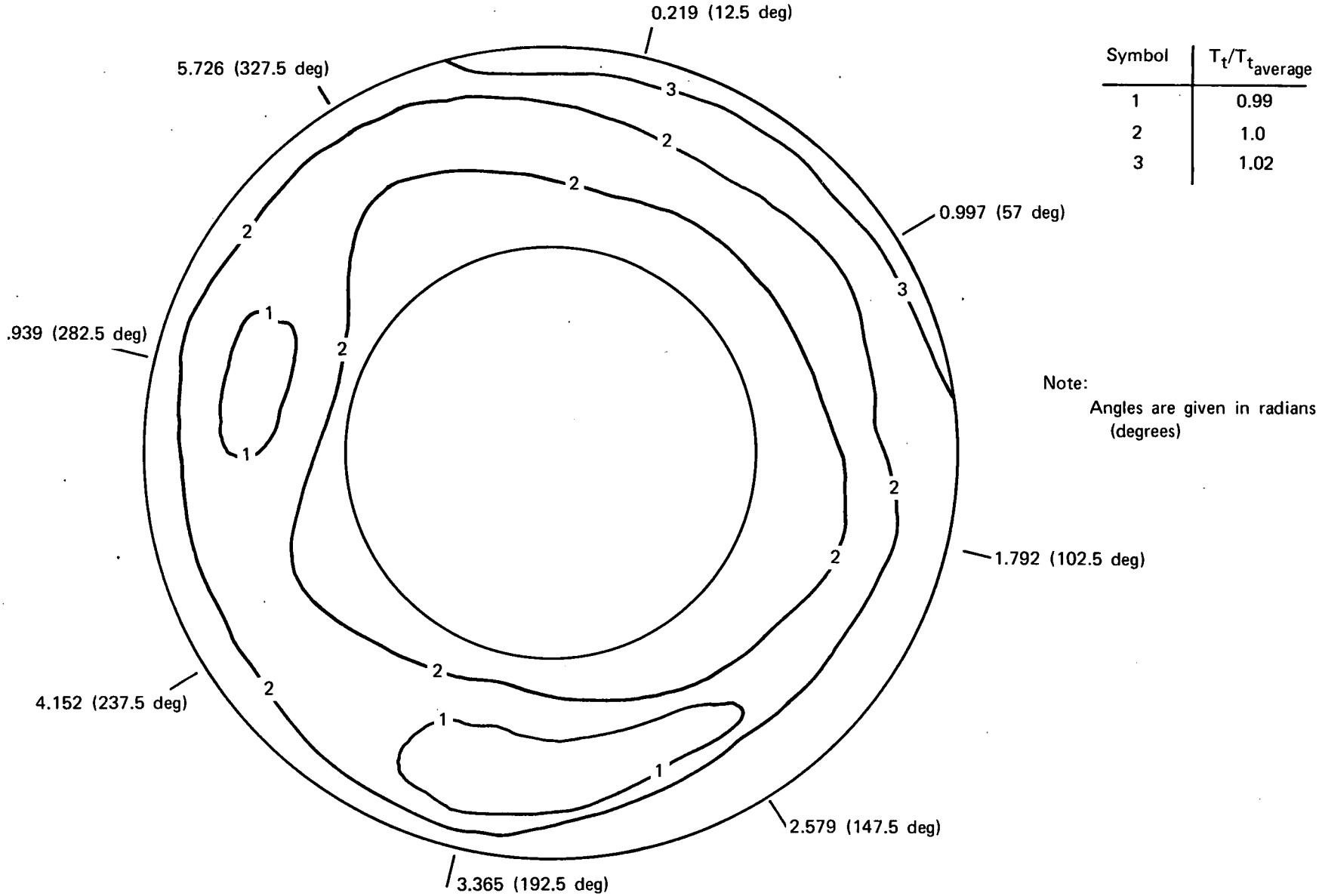

Figure 41. F100/F401 High Compressor Inlet Temperature Map, No Distortion; Build 205, Run 4313 FD 63399

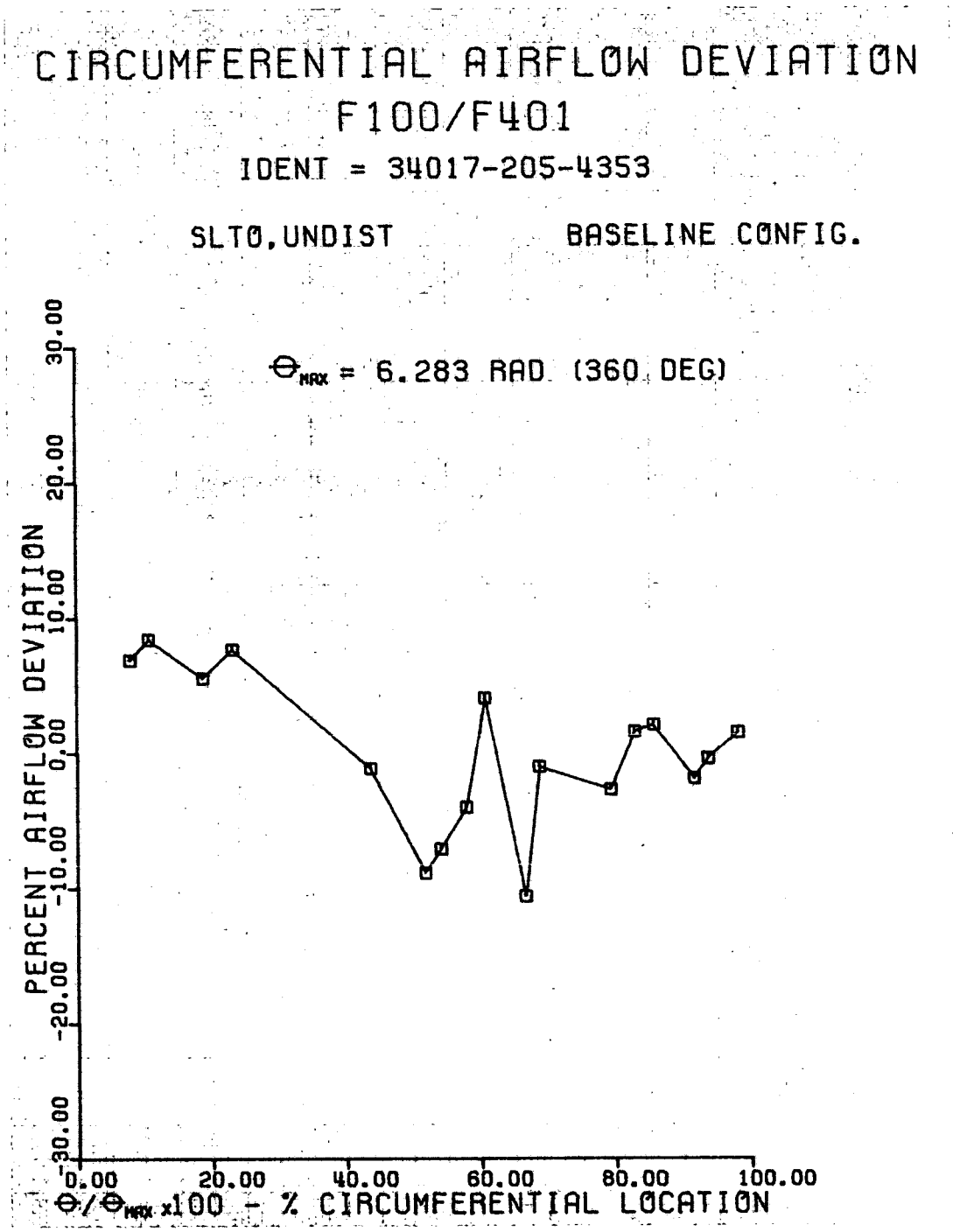

Figure 42.

DF 92094

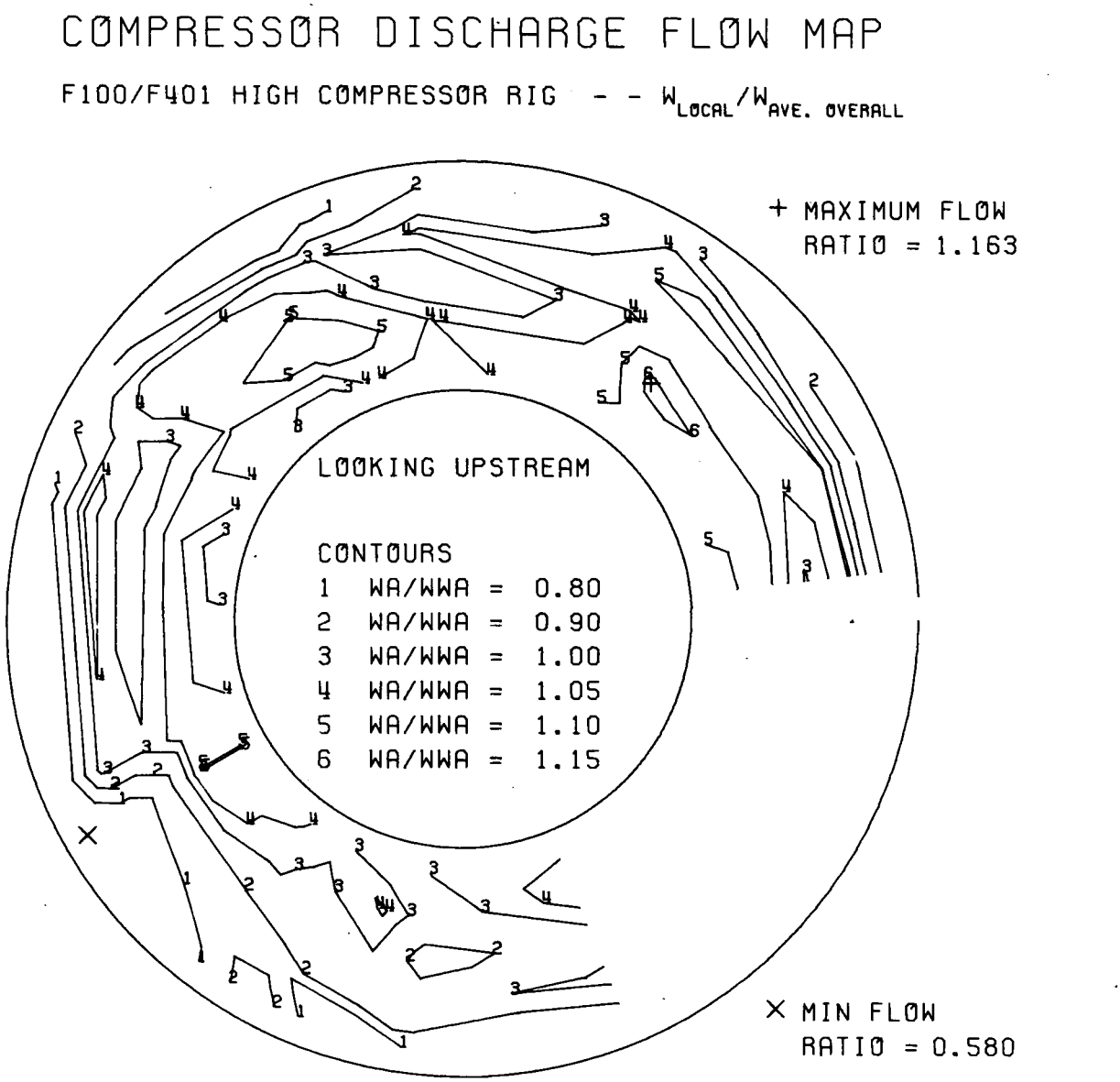

Figure 43.

DF 92075

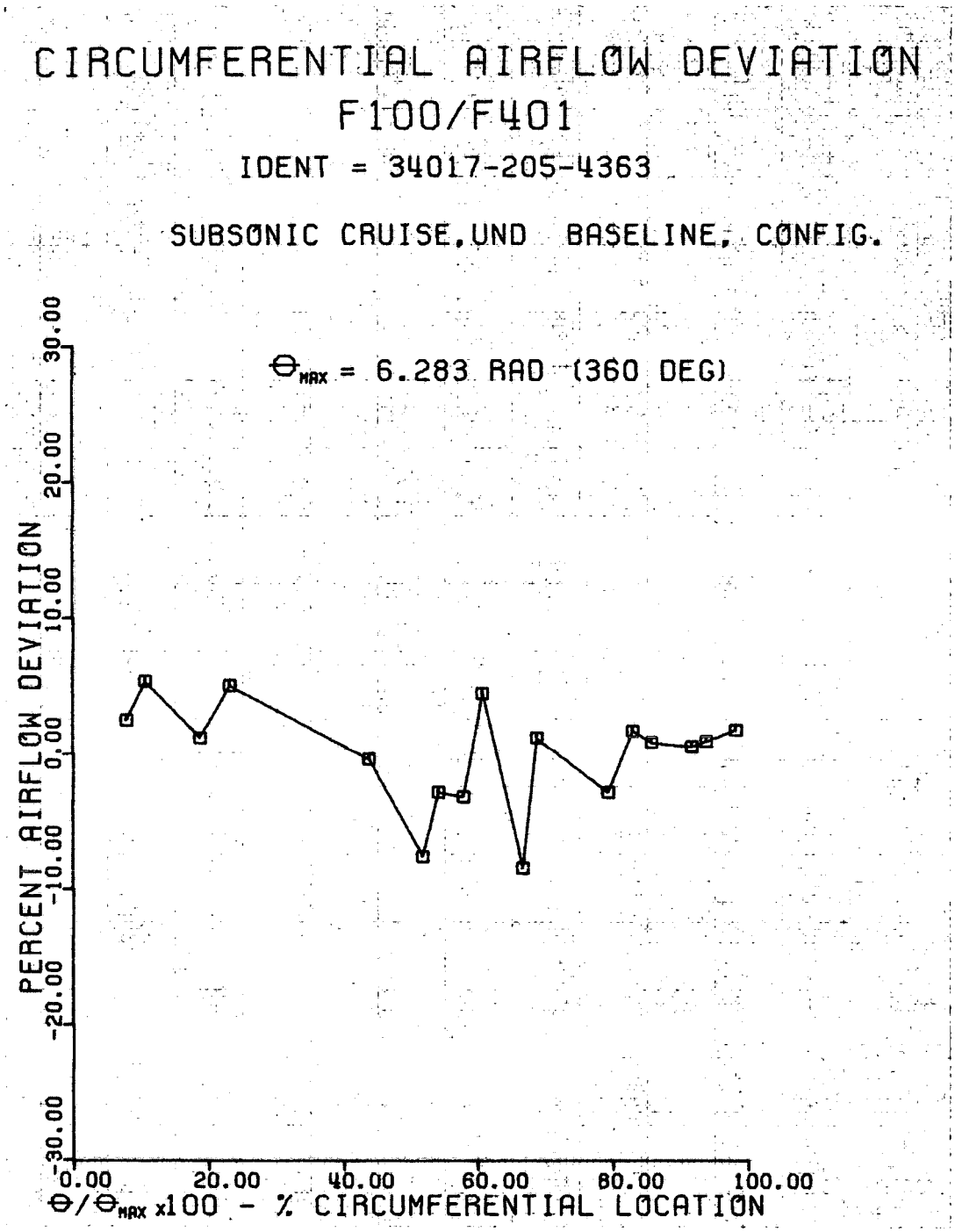

Figure 44.

DF 92095

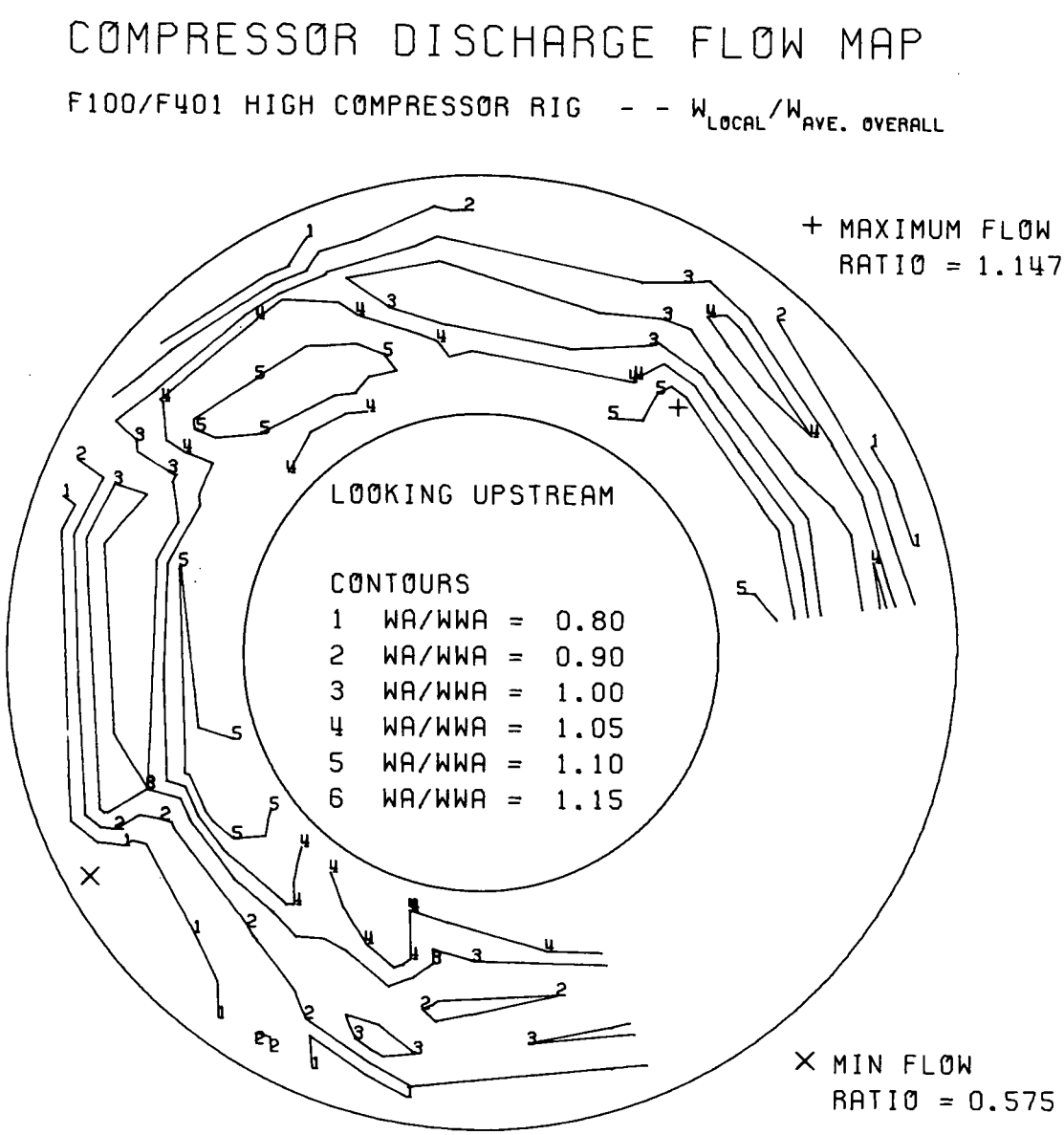

RIG NO.34017 BUILD NO.=205 RUN NO.=4363 CONDITION-SUBSONIC CRUISE,UND

Figure 45.

DF 92076

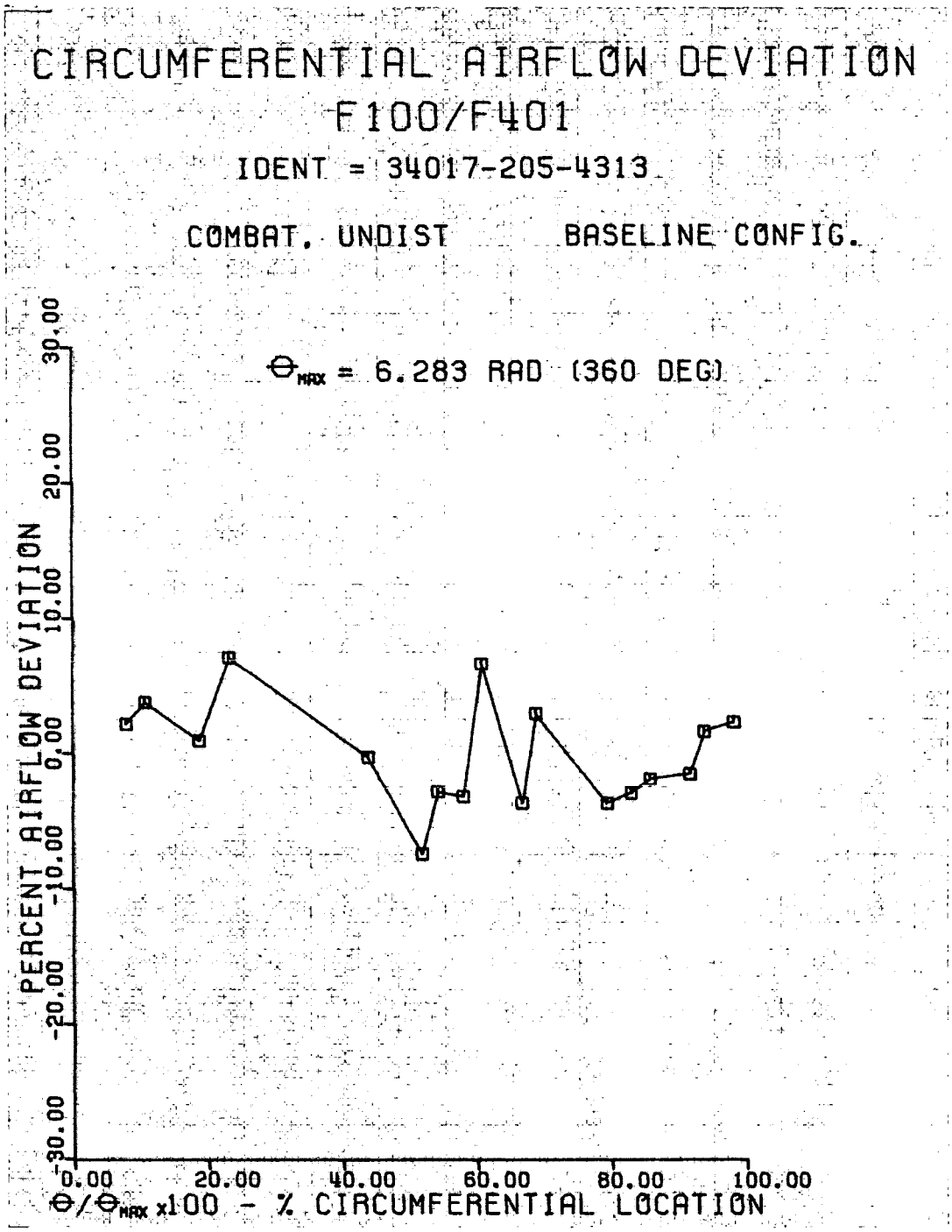

Figure 46.

DF 92096

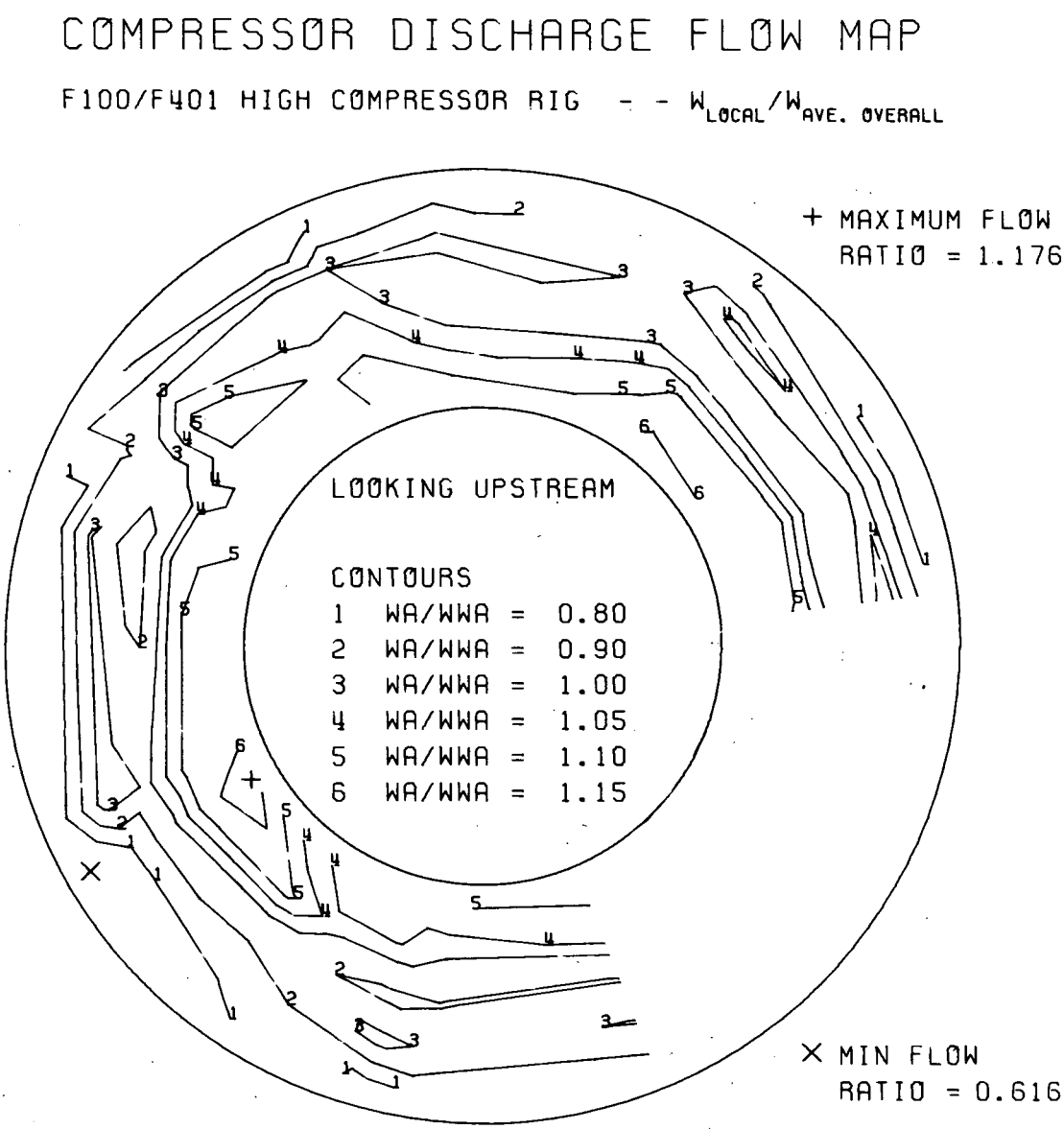

Figure 47.

DF 92077

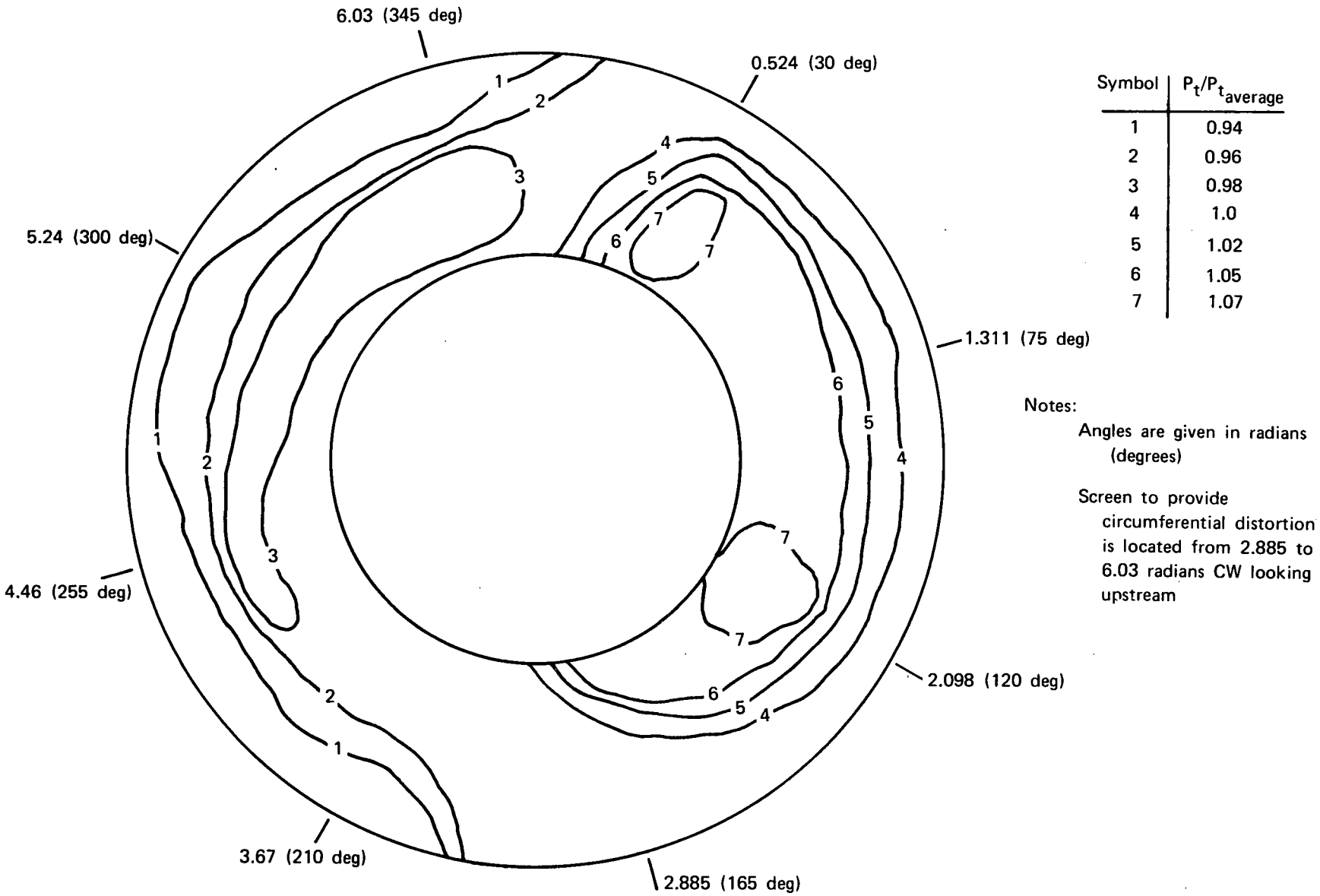

Figure 48. F100/F401 High Compressor Inlet Pressure Map With Aerodynamic Distortion; Build 205, Run 4233

FD 63400

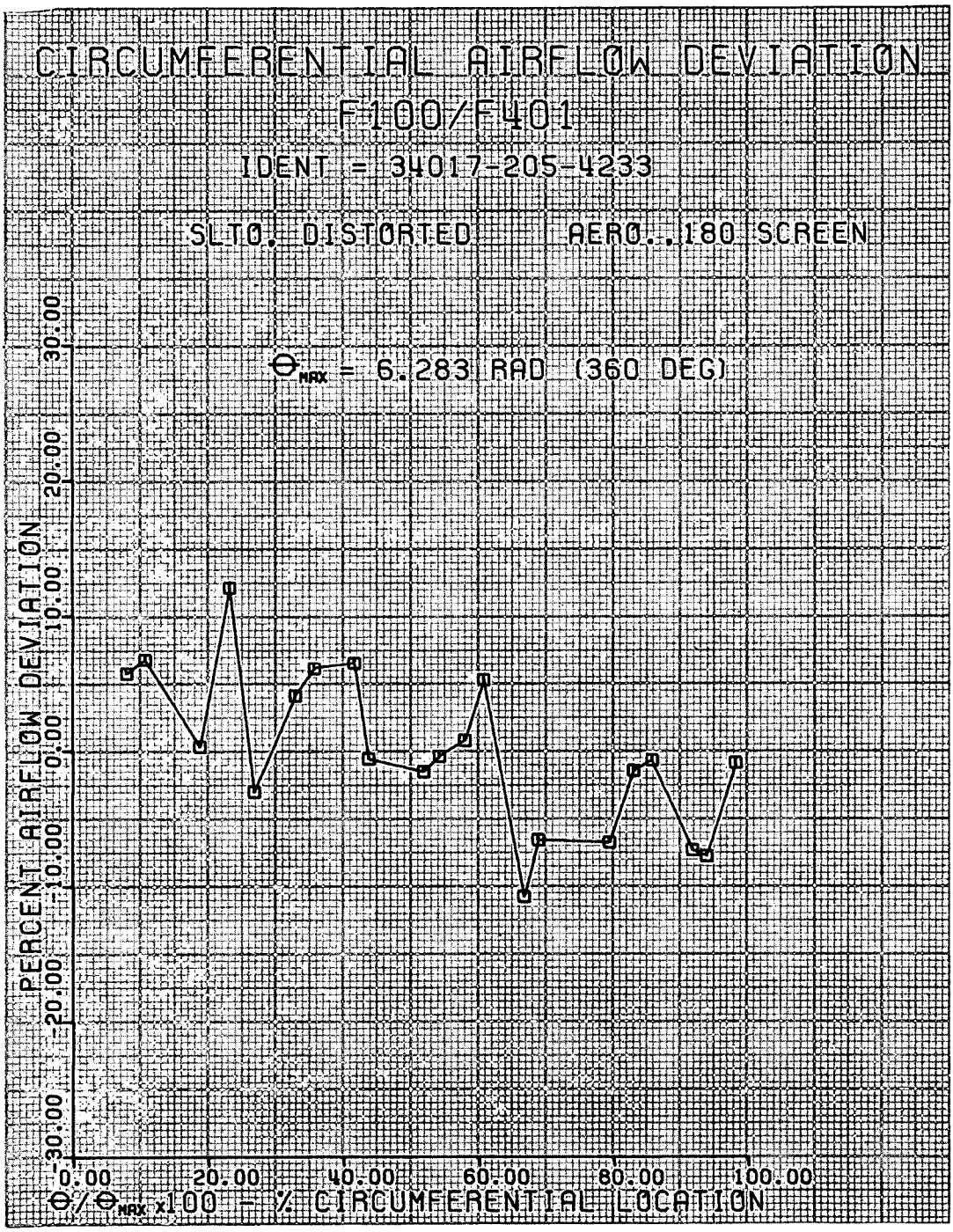

Figure 49.

DF 92097

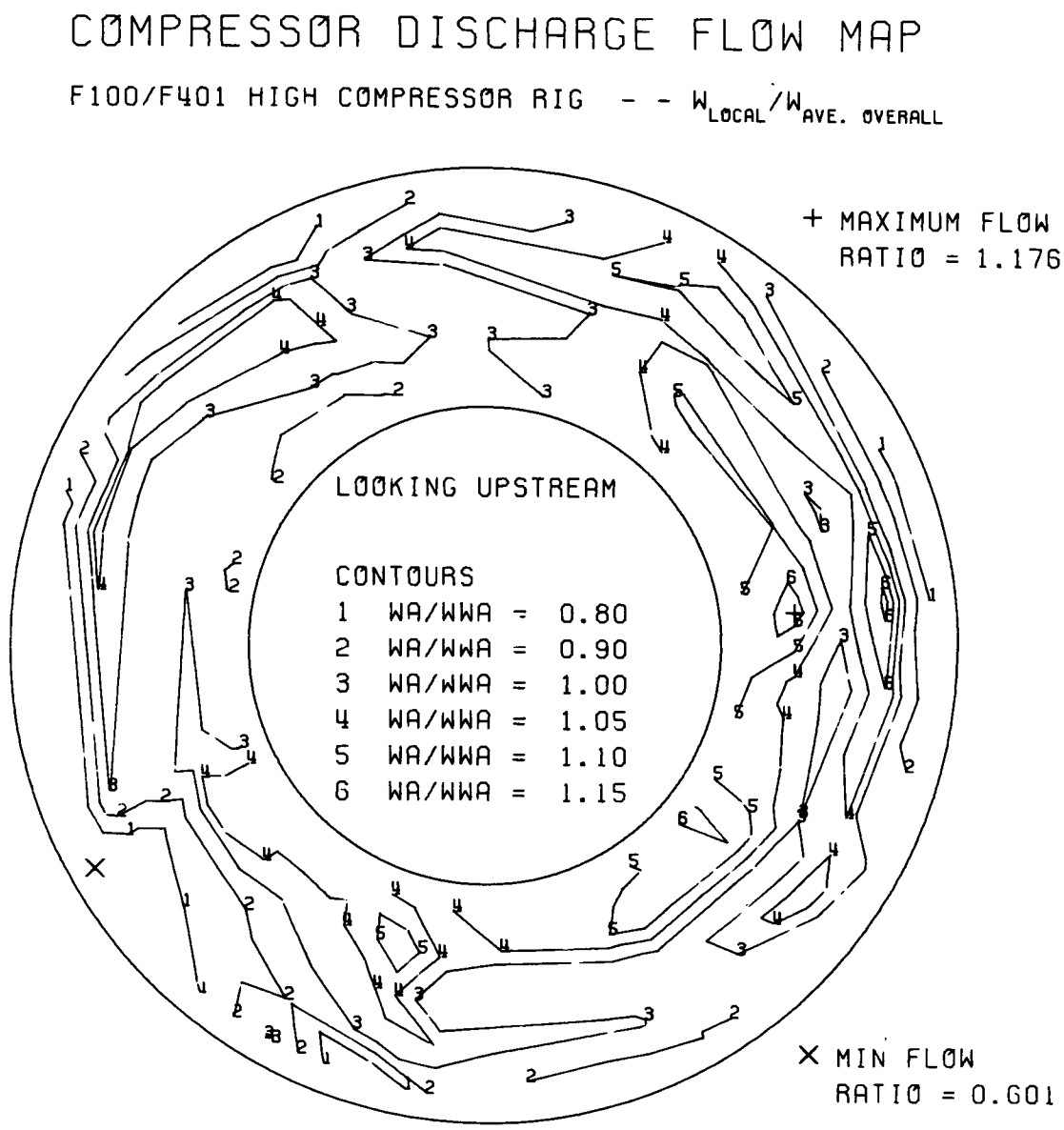

Figure 50.

DF 92078

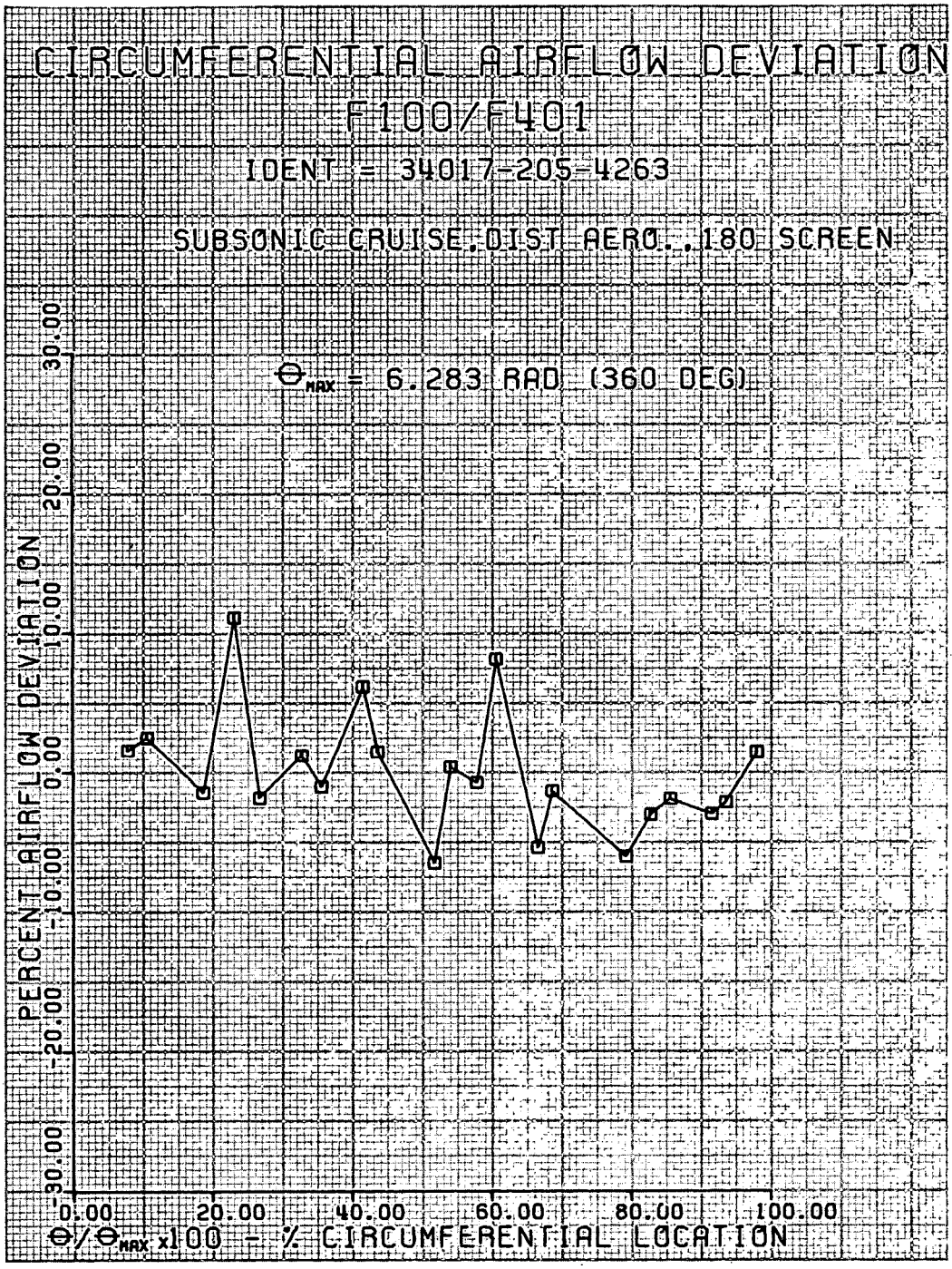

Figure 51.

DF 92098

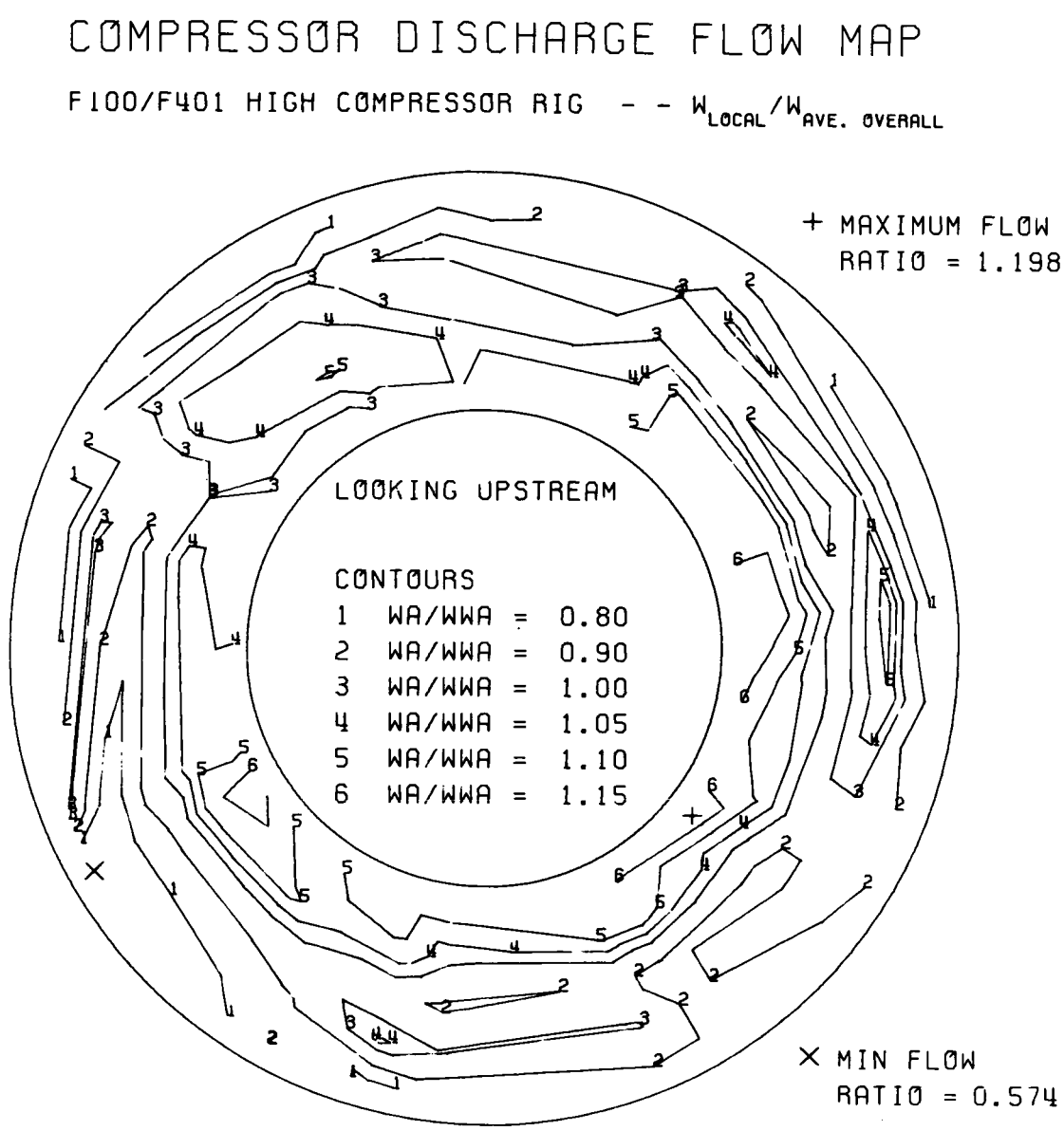

Figure 52.

DF 92079

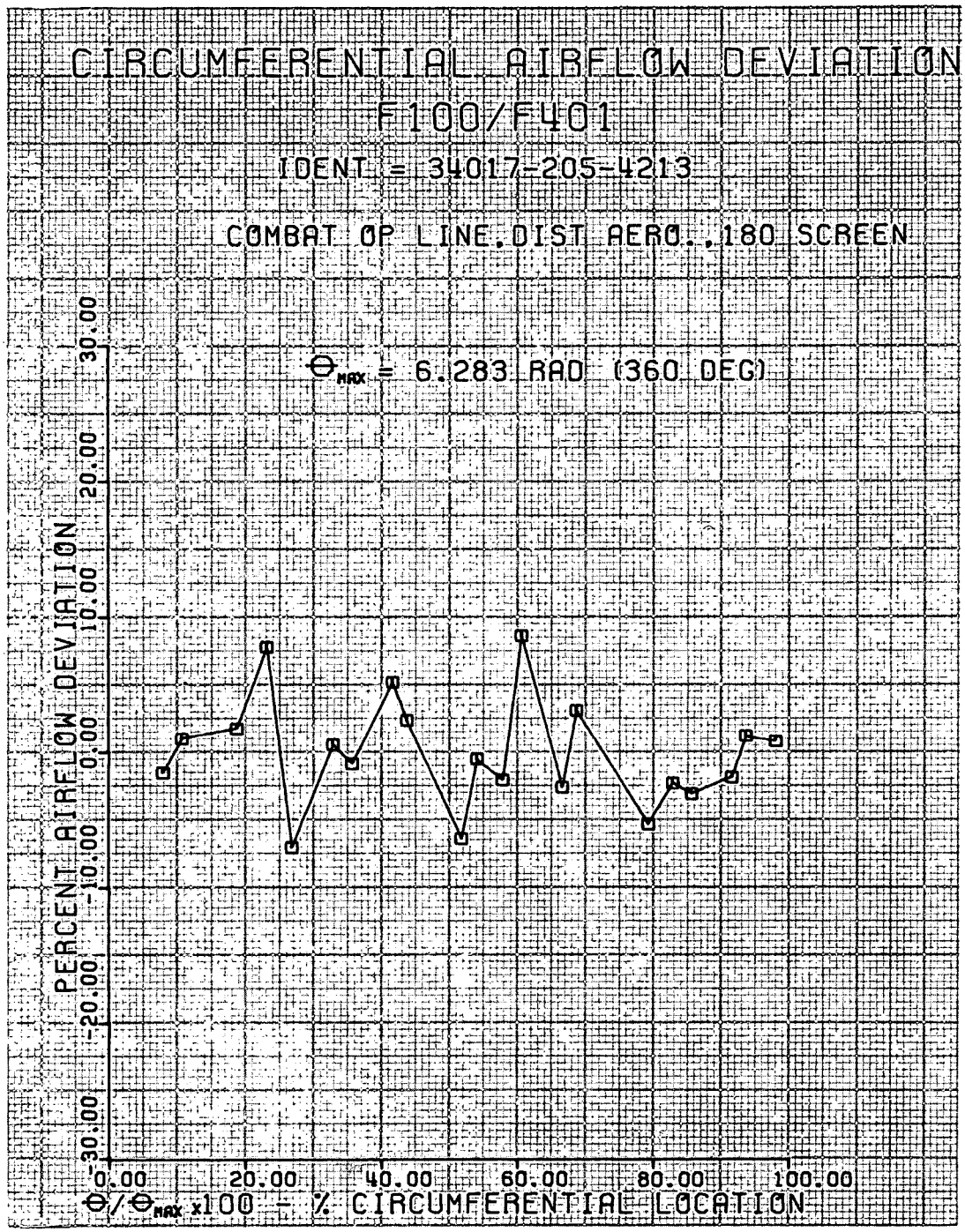

Figure 53.

DF 92099

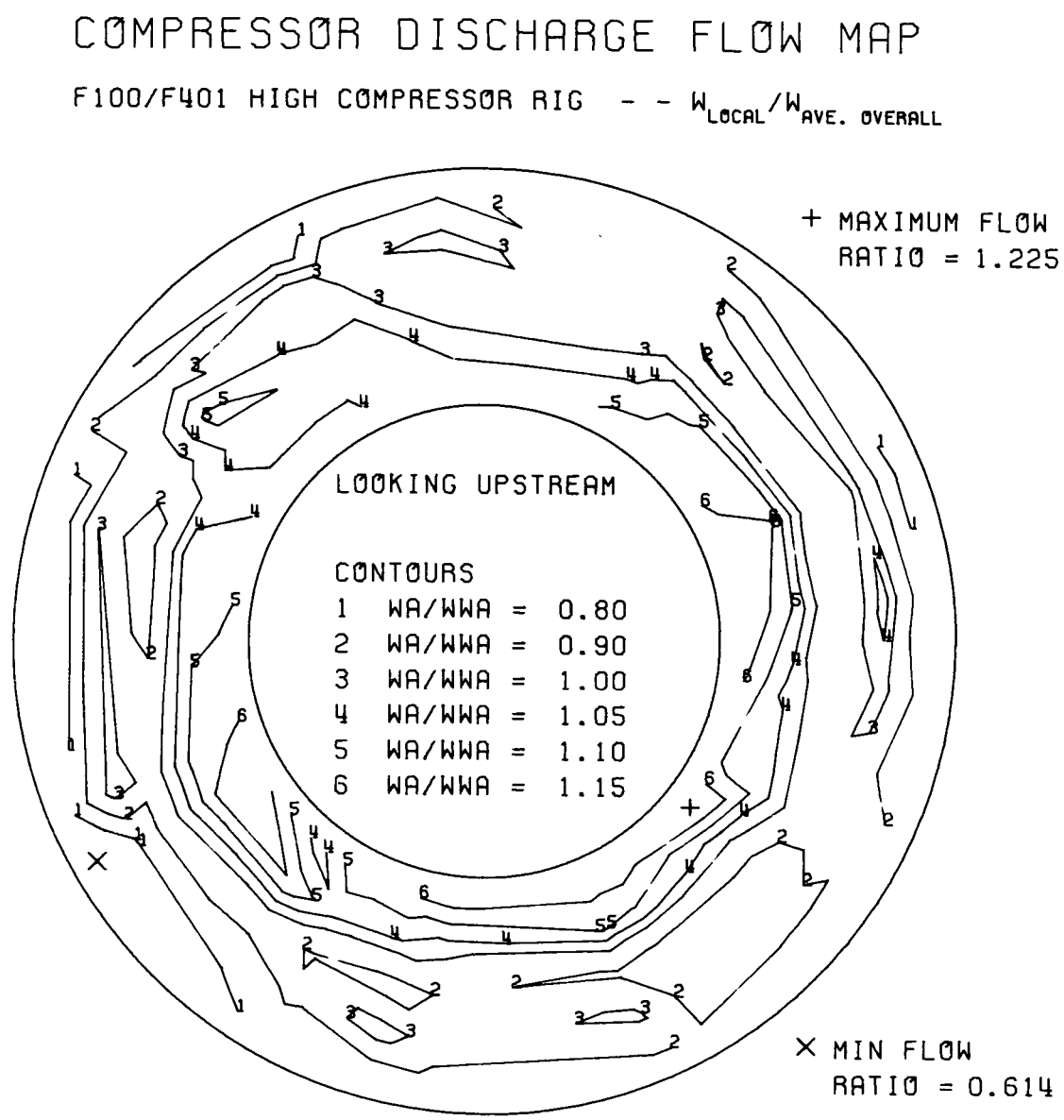

Figure 54.

DF 92080

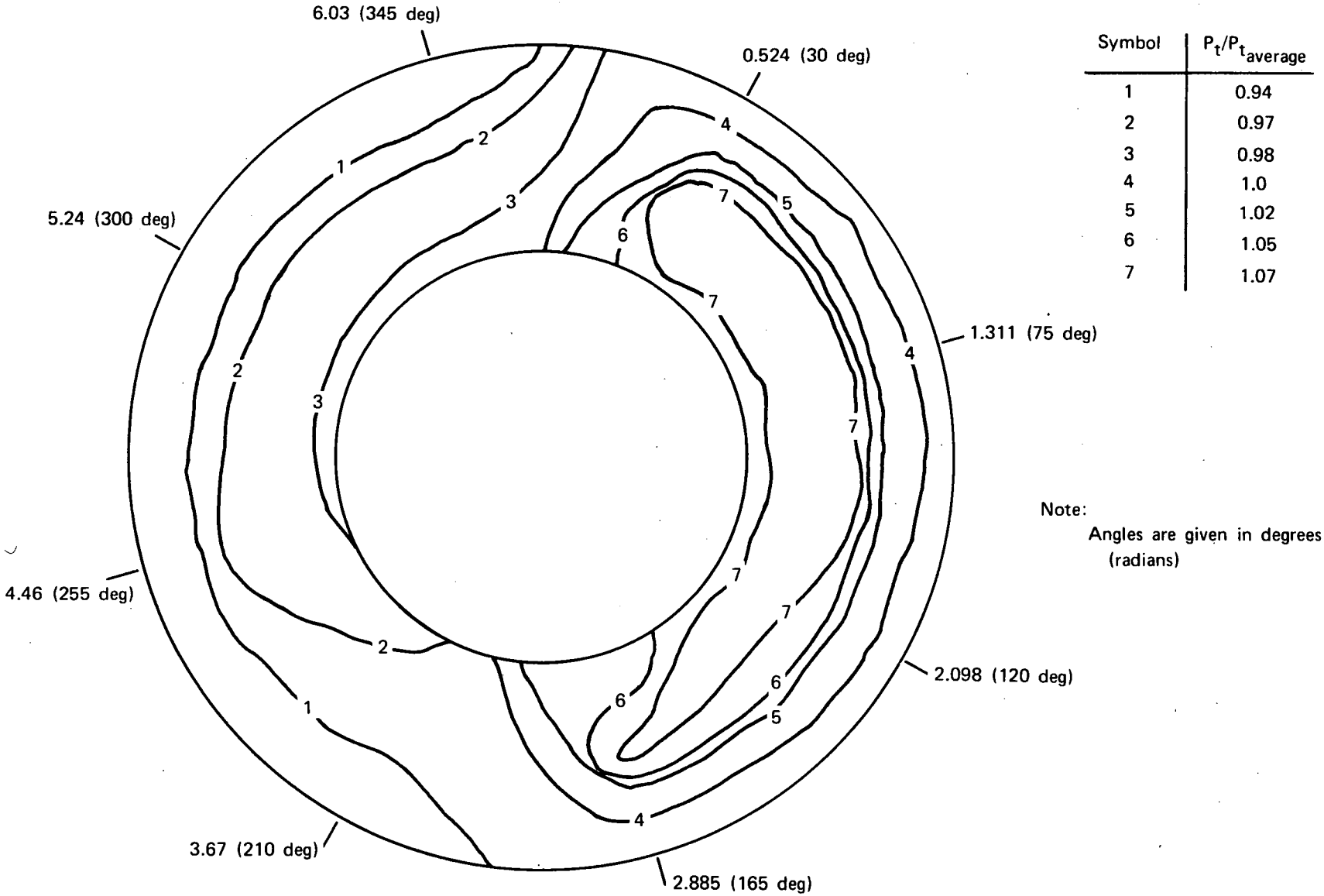

Symbol	$P_t/P_{t_{average}}$
1	0.94
2	0.97
3	0.98
4	1.0
5	1.02
6	1.05
7	1.07

Note:
Angles are given in degrees (radians)

Figure 55. F100/F401 High Compressor Inlet Pressure Map With Aerodynamic and Thermal Distortion, $\Delta T = 22\,°K$ (40 °F); Build 205, Run 4453

FD 63402

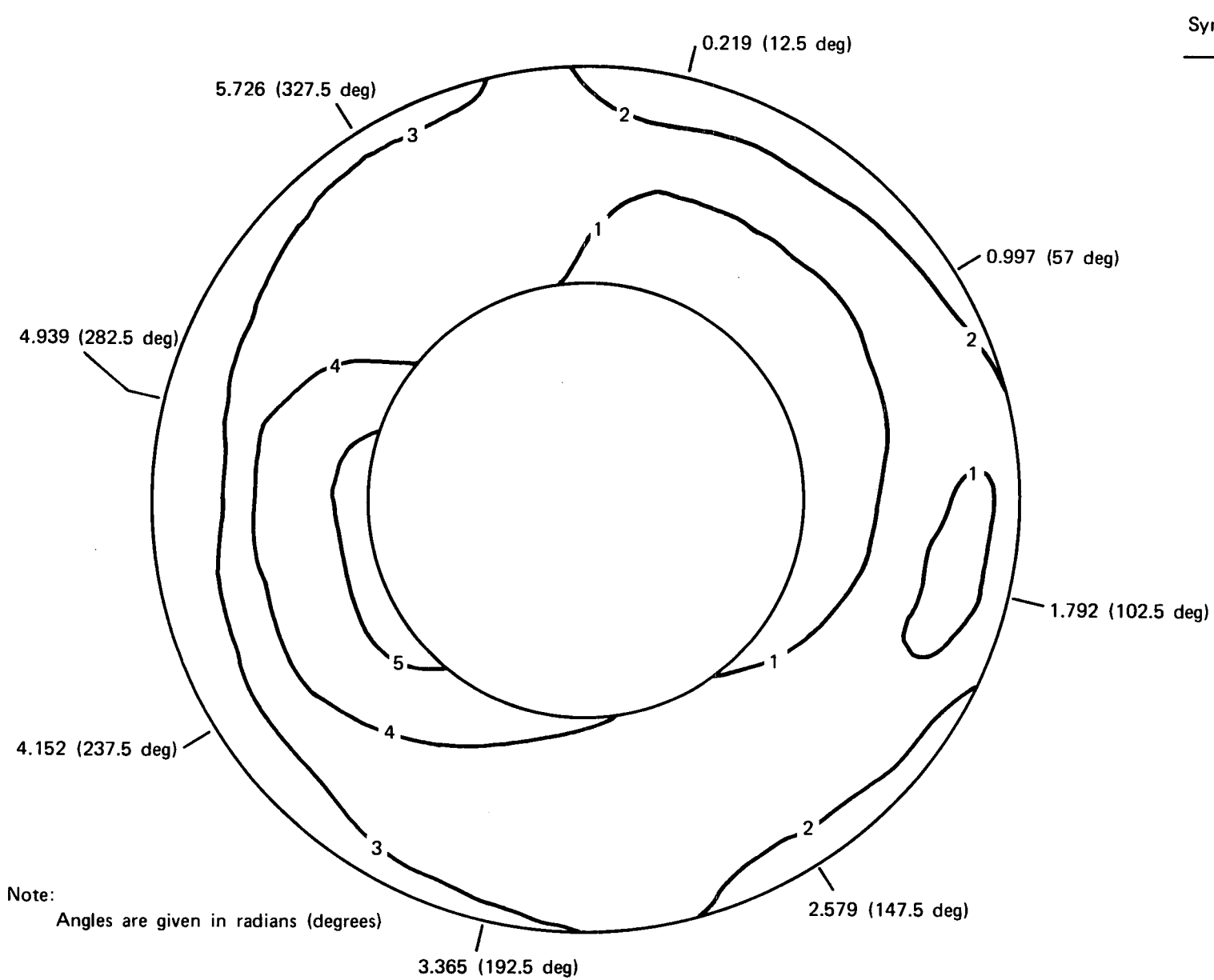

Symbol	$T_t/T_{t_{average}}$
1	0.66
2	0.68
3	1.3
4	1.35
5	1.38

Figure 56. F100/F401 High Compressor Inlet Temperature Map With Aerodynamic and Thermal Distortion, ΔT = 22 °K (40 °F); Build 205, Run 4453

FD 63401

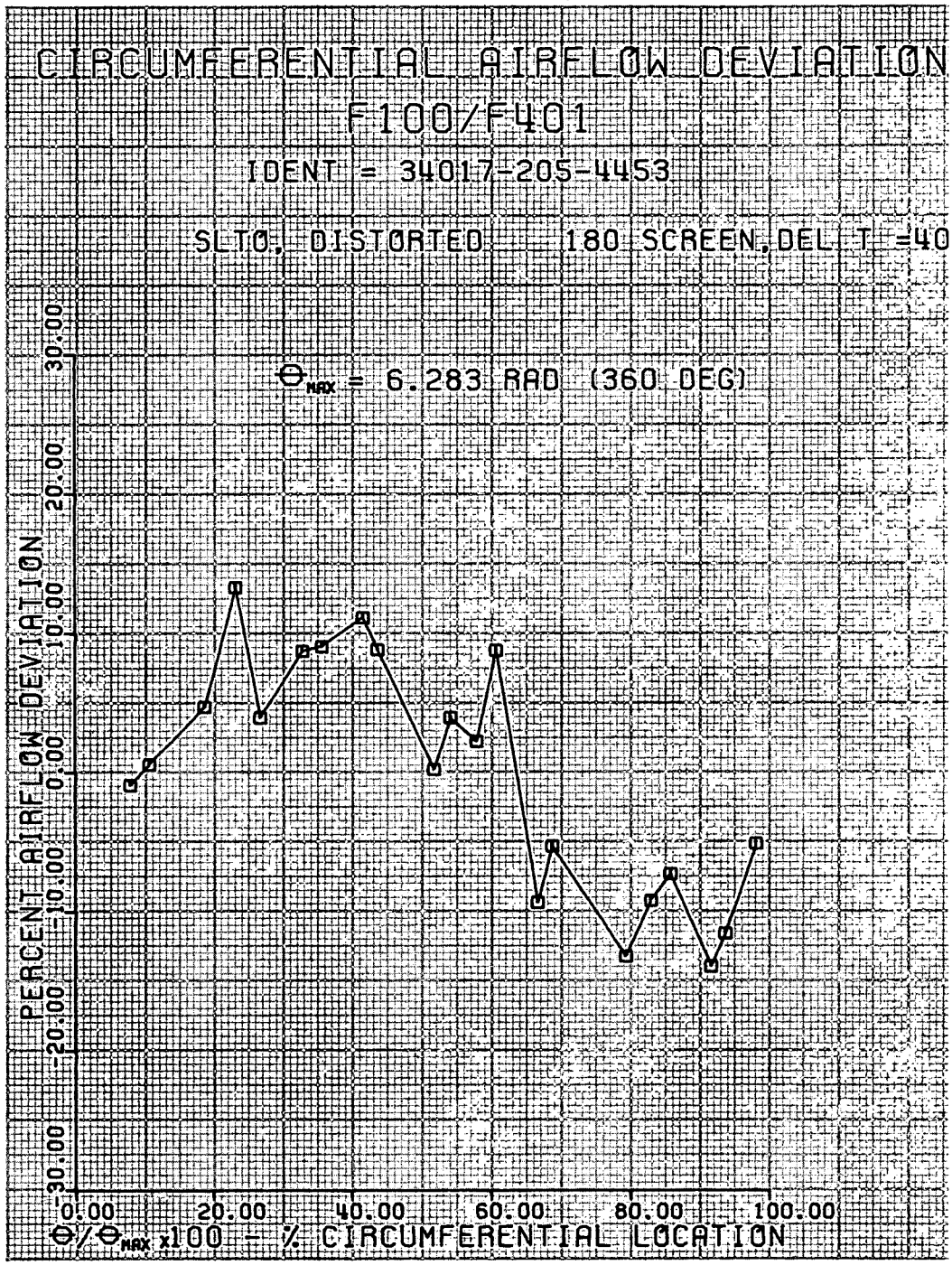

Figure 57.

DF 92101

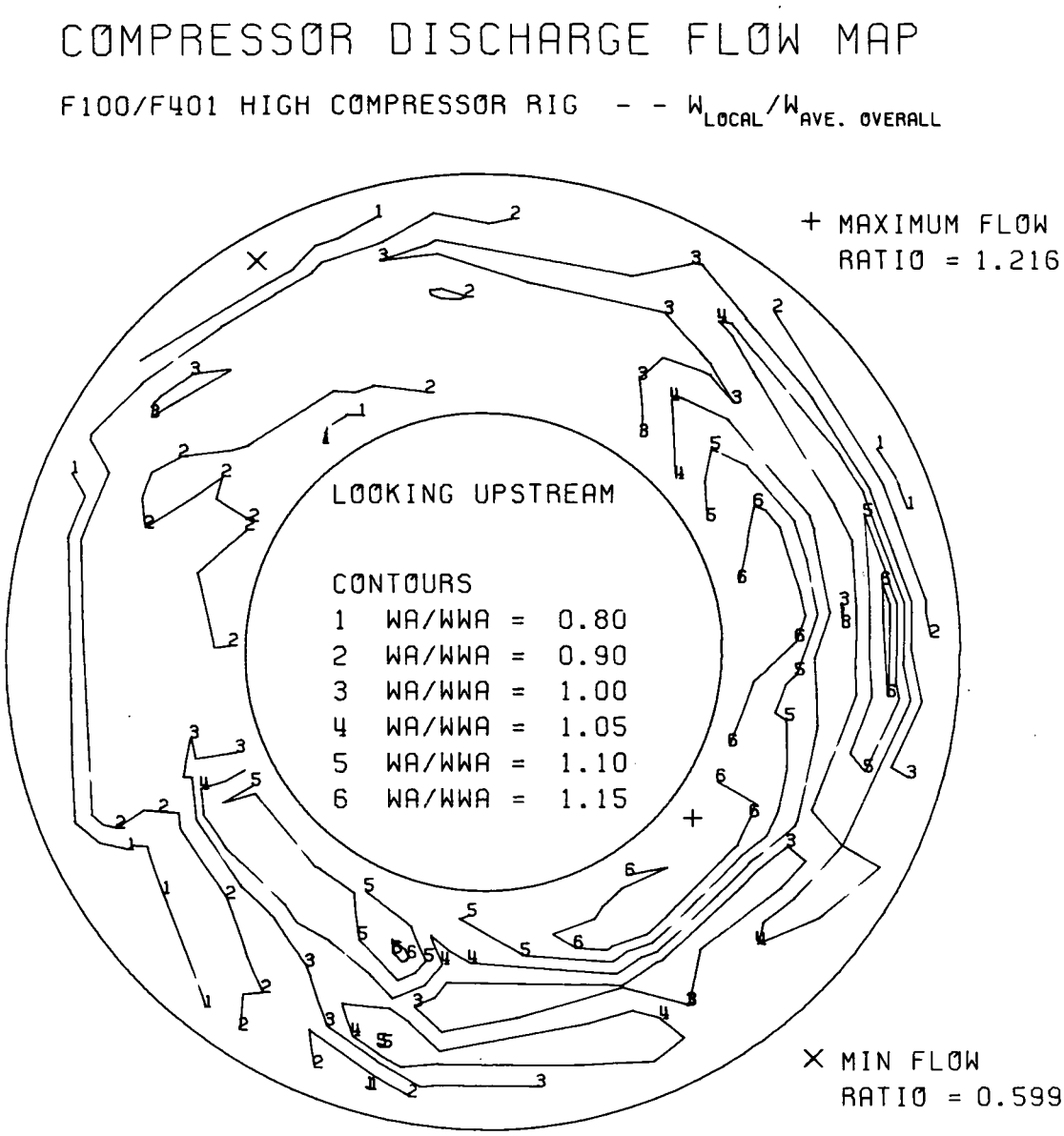

Figure 58.

DF 92081

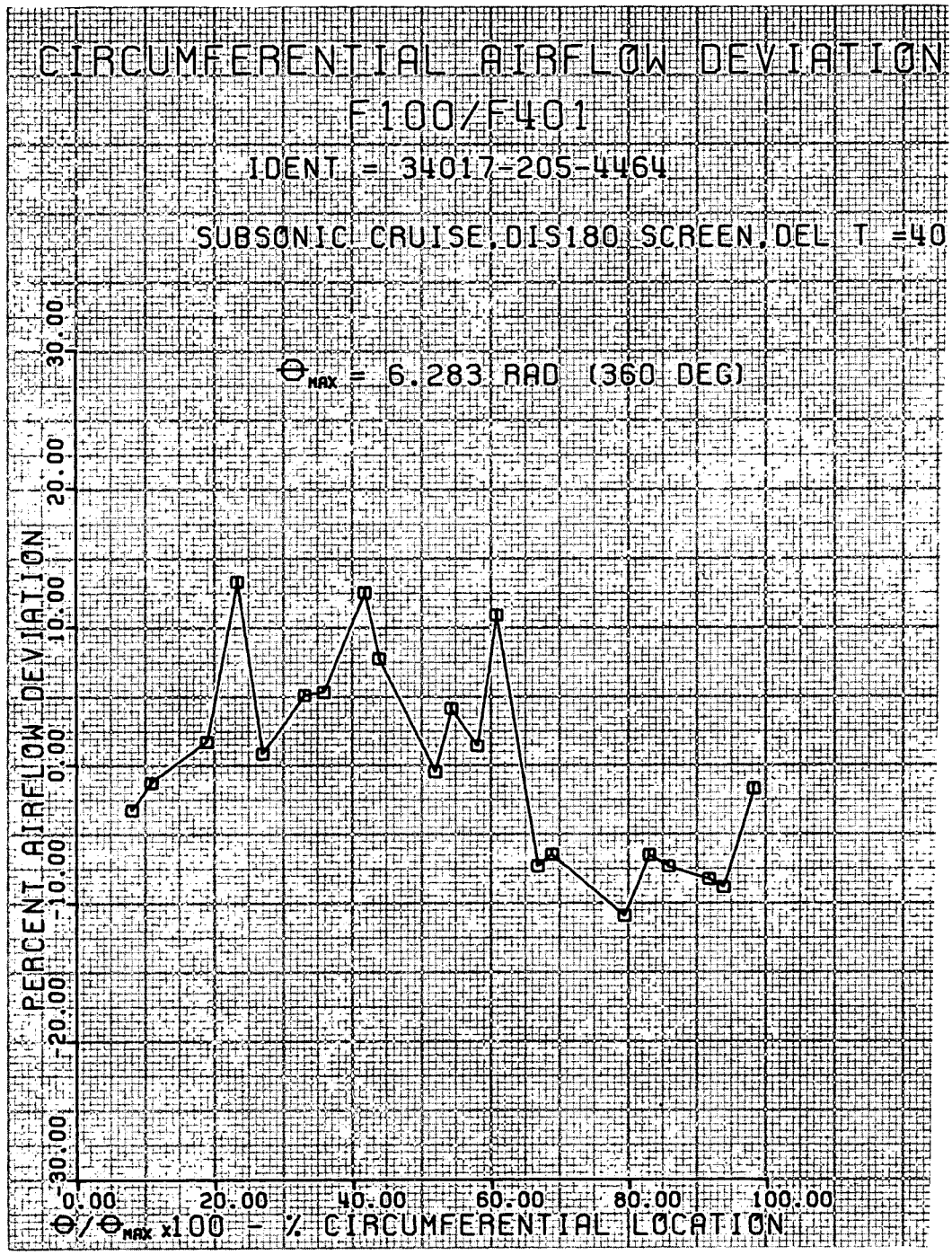

Figure 59.

DF 92100

COMPRESSOR DISCHARGE FLOW MAP

F100/F401 HIGH COMPRESSOR RIG - - $W_{LOCAL}/W_{AVE.\ OVERALL}$

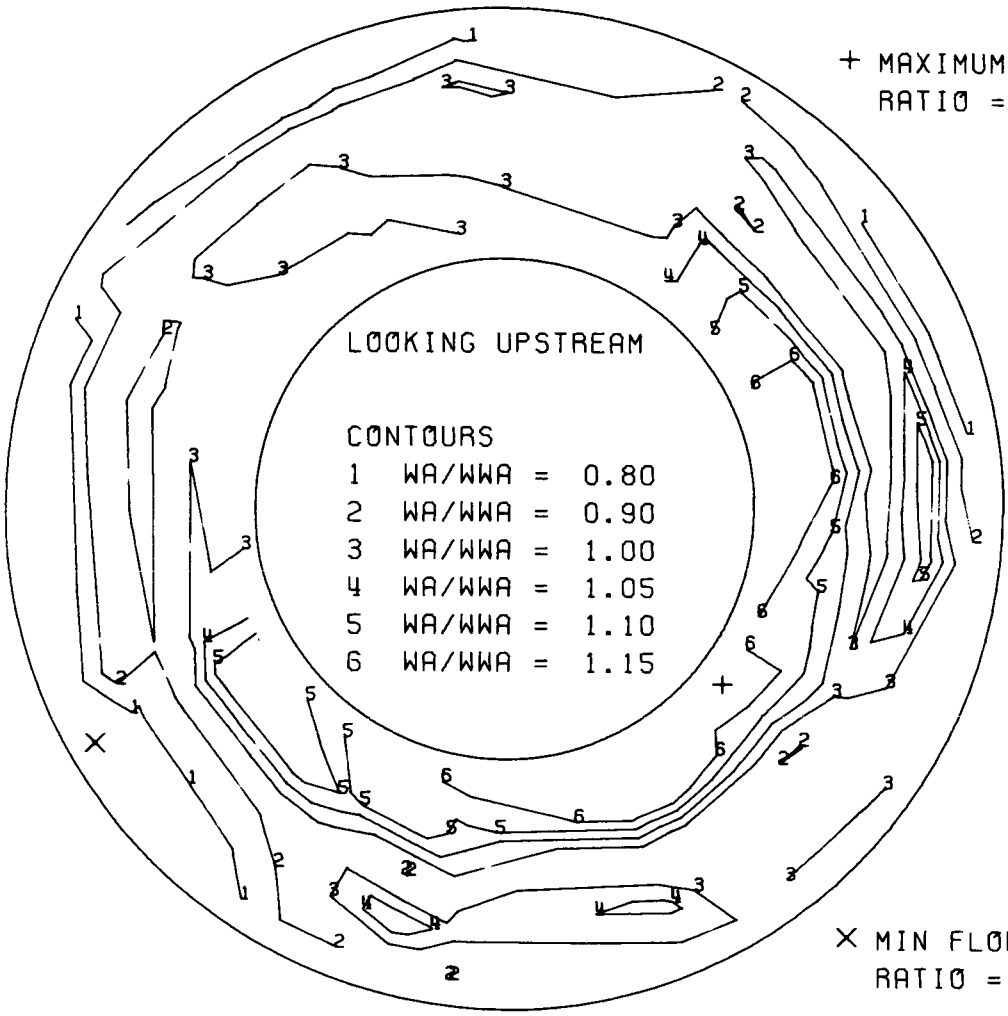

RIG NO.34017 BUILD NO.=205 RUN NO.=4464 CONDITION- SUBSONIC CRUISE,DIS

DF 92082

Figure 60.

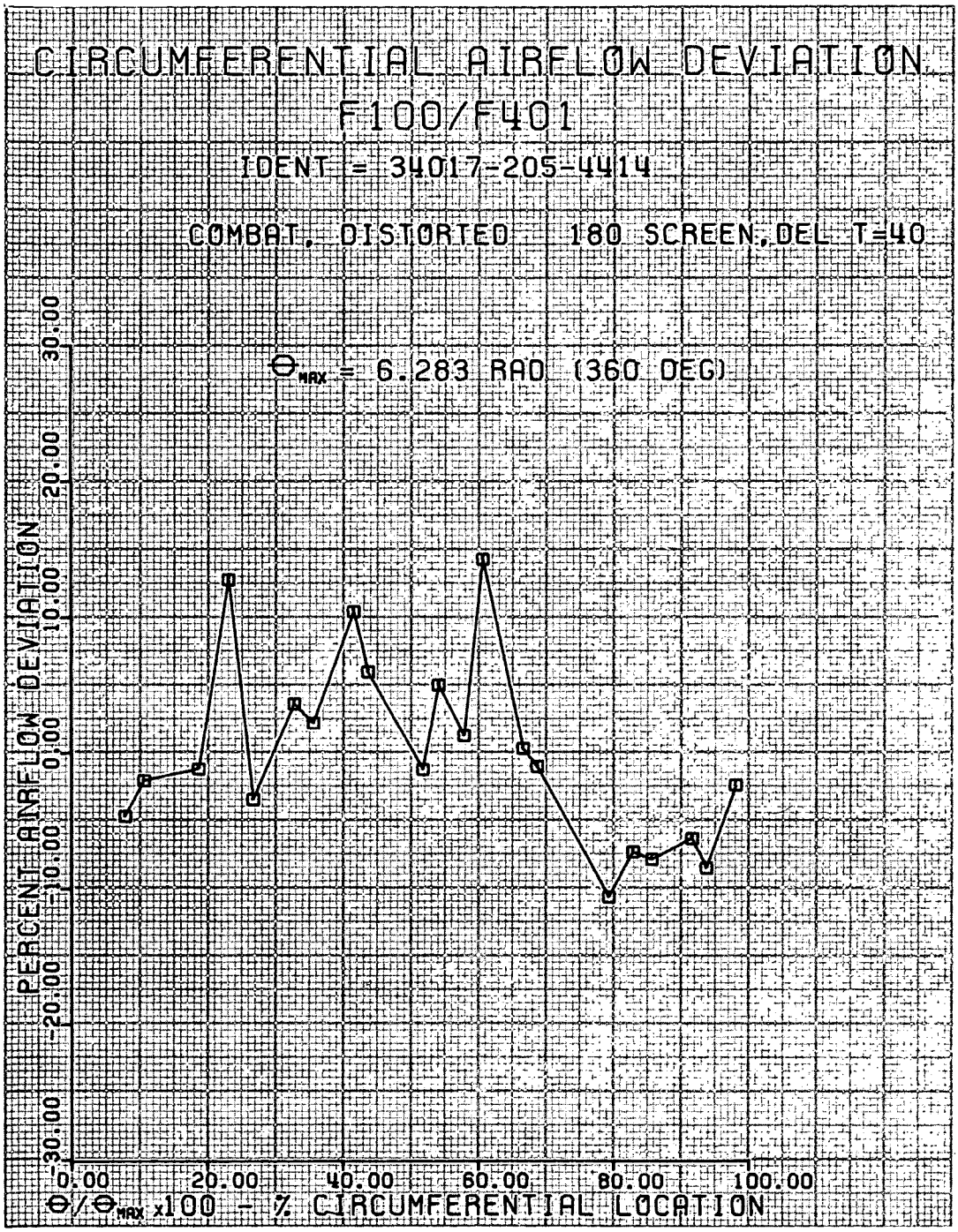

Figure 61.

DF 92102

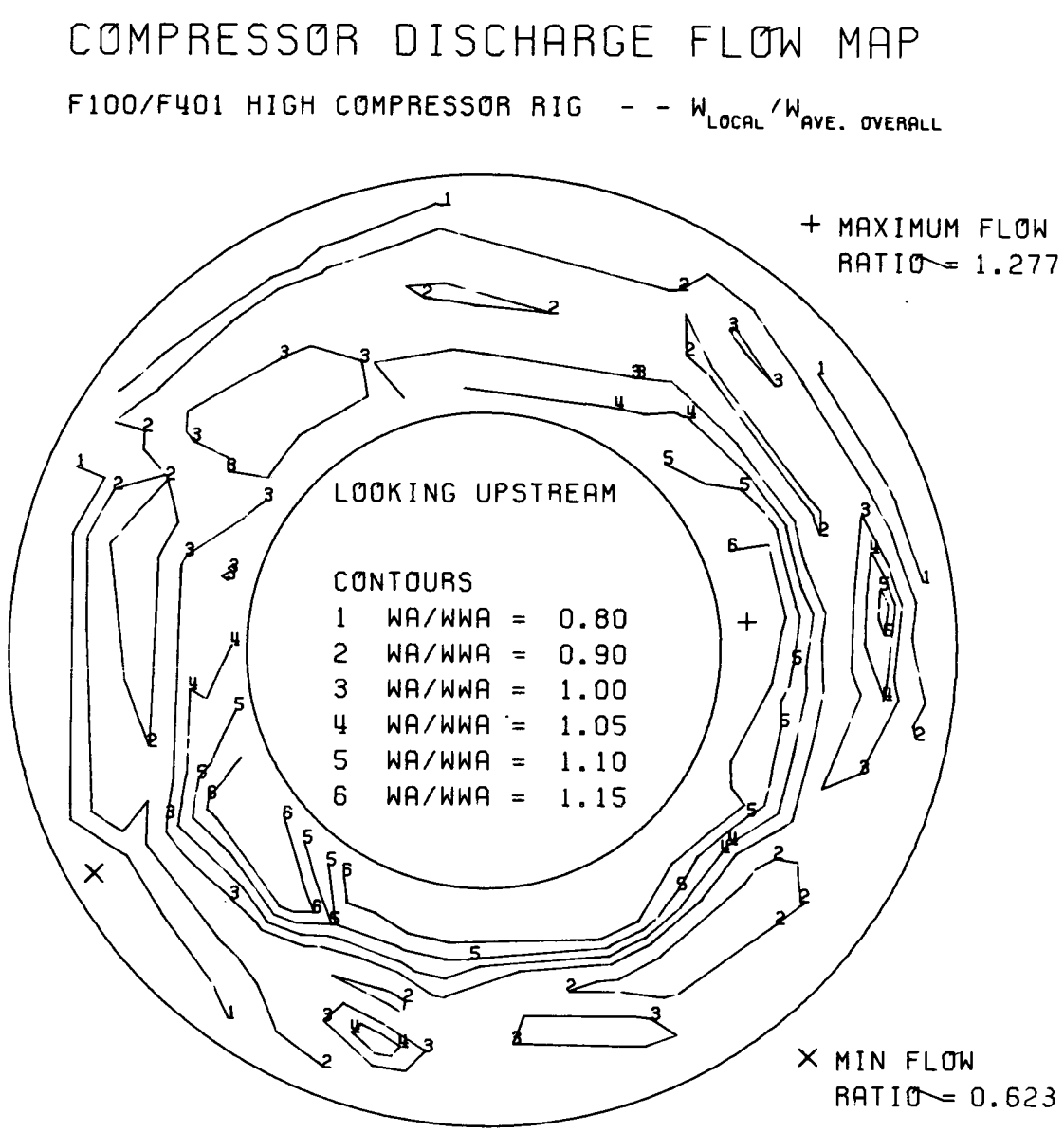

Figure 62.

DF 92083

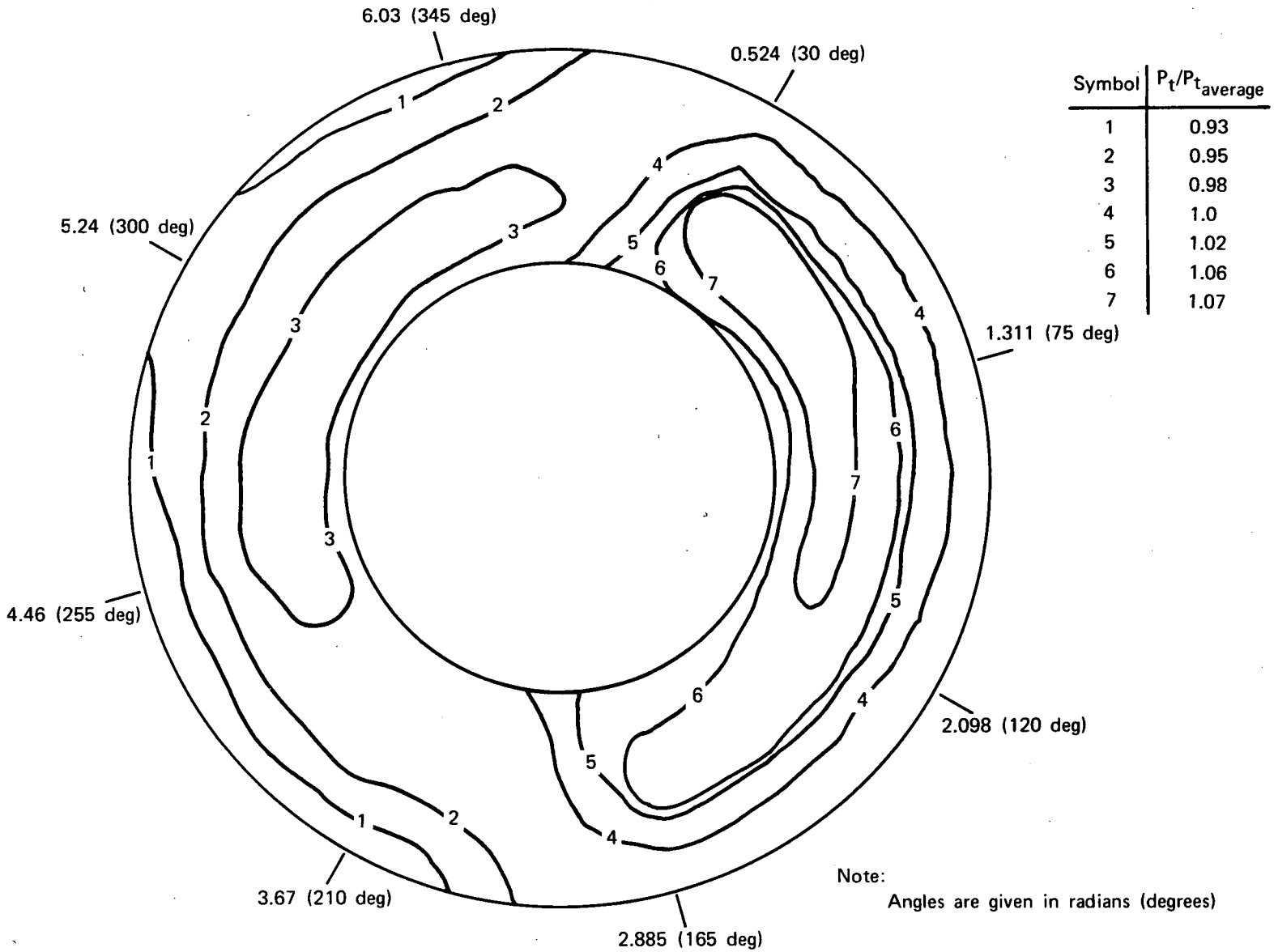

Figure 63. F100/F401 High Compressor Inlet Pressure Map With Aerodynamic and Thermal Distortion, $\Delta T = 55\,°K$ (100 °F); Build 205, Run 5313

FD 63403

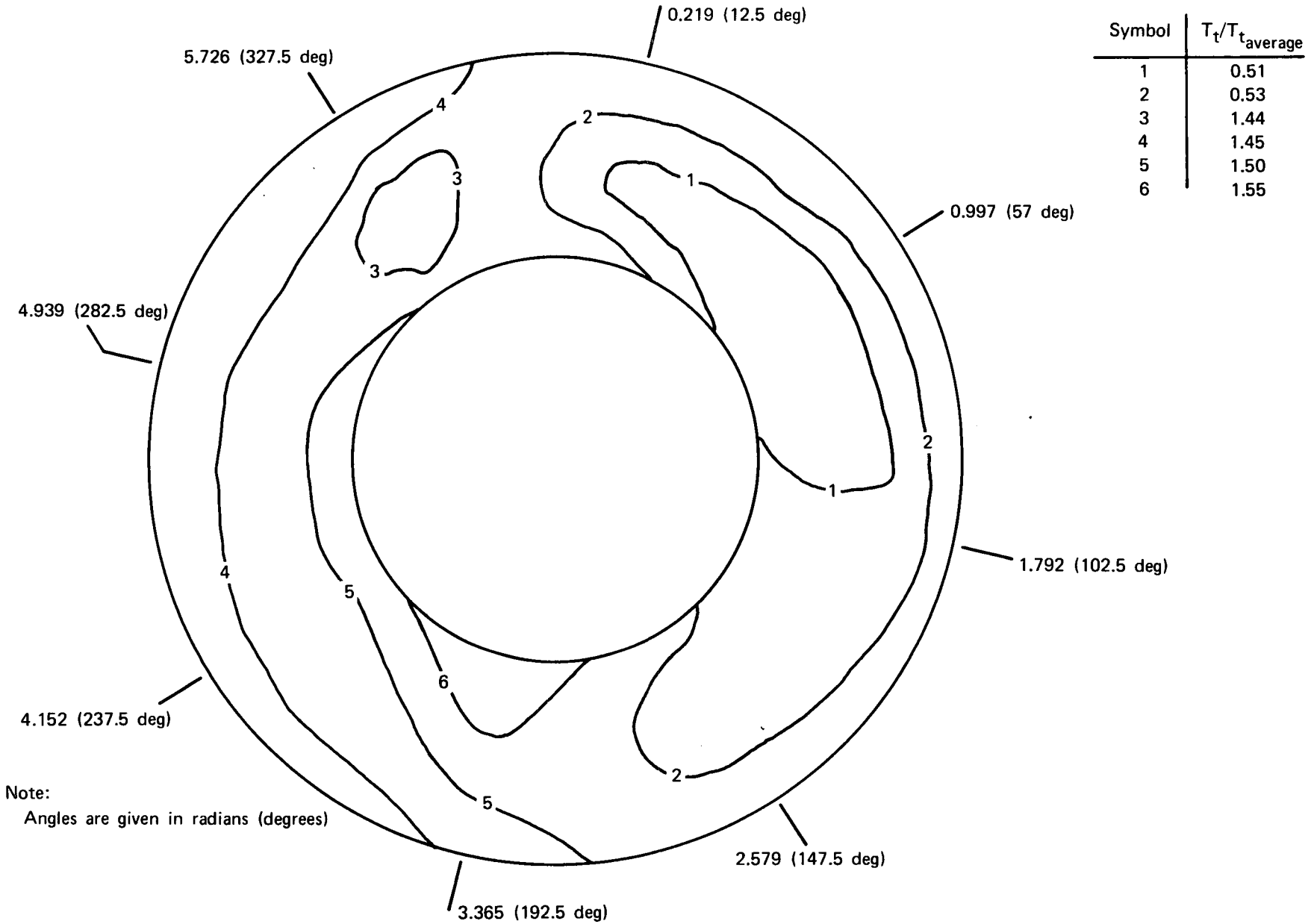

Figure 64. F100/F401 High Compressor Inlet Temperature Map With Aerodynamic and Thermal Distortion, $\Delta T = 55\,°K$ (100 °F); Build 205, Run 5313

FD 63406

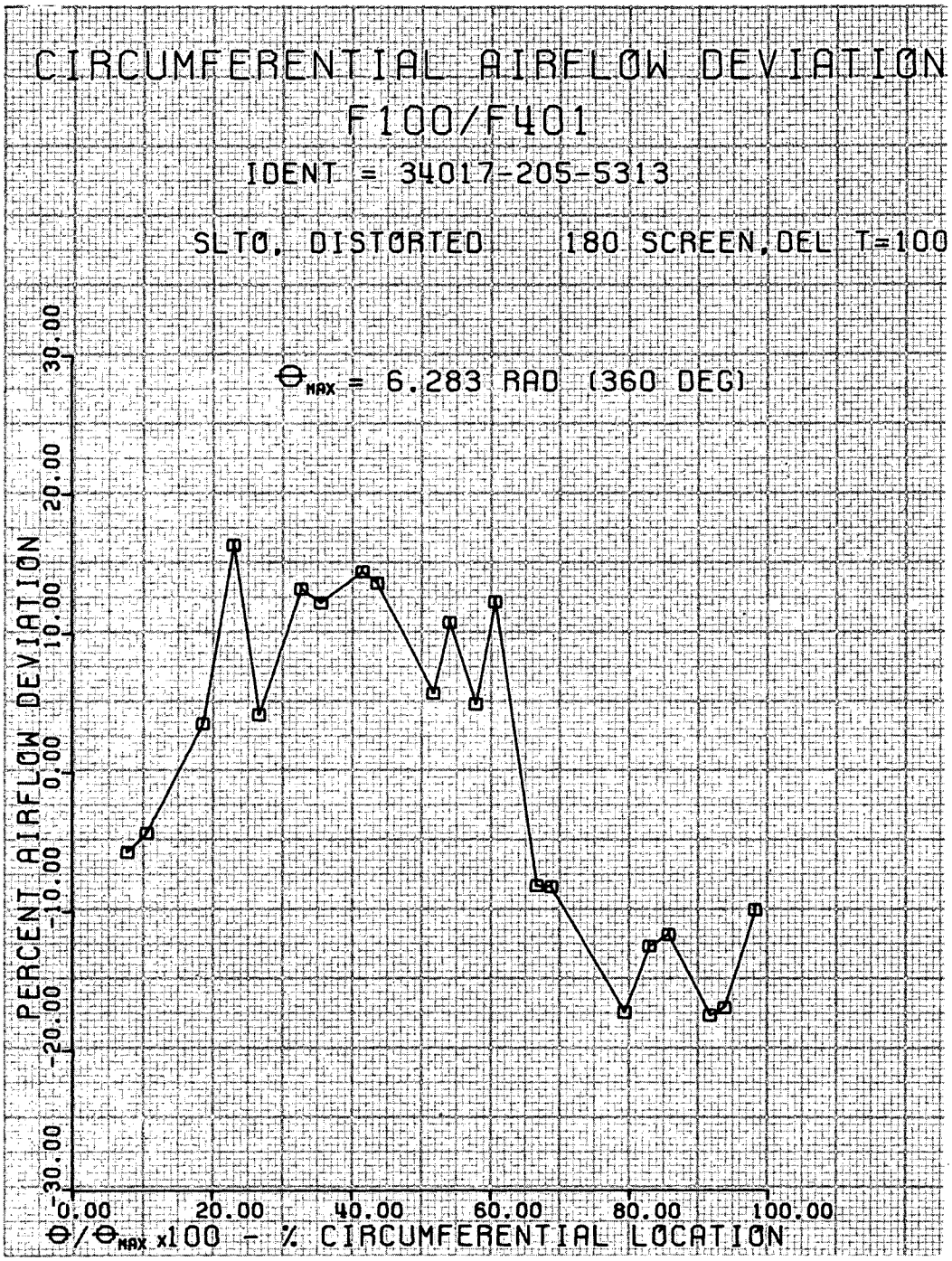

Figure 65.

DF 92103

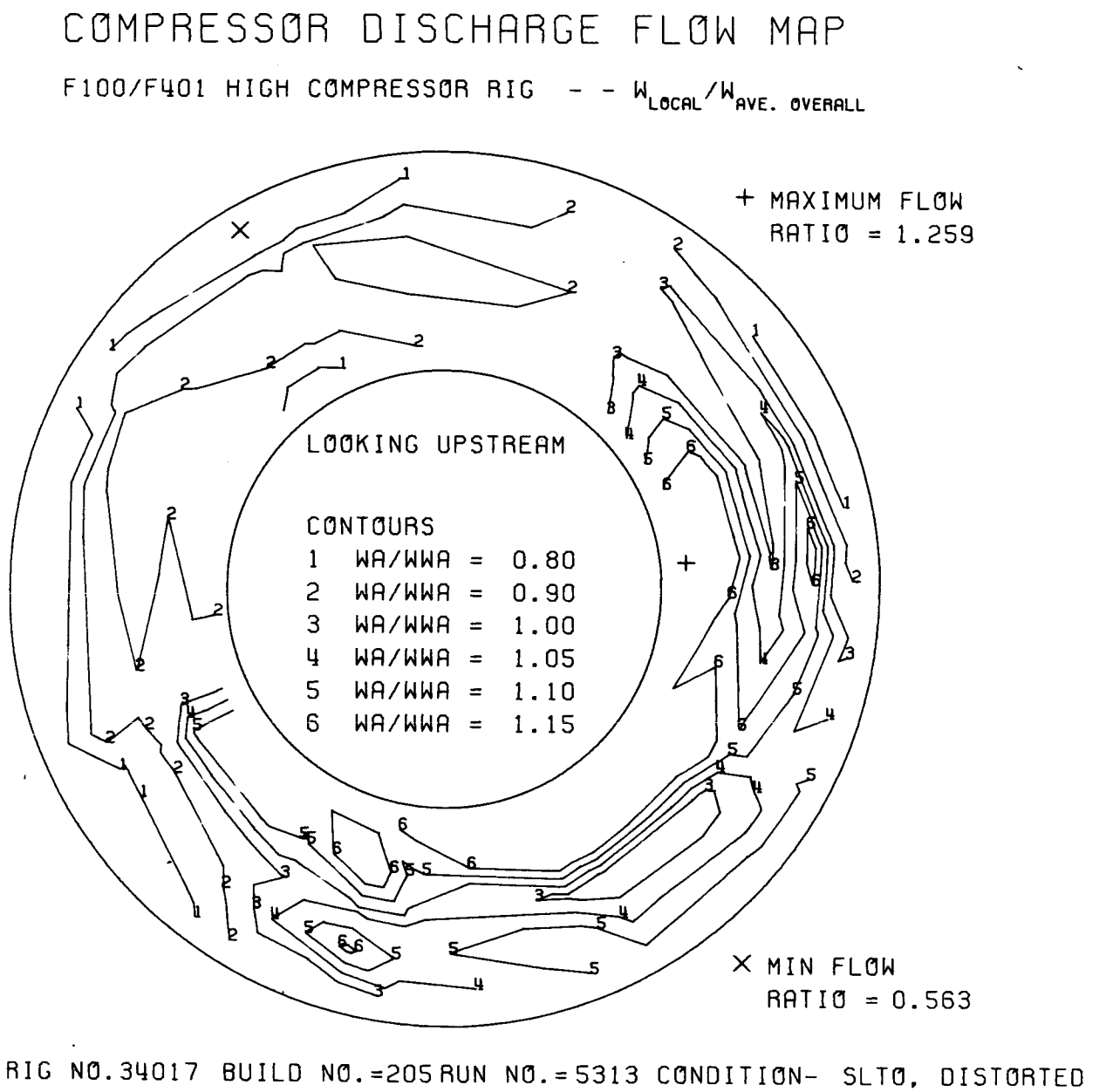

Figure 66.

DF 92084

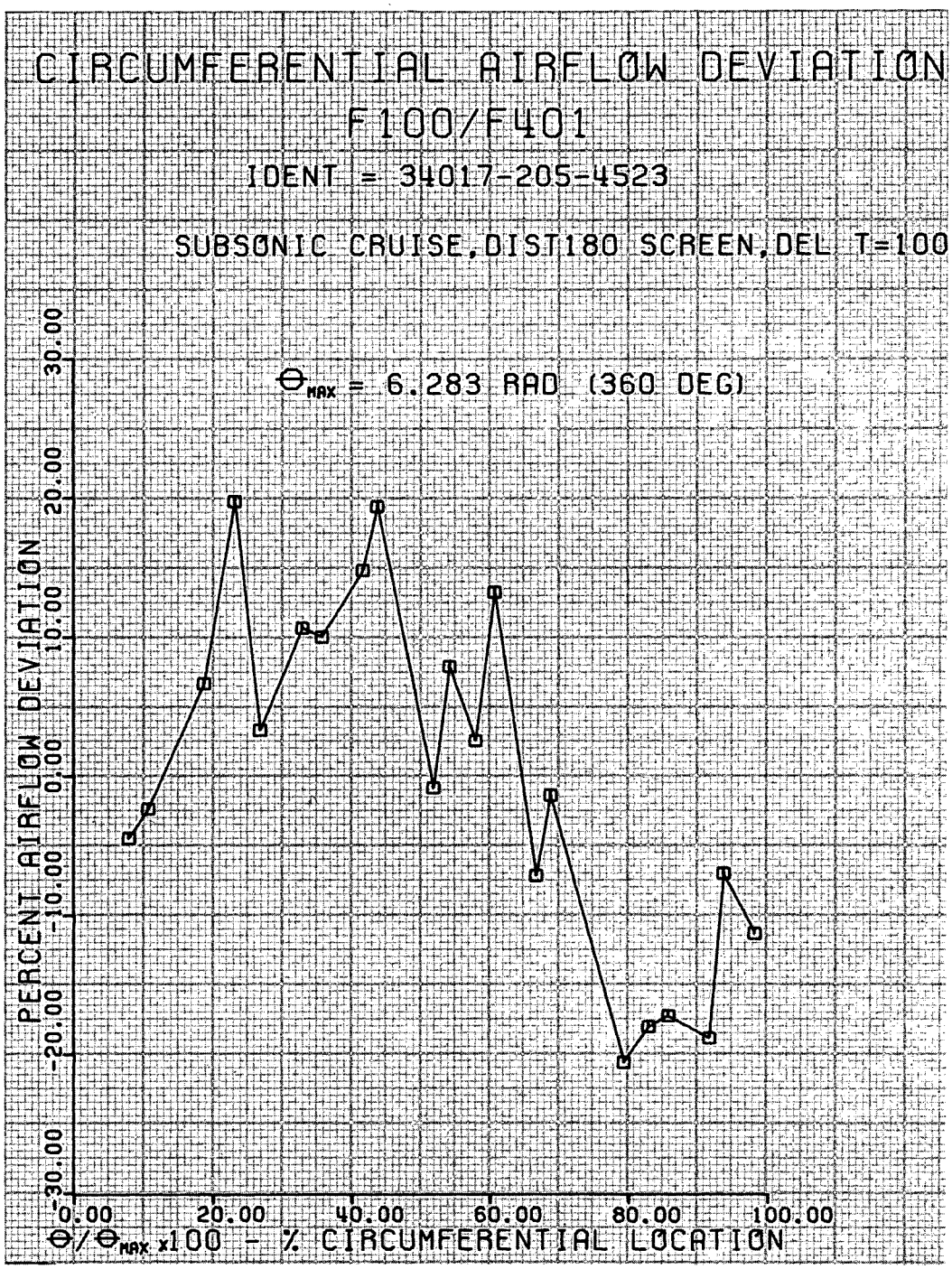

Figure 67.

DF 92104

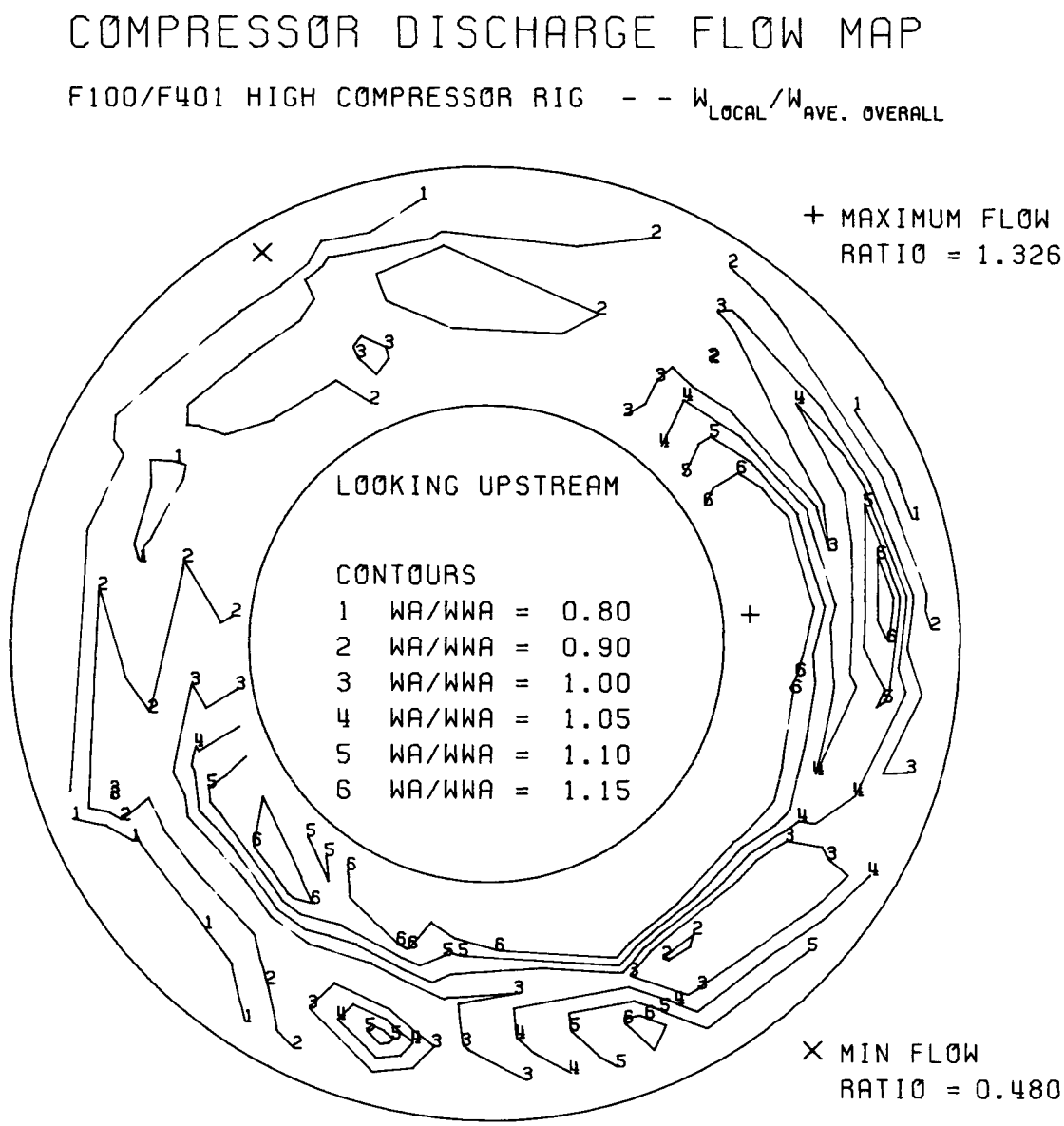

Figure 68.

DF 92085

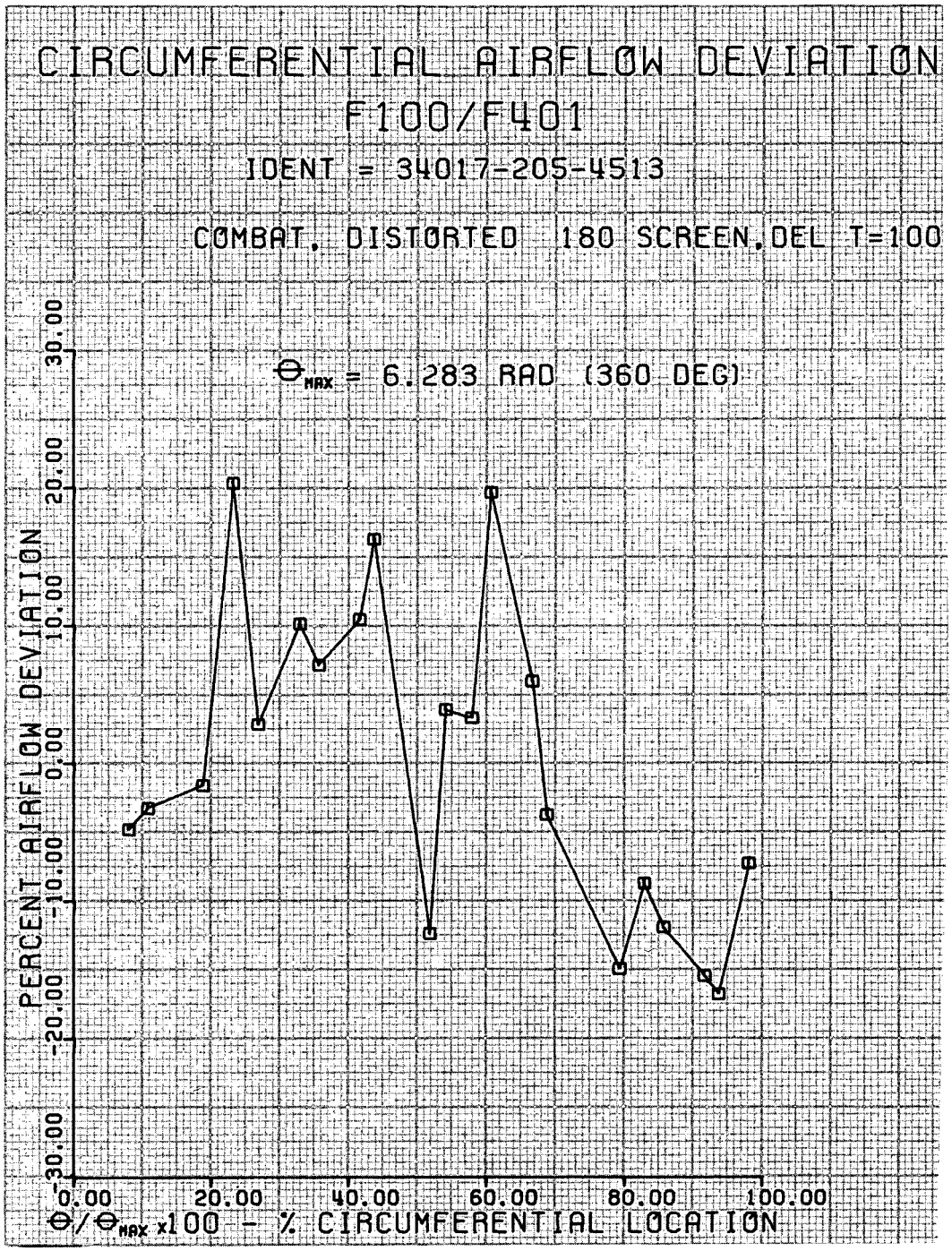

Figure 69.

DF 92105

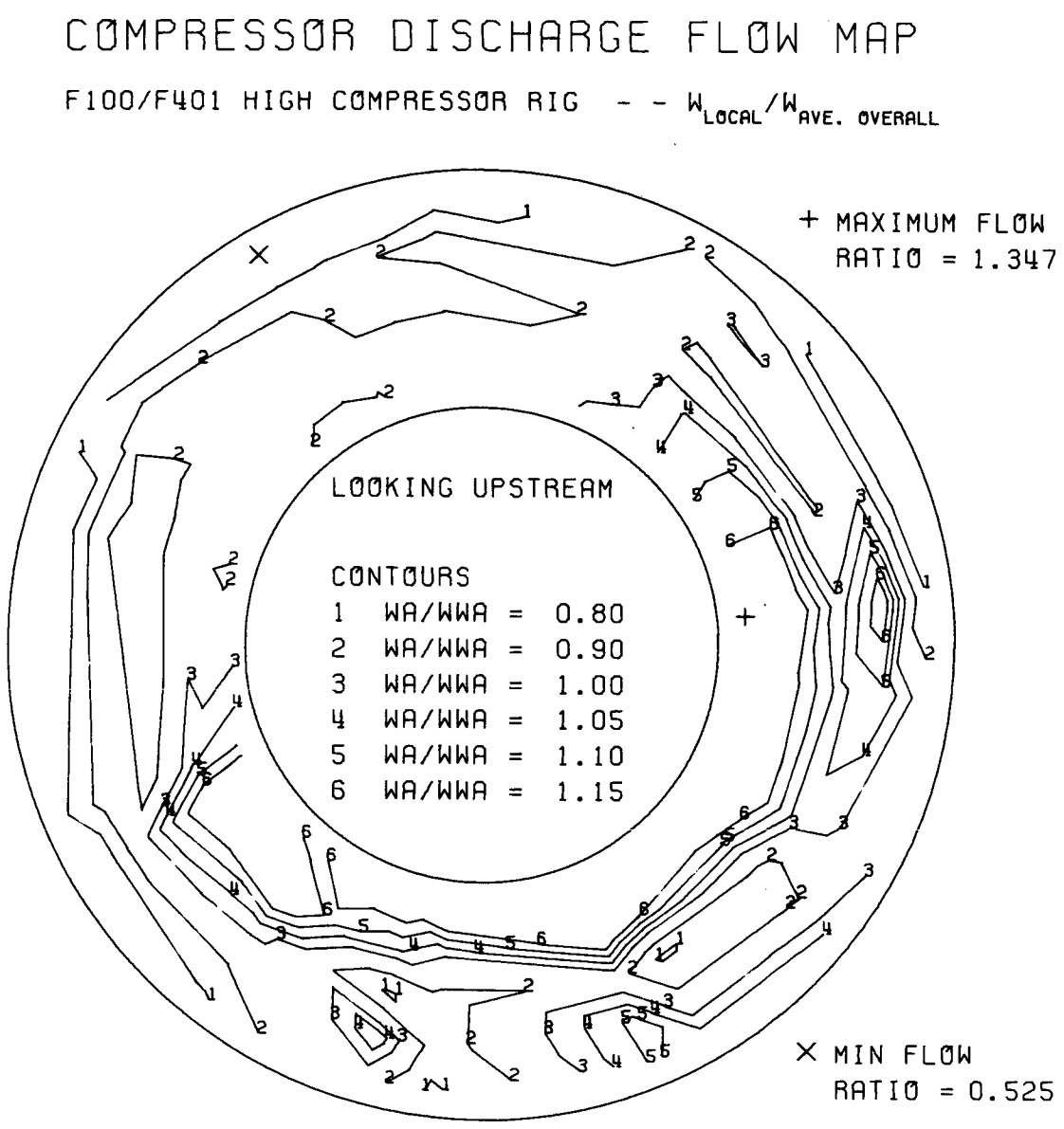

Figure 70.

DF 92086

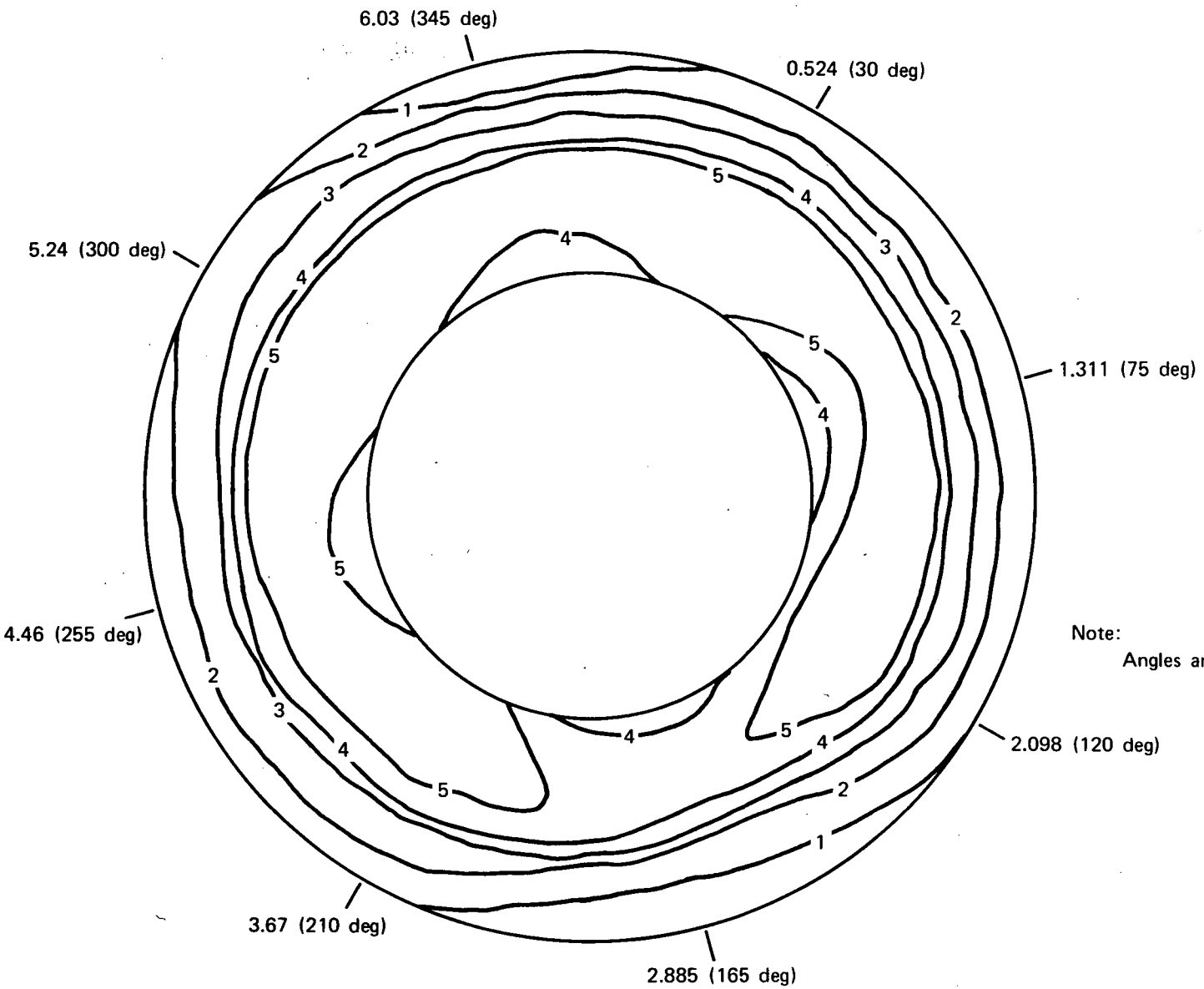

Symbol	$P_t/P_{t_{average}}$
1	0.94
2	0.96
3	0.98
4	1.0
5	1.02

Note:
Angles are given in radians (degrees)

Figure 71. F100/F401 High Compressor Inlet Pressure Map With Thermal Distortion, $\Delta T = 22\,°K$ (40 °F); Build 205, Run 4653

FD 63404

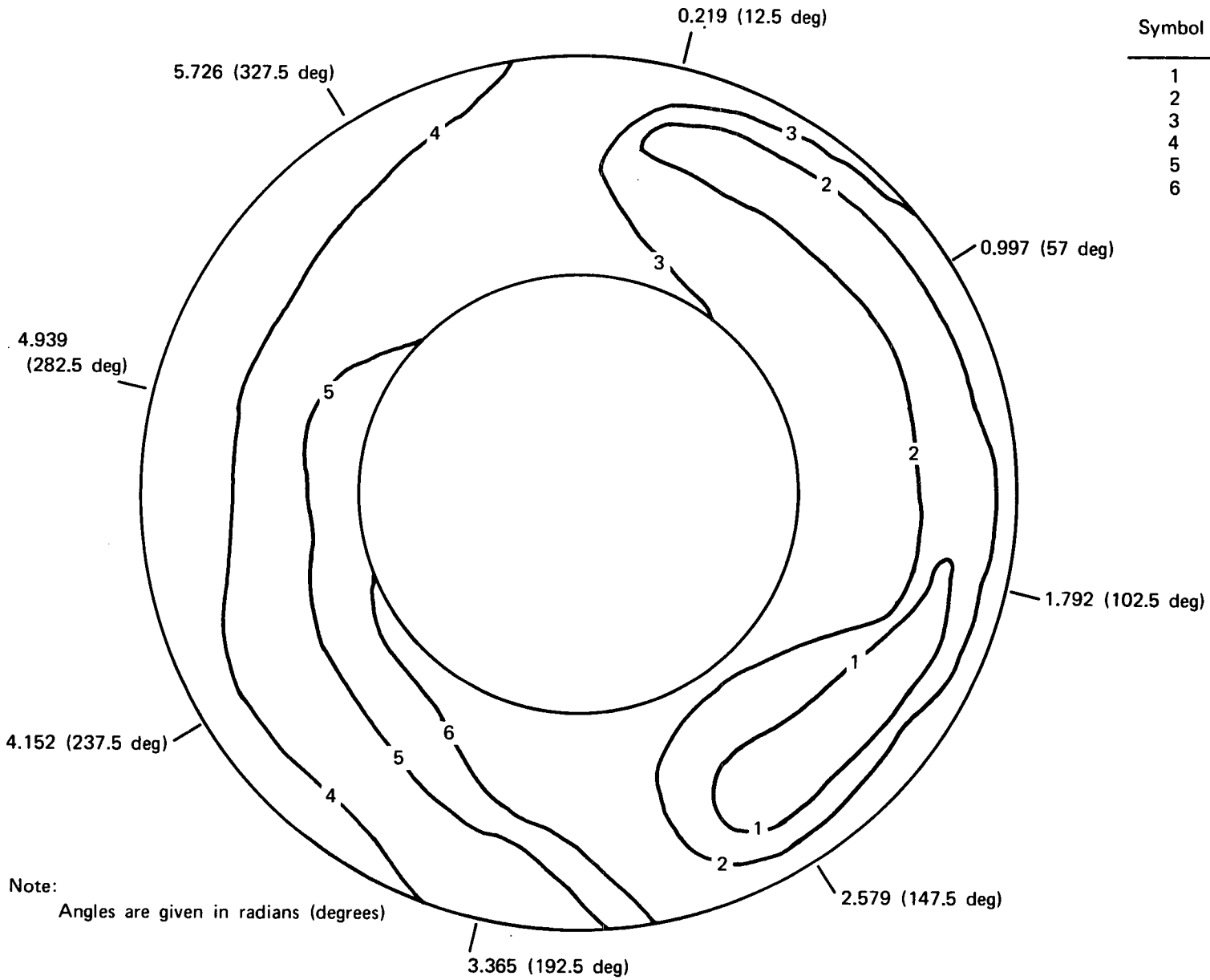

Symbol	$T_t/T_{t_{average}}$
1	0.785
2	0.79
3	0.795
4	1.20
5	1.22
6	1.24

Figure 72. F100/F401 High Compressor Inlet Temperature Map With Thermal Distortion, $\Delta T = 22\,°K$ (40 °F); Build 205, Run 4653

FD 63407

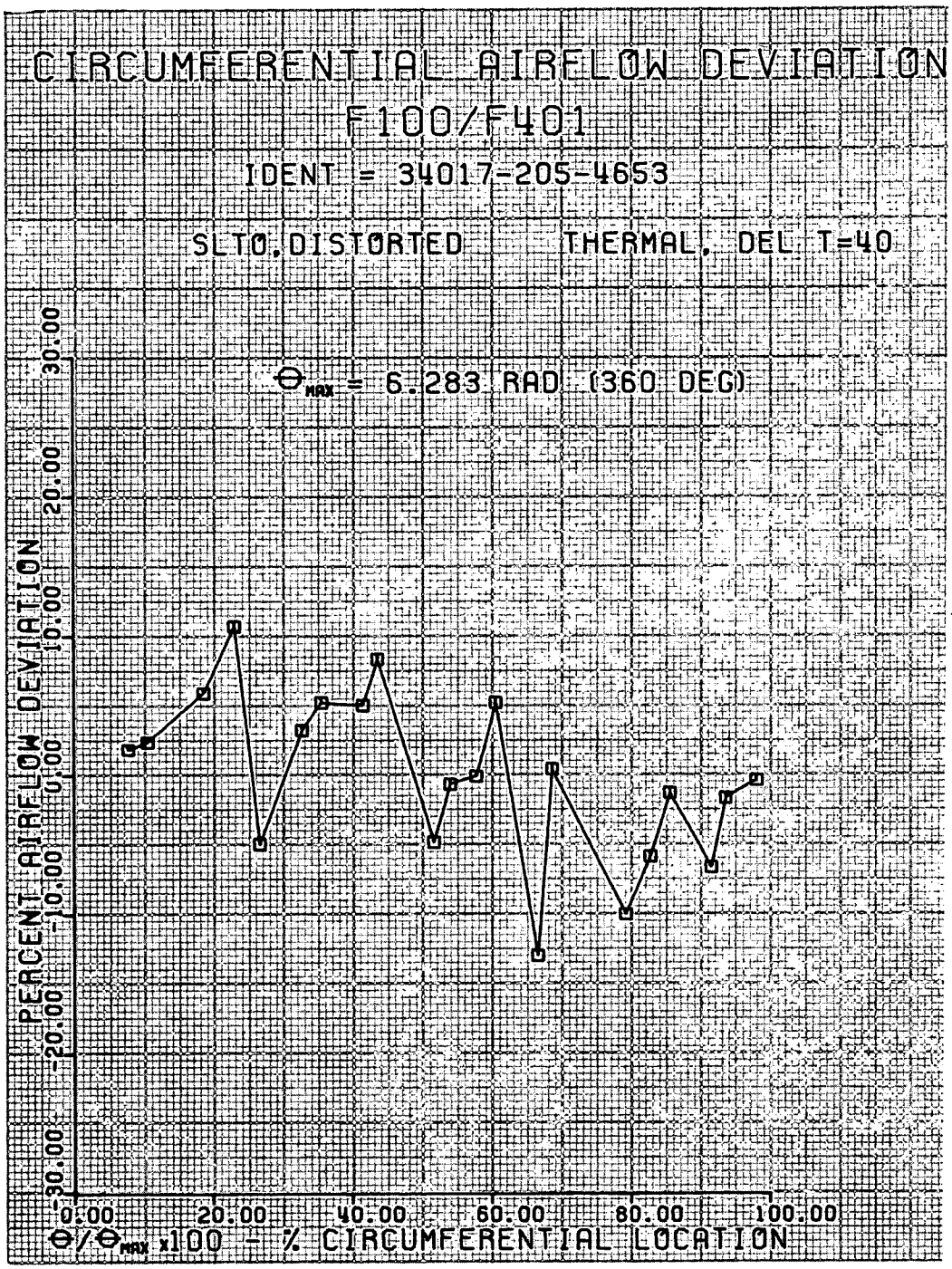

Figure 73.

DF 92106

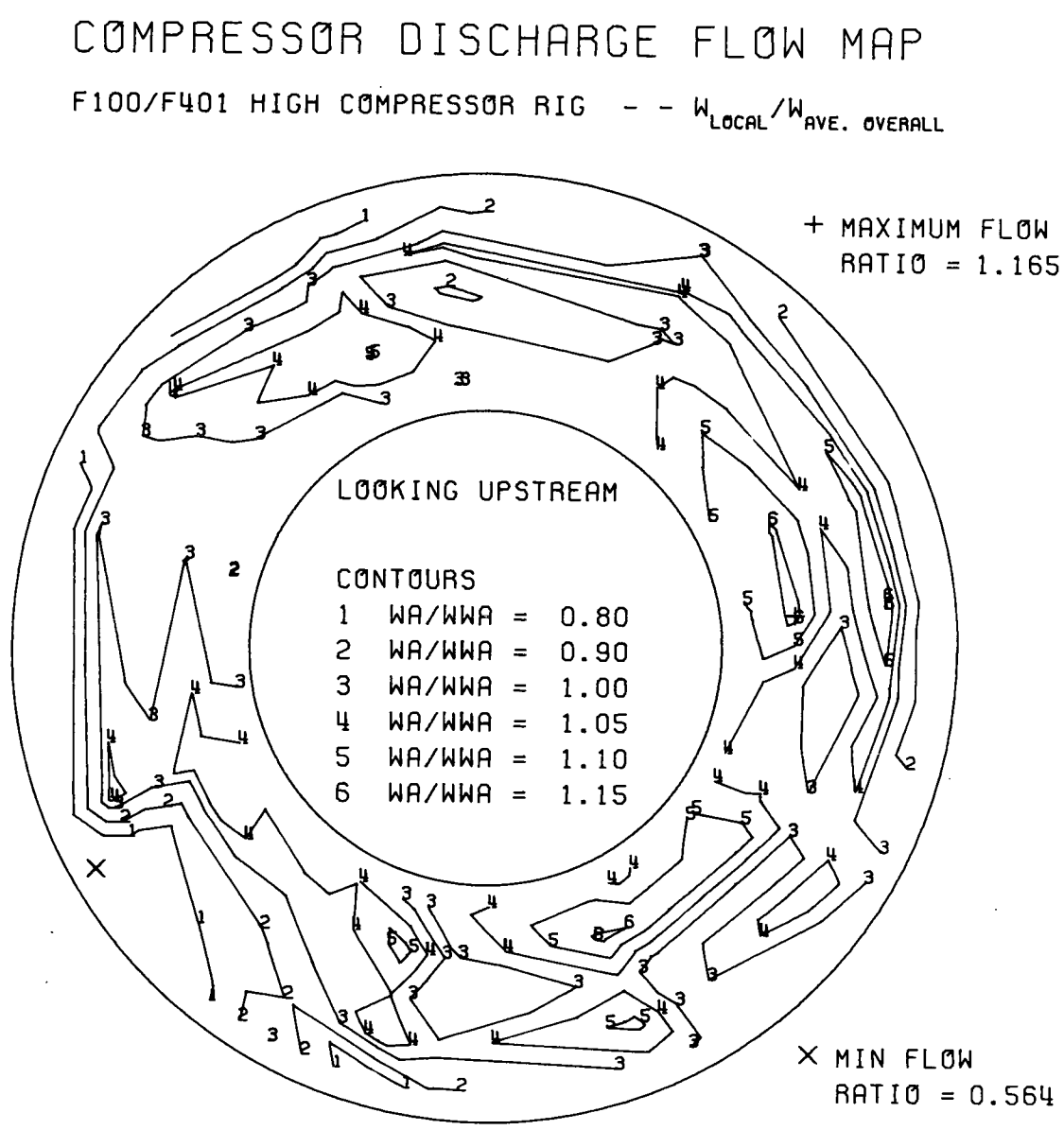

Figure 74.

DF 92087

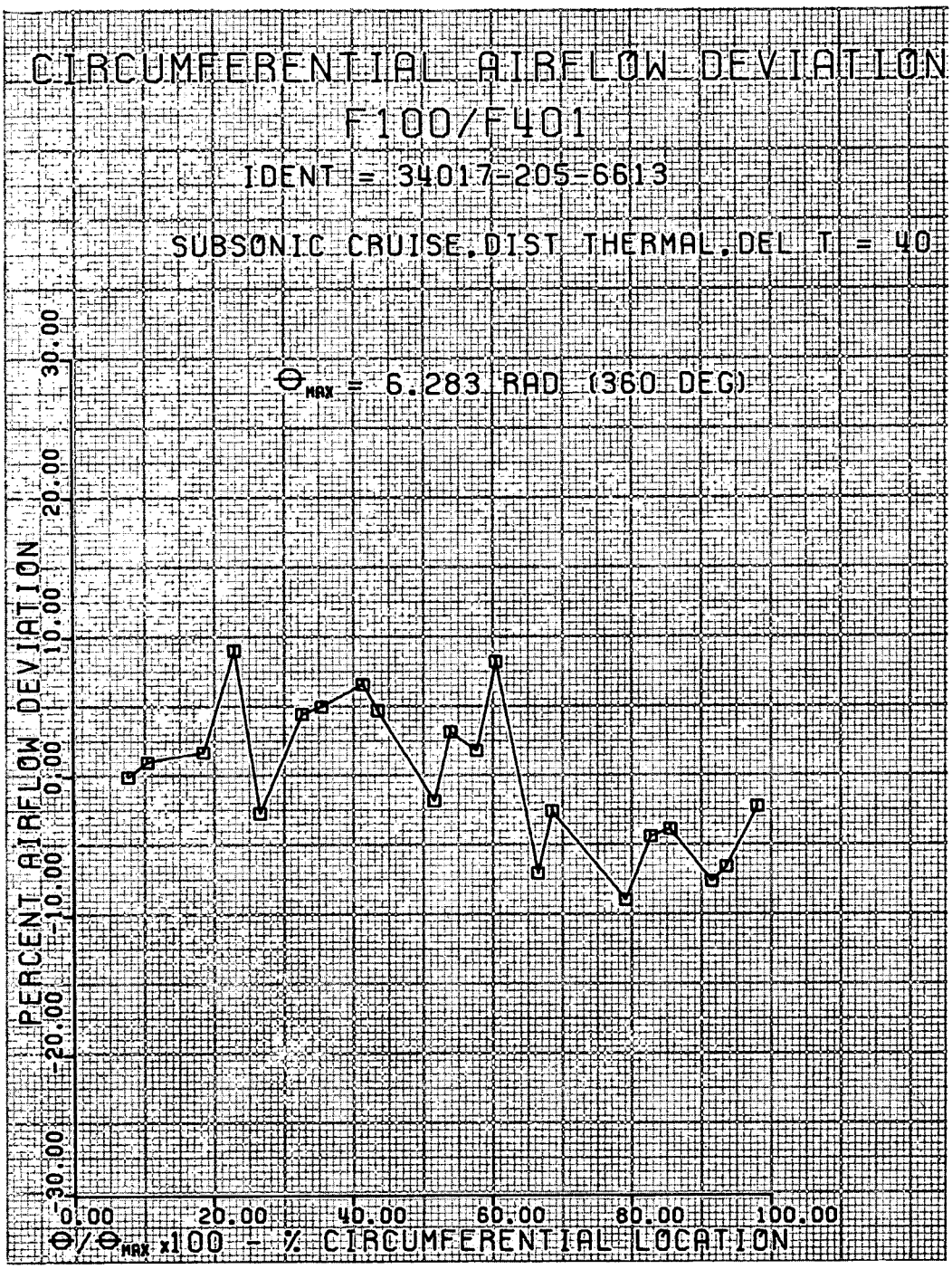

Figure 75.

DF 92107

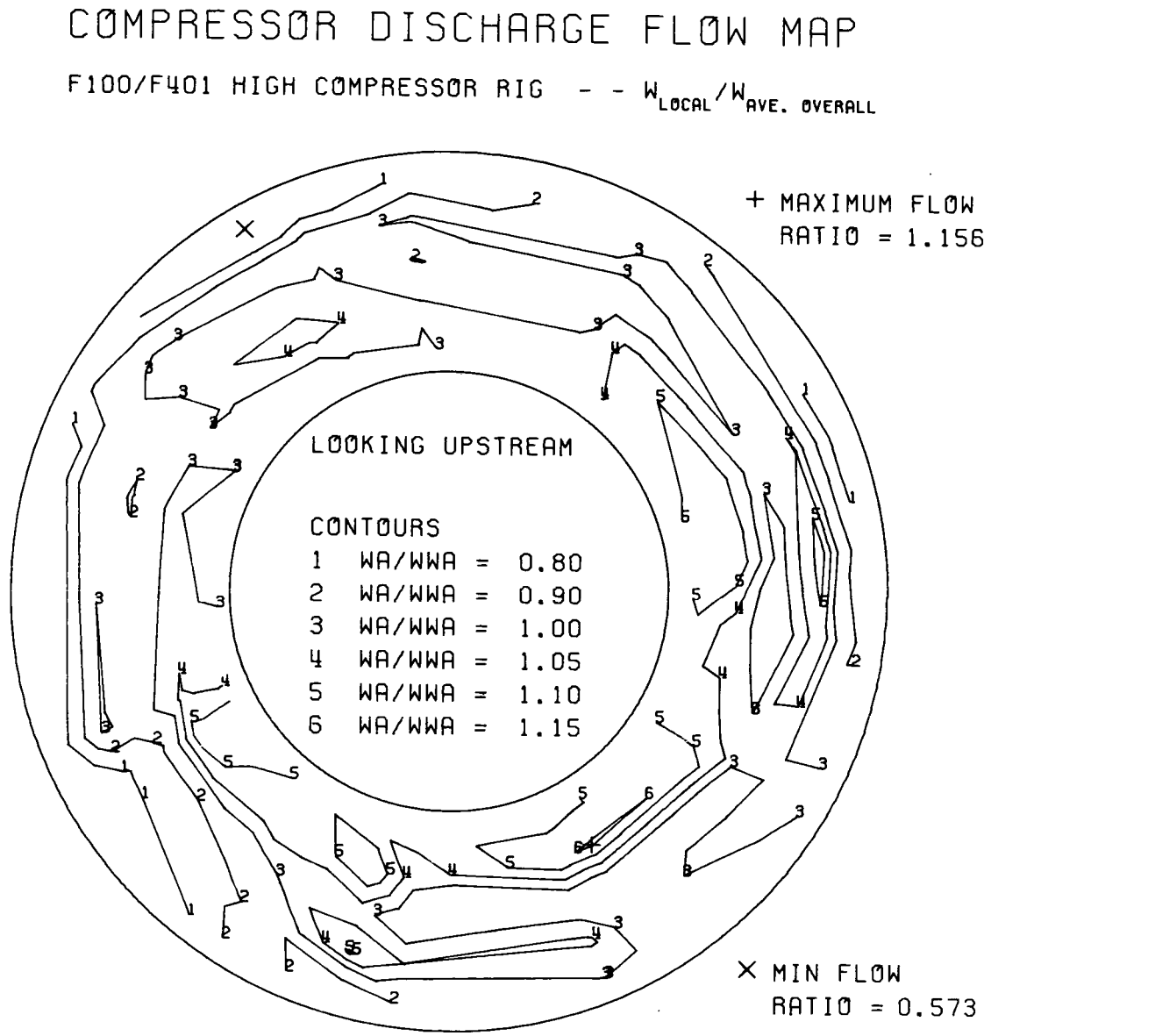

Figure 76.

DF 92088

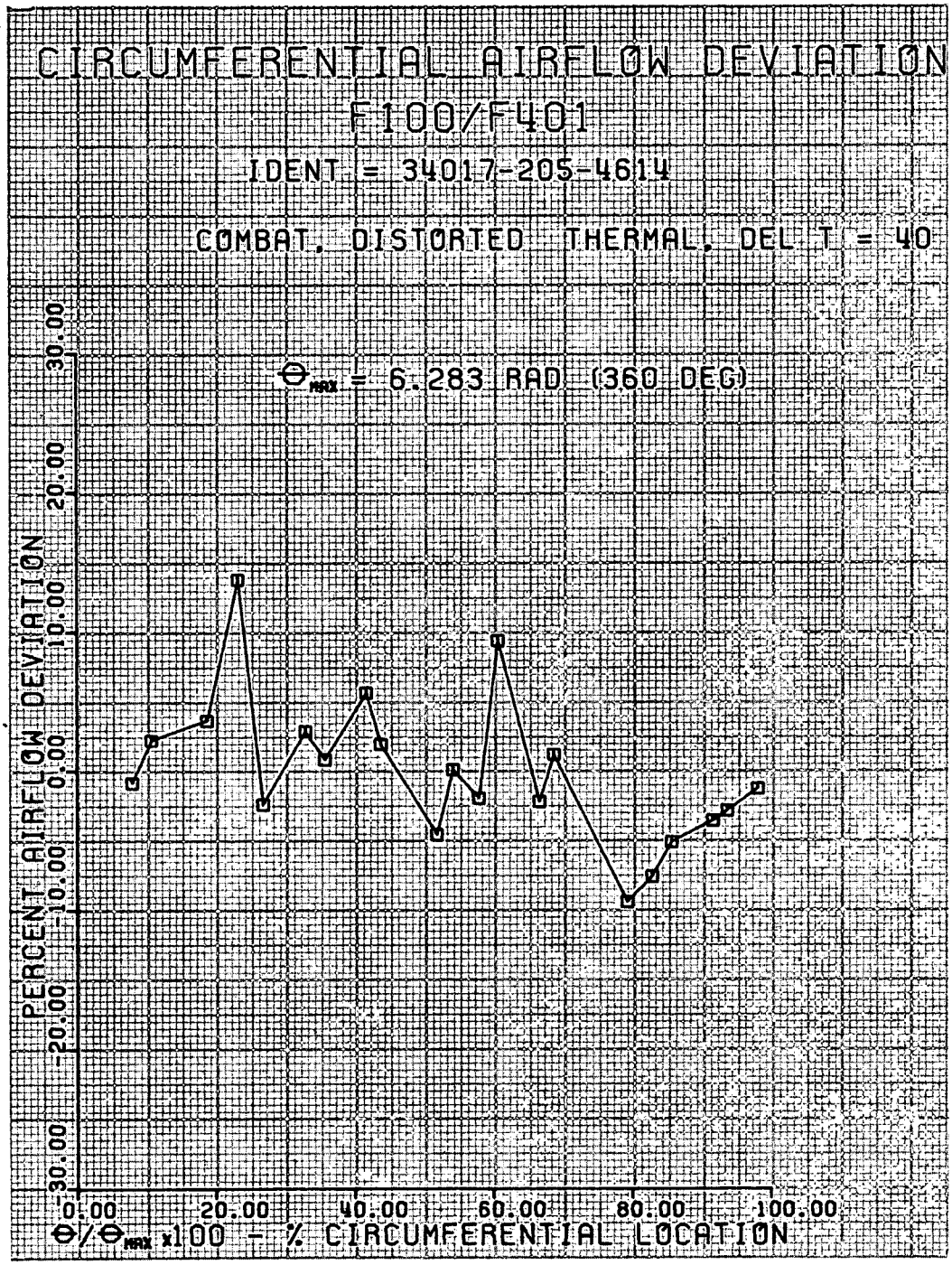

Figure 77.

DF 92108

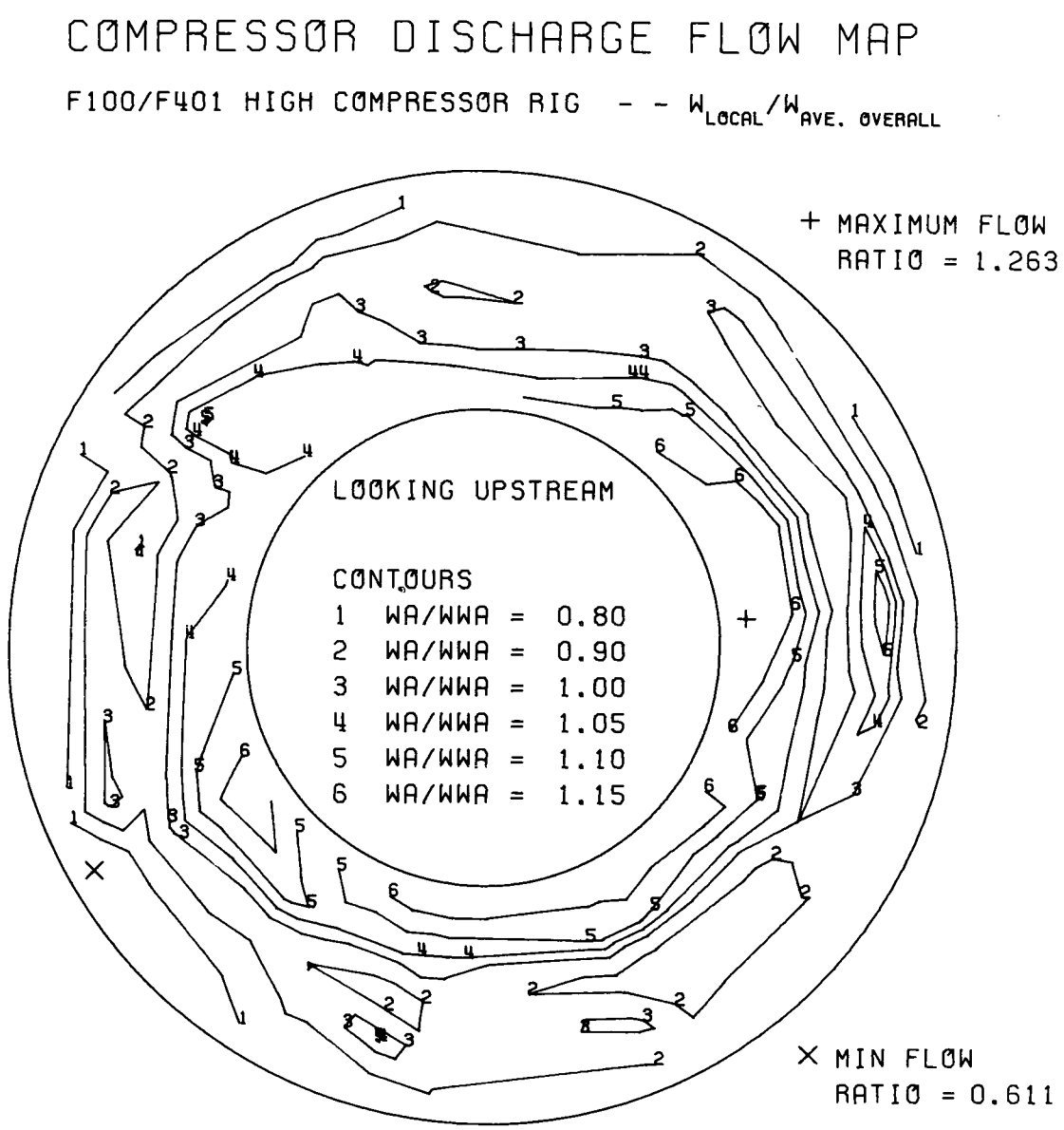

Figure 78.

DF 92089

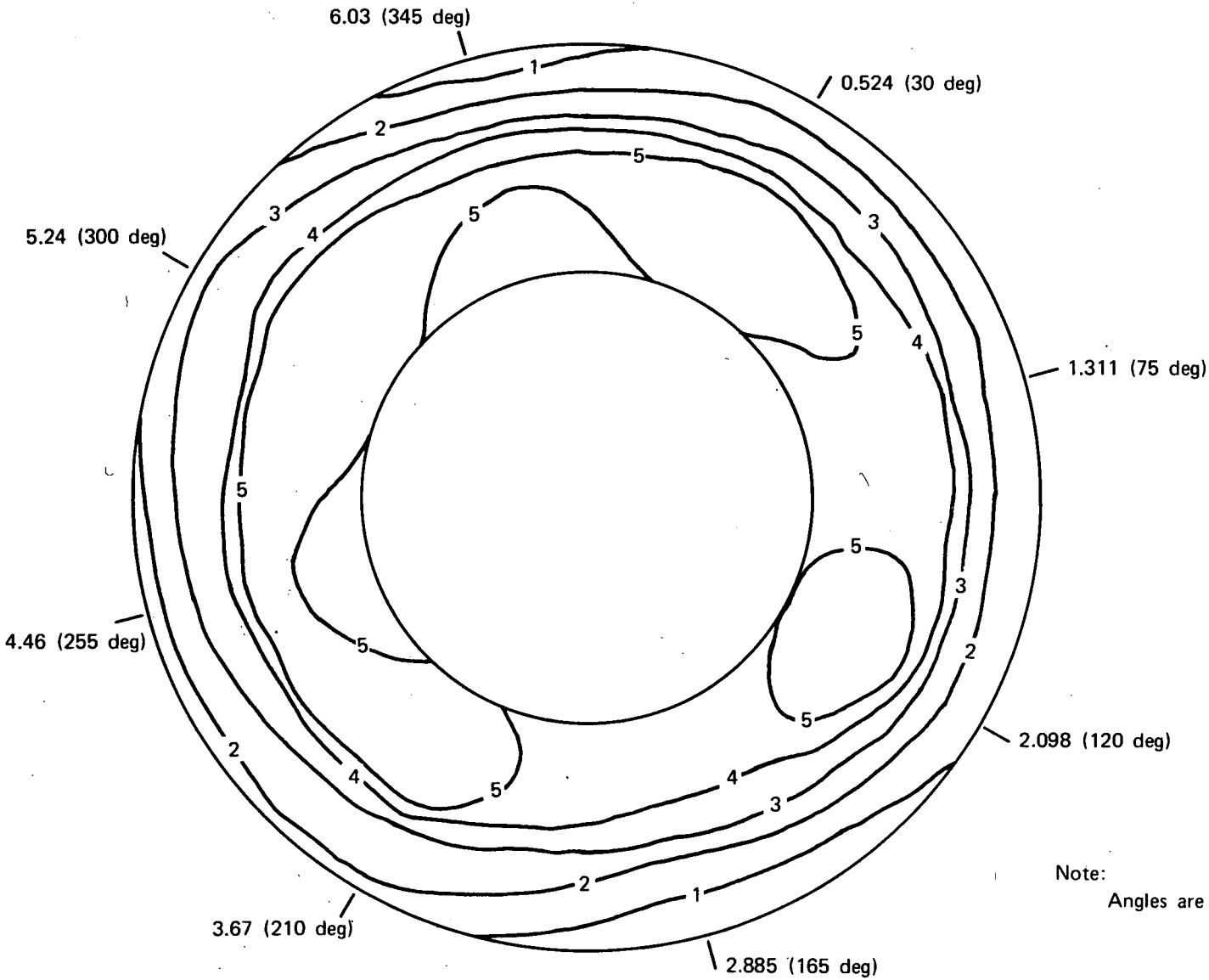

Figure 79. F100/F401 High Compressor Inlet Pressure Map With Thermal Distortion, $\Delta T = 55\,°K$ (100 °F); Build 205, Run 4753

FD-63405

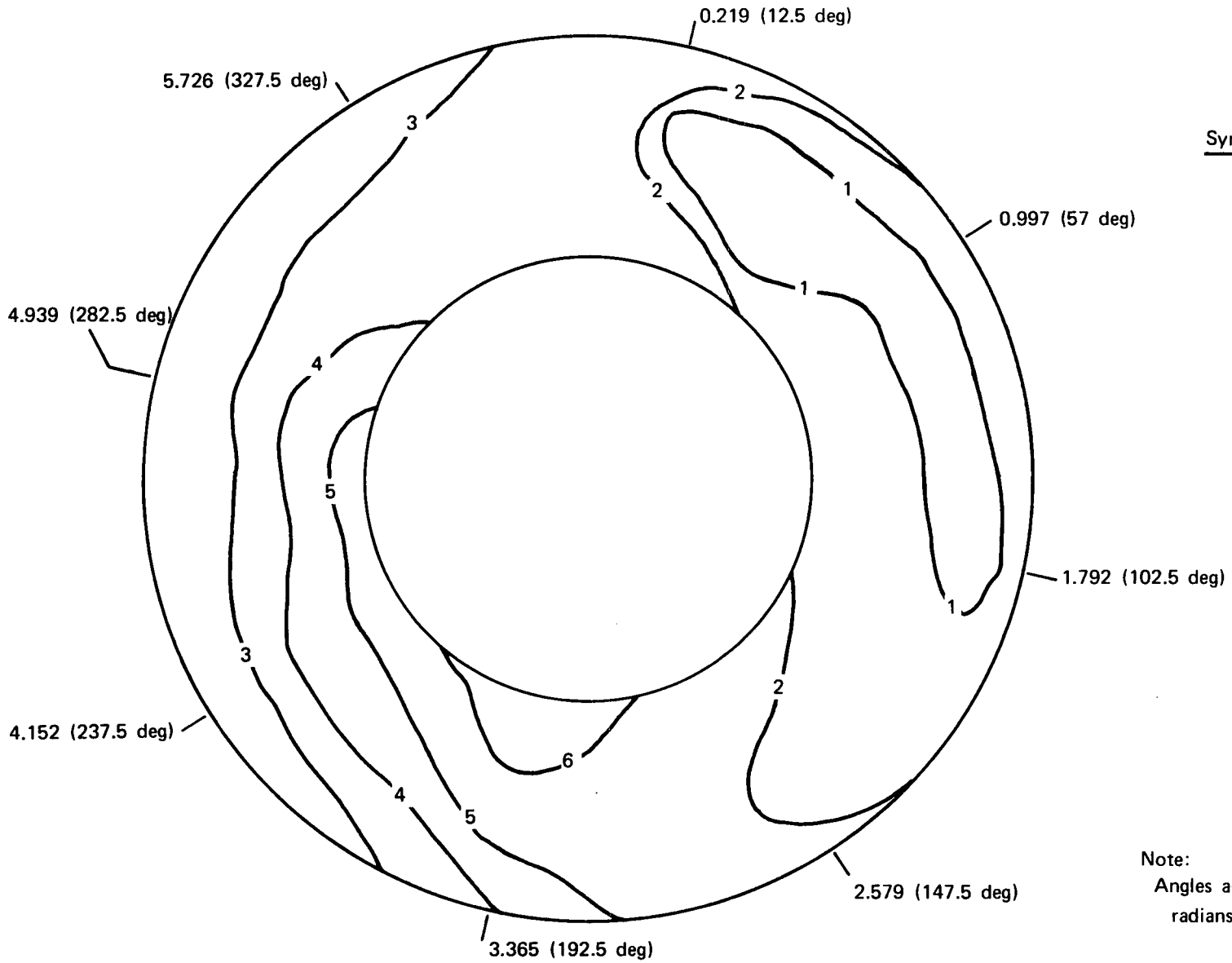

Figure 80. F100/F401 High Compressor Inlet Temperature Map With Thermal Distortion, $\Delta T = 55\,°K$ (100 °F); Build 205, Run 4753

FD 63408

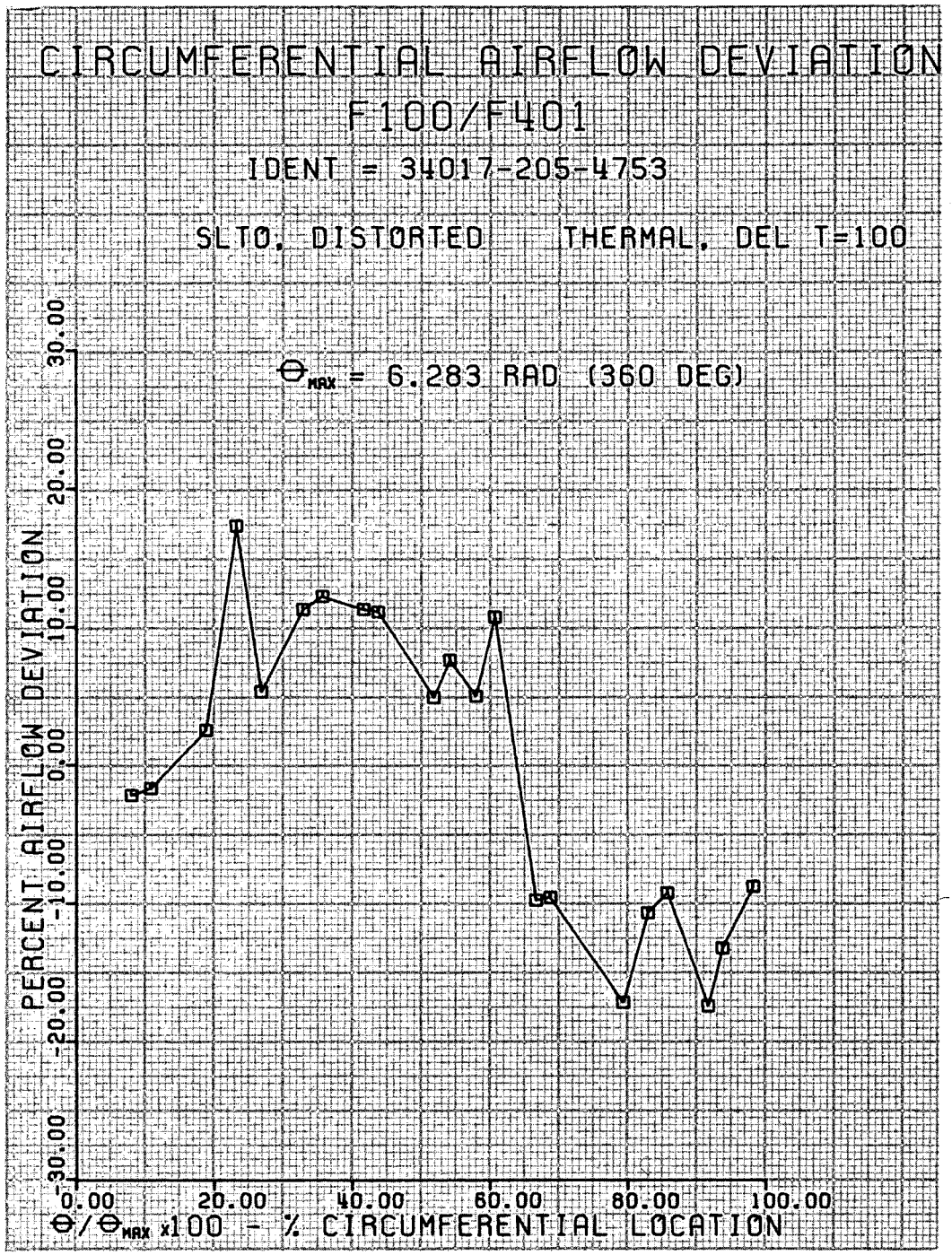

Figure 81.

DF 92109

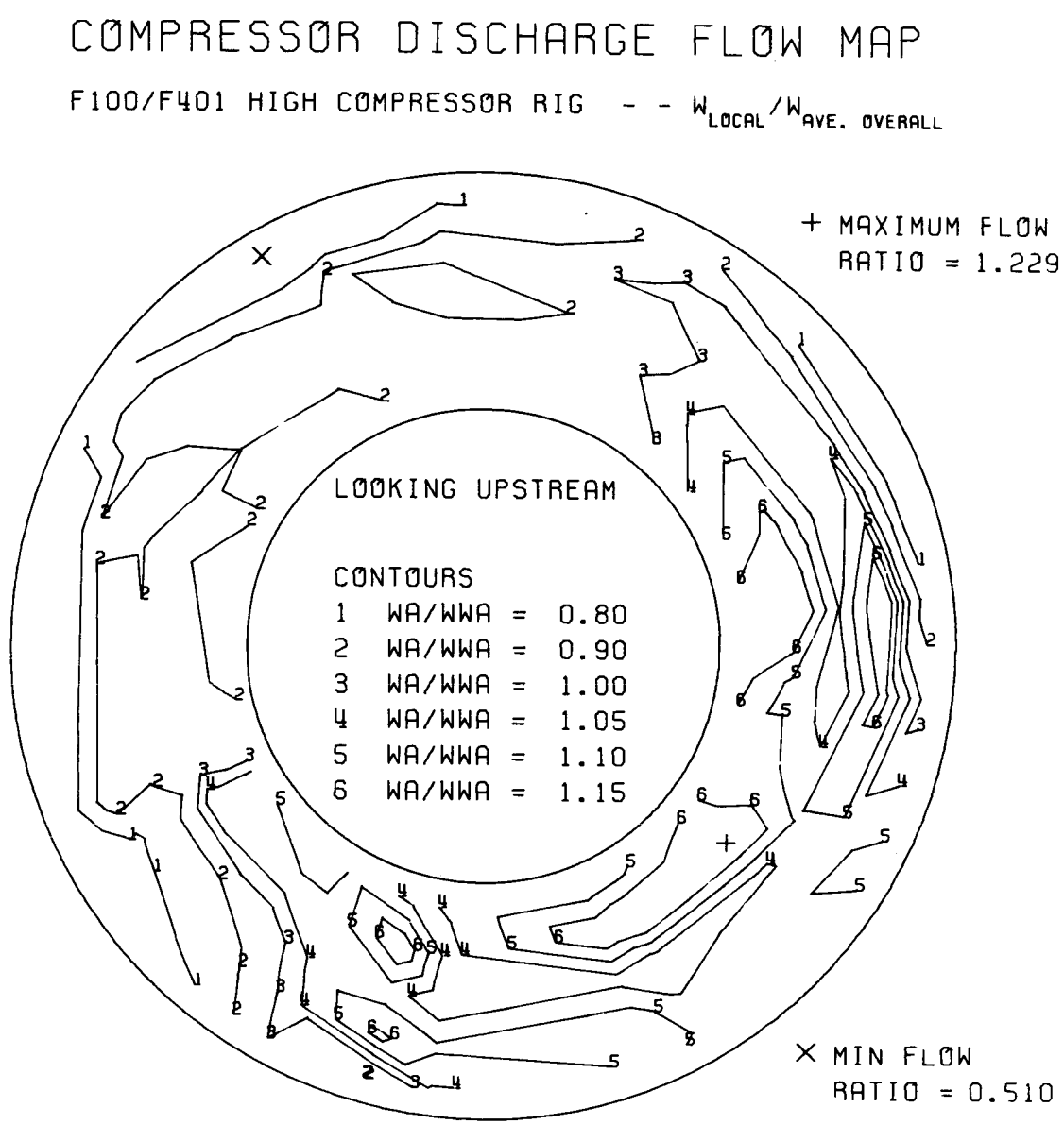

Figure 82.

DF 92090

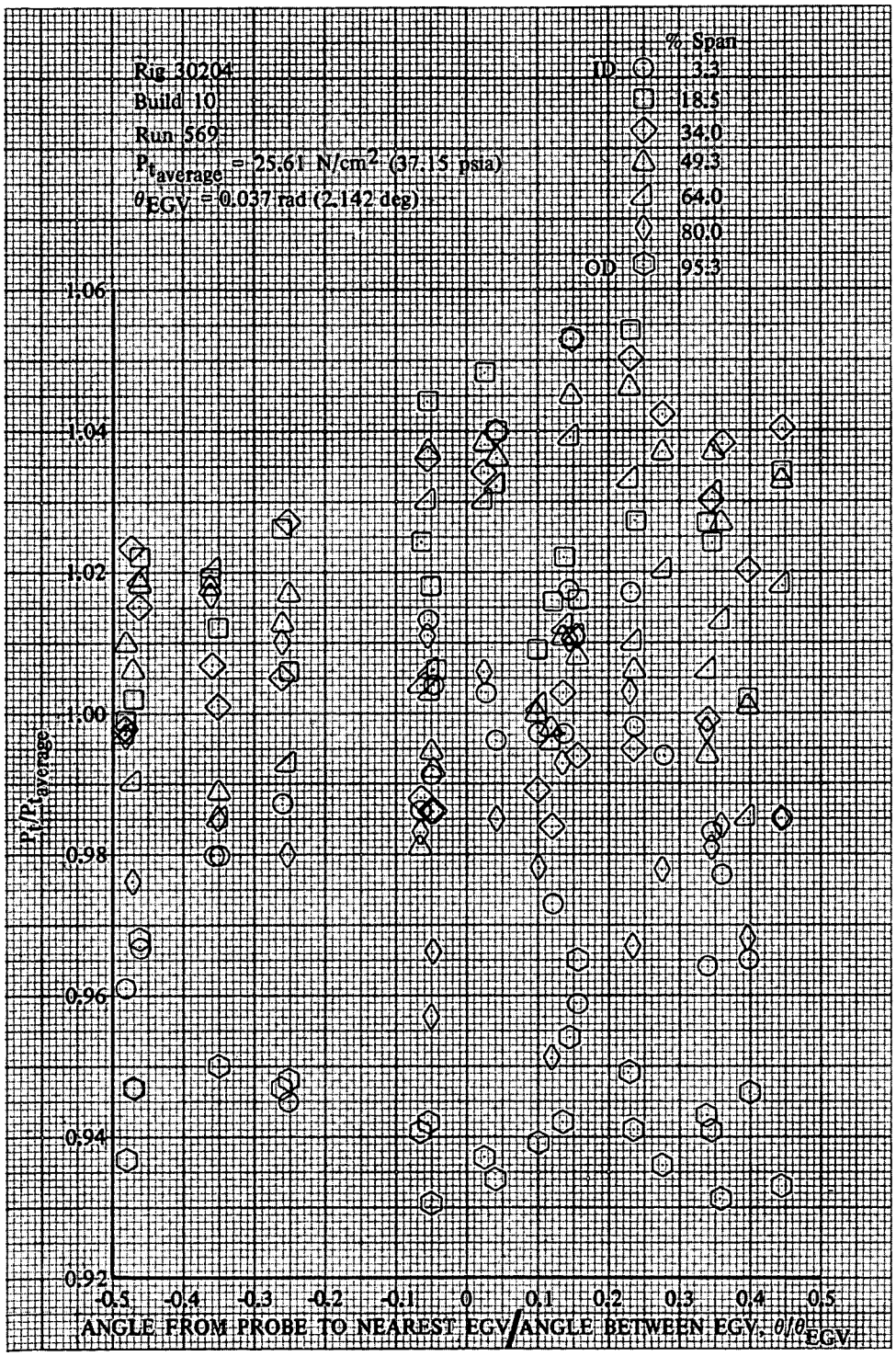

Figure 83. J58 Compressor Discharge Total Pressure Distribution Relative to Exit Guide Vane (EGV) Trailing Edge

DF 92116

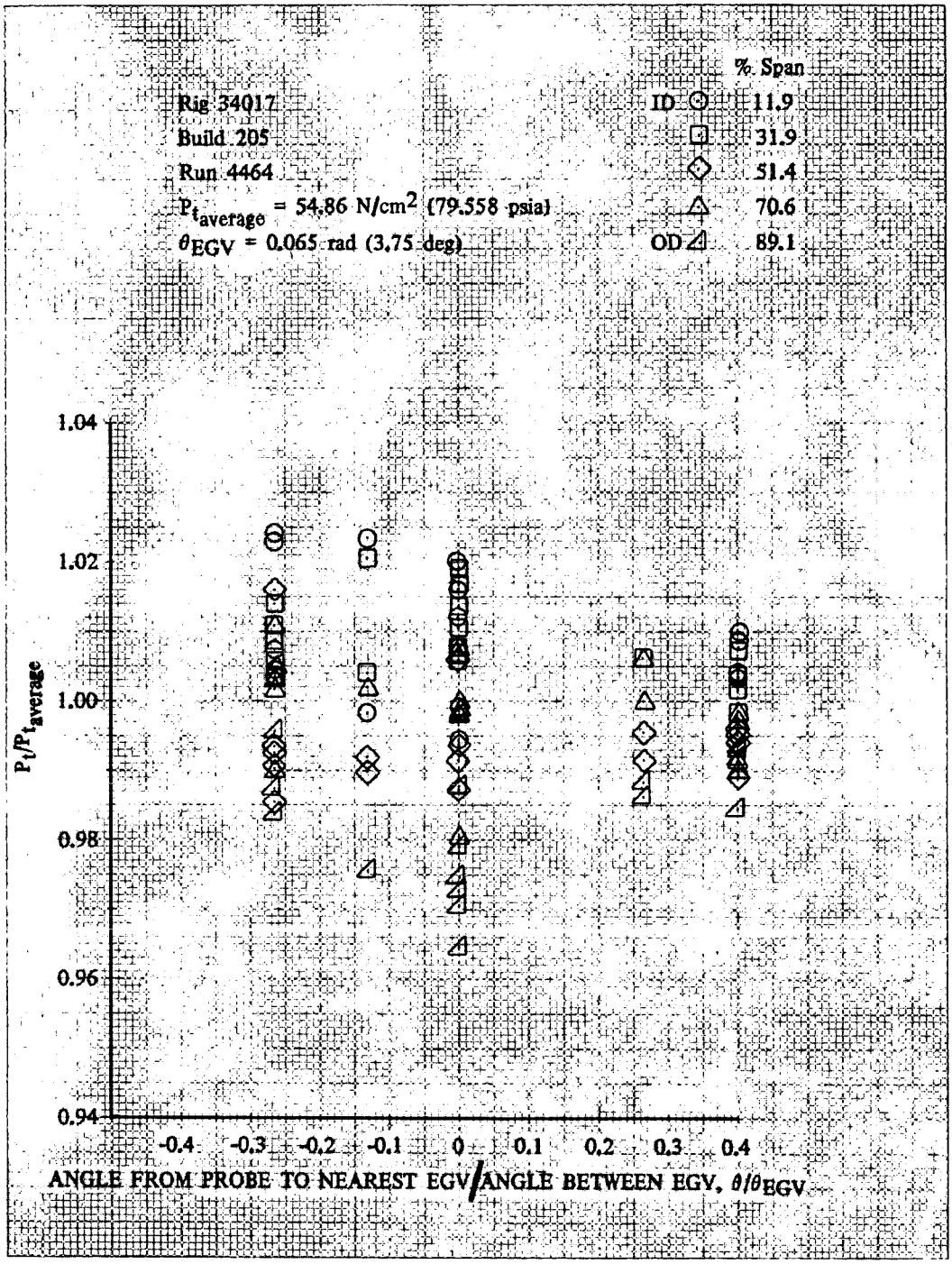

Figure 84. F100/F401 High Compressor Discharge Total Pressure Distribution Relative to Exit Guide Vane (EGV) Trailing Edge DF 92115

REFERENCES

1. Shadowen, J. H., and W. J. Egan, Jr., "Evaluation of Circumferential Airflow Uniformity Entering Combustors from Compressors, Volume II - Data Supplement," NASA CR 121010, 1972.

2. Keenan, J. H., and J. Kaye, Gas Tables, John Wiley & Sons, Inc., New York, 1965.